

The Pennsylvania State University
The Graduate School
College of Earth and Mineral Sciences

**RELATIONSHIPS BETWEEN RAINFALL CHARACTERISTICS
AND ENVIRONMENTAL PREDICTORS IN THE WEST AFRICAN
REGION**

A Dissertation in
Meteorology
by
Holly L. Hamilton

© 2016 Holly L. Hamilton

Submitted in Partial Fulfillment
of the Requirements
for the Degree of

Doctor of Philosophy

August 2016

The dissertation of Holly L. Hamilton was reviewed and approved* by the following:

Jenni L. Evans
Professor of Meteorology
Dissertation Co-Advisor, Co-Chair of Committee

José D. Fuentes
Professor of Meteorology
Dissertation Co-Advisor, Co-Chair of Committee

Michael E. Mann
Professor of Meteorology

George S. Young
Professor of Meteorology
Joint appointment with the GeoEnvironmental Engineering Program

Robert Crane
Professor of Geography
Director of the Alliance for Education, Science, Engineering and Development
in Africa

David Stensrud
Professor of Meteorology
Head of the Department of Meteorology

*Signatures are on file in the Graduate School.

Abstract

Mesoscale Convective Systems (MCS) are a substantial source of the water required for agriculture and human consumption in West Africa. Understanding the lifecycle behaviour of West African mesoscale storms poses unique challenges as these systems traverse strong thermodynamic gradients in their westward propagation from land to ocean. MCS in this region are known to be associated with African Easterly Waves (AEWs). The topography of eastern Africa, namely the Ethiopian Highlands and Darfur Mountains have been shown to play an intricate role in the genesis of these waves through MCS initiation in that region. We investigate the topographic influence on the formation of these systems using the Weather Research and Forecasting model by recreating the atmospheric state over an eight day period for three cases with varying topography: realistic, half-height, and no topography. As a case study, we use a MCS observed on August 30-31 during the NASA African Monsoon Multidisciplinary Analysis field experiment of 2006. This sensitivity study reveals that the topography influences the development and structure of the reference MCS event. The model persisted in simulating the MCS in conjunction with an AEW in each run, which highlights the robustness of the well-known connection between the two systems in West Africa. The development of the simulated MCSs differ in each run due to their interaction with the AEW and the onshore flow that are in turn impacted by the topography.

We examine further the topographic influences on the evolution and energetics of AEW and the formation of convective systems within these AEW. The Weather Research and Forecasting (WRF) model is employed to simulate the evolution over a 36-day period for three cases with varying topography: realistic, half-height, and no topography. An energetics analysis for AEW reveals that baroclinic processes that develop low-level waves north of the jet strengthens due to a stronger monsoonal flow in the flattened topography environment. A noticeably weaker contribution from barotropic and baroclinic instabilities at the jet level in West Africa in the flattened topography simulation explains the weakening of those waves at that level. The results show that topography in Africa plays more of a role in the wave development as they propagate westward rather than in their initiation over East

Africa.

Satellite rainfall estimates reveal a consistent rainfall maximum offshore West Africa during the monsoon rainy season. A 16-year rainfall climatology is conducted to examine the cause of such copious amounts of rainfall. Composites of daily rainfall and mid-level meridional winds centered on the days with maximum rainfall in August show that the day with heaviest rainfall follows the strongest mid-level northerlies. Reflectivity and rain type composites show that stratiform rain dominates the region. The composites suggest that the dominant contribution to the offshore rainfall maximum derives from the trailing stratiform portion of mesoscale convective systems in the northerly phase of African Easterly Waves propagating off the continent. Sensitivity simulations done with the WRF model recreates the rainfall maximum and indicates the weakening of the maximum as topography on the African continent is flattened.

Table of Contents

List of Figures	vii
List of Tables	xii
List of Symbols	xiii
Acknowledgments	xv
Chapter 1	
Introduction	1
1.1 The West African Monsoon	2
1.1.1 African Easterly Waves and their convective interactions . . .	3
1.2 Coastal Influences on African Easterly Waves and Mesoscale Con- vective System Development	5
1.2.1 Frictional convergence	6
1.2.2 Interaction with coastal topography	7
1.3 Topographic Influence on African Easterly Waves and their Convec- tive Interactions	9
1.4 African Easterly Wave Energetics	10
1.5 Objectives and outline	11
Chapter 2	
A Case Study of Topographic Influence on the Development of West African Mesoscale Convective Systems	13
2.1 Introduction	13
2.2 Numerical Model Configuration and Design of Sensitivity Runs . . .	14
2.3 Observed Case Description (OBS)	17
2.3.1 Satellite Data	17
2.3.2 Field Experiment Site Description and Data Collected . . .	17
2.3.3 AEW and MCS Event of 30-31 August 2006	18
2.4 Simulations of MCS	20

2.4.1	Control simulation (TOPO)	22
2.4.2	HALF simulation	27
2.4.3	FLAT simulation	28
2.5	Conclusion	28
Chapter 3		
Topographic Influence on AEW Energetics and Convective Interactions		36
3.1	Introduction	36
3.2	Numerical Model Configuration and Design of Sensitivity Runs . . .	39
3.3	African Easterly Wave Sensitivity to Large-Scale Topography	40
3.3.1	Computation of African Easterly Wave Energetics	43
3.4	African Easterly Wave and Convective Interactions	44
3.4.1	Energy conversions in West Africa	47
3.4.2	Energy conversions in East Africa	54
3.5	Conclusions	57
Chapter 4		
Climatology of the West African Offshore Rainfall Maximum and its relationship with topography		60
4.1	Introduction	60
4.2	Data	62
4.2.1	TRMM Products	62
4.2.2	Reanalysis data	62
4.3	Model Sensitivity Runs	63
4.4	Rainfall Climatology	63
4.4.1	Moisture Flux Convergence	65
4.5	Rainfall Composites	65
4.5.1	Composites of area-averaged terms	66
4.5.2	Composites of deviations from the zonal mean	67
4.6	Conclusion	70
Chapter 5		
Summary and Conclusions		74
Bibliography		77

List of Figures

1.1	Annually-averaged seasonal (May to October 1998-2013) rainfall (in mm) from TRMM rainfall estimates. The bold lined box represents the study region (20° – 10° W and 5° – 12° N) designated to explore the offshore rainfall maximum in chapter 4.	6
2.1	Model terrain height in meters from WRF model. The outer domain has a grid spacing of 36 km. The second domain has a grid spacing of 12 km and the inner domain has a grid spacing of 4 km. The dashed and solid white boxes highlight the domains marked as West Africa (WA; 5 - 25° N, 10° W- 20° E) and East Africa (EA; 5 - 20° N, 15 - 30° E) respectively, used in the energetics analysis. The letter D marks the location of the Darfur Mountains and E marks the location of the Ethiopian Highlands. The location of the research site during the NASA African Monsoon Multidisciplinary Analysis (NAMMA) field campaign is marked by the red star.	16
2.2	Three-hourly precipitation rates (mm hr^{-1}) from TRMM showing the lifecycle of the observed MCS case study on 31 August 2006 at (a) 0000 UTC, (b) 0300 UTC, (c) 0600 UTC, (d) 0900 UTC, (e) 1200 UTC, and (f) 1500 UTC. Note the MCS is located in the top right corner of panel (a) and travels southwesterly towards the Senegalese coast. Arrows indicate 700 hPa wind vectors and the red dashed contour indicates where the 700 hPa meridional wind is zero from six-hourly ERA-Interim data.	19

2.3	Time series of the (a) virtual potential temperature, (b) equivalent potential temperature, and (c) specific humidity measured by the rawinsondes at the research site on 30 August at 1758 UTC, 31 August at 0000, 0501, 0907, 1152, 1806 UTC, and 1 September at 0148, 0624, and 1702 UTC. The 0907 rawinsonde failed shortly after launch. Time series of the (d) virtual potential temperature, (e) equivalent potential temperature, and (f) specific humidity from the TOPO run from 1900 UTC 30 August to 1800 UTC 01 September at 1 hour intervals.	21
2.4	Time series of the (a) total wind speed and (b) zonal wind speed measured by the rawinsondes at the research site on 30 August at 1758 UTC, 31 August at 0000, 0501, 0907, 1152, 1806 UTC, and 1 September at 0148, 0624, and 1702 UTC. The 0907 failed shortly after launch. Time series of the (c) total wind speed and (d) zonal wind speed from the TOPO run from 1900 UTC 30 August to 1800 UTC 01 September at 1 hour intervals.	22
2.5	Maximum reflectivity in dBZ (shaded) and winds at 850 hPa (vectors) in domain 3 from the TOPO simulations for (a) 0000 UTC, (b) 0200 UTC, (c) 0400 UTC, and (d) 0600 UTC on 31 August 2006. The location of the research site is marked by the red star at 14.66°N, 17.10°W.	23
2.6	Vertical cross section of reflectivity in dBZ (shaded) and total wind vectors in domain 3 from the TOPO simulations for (a) 0000 UTC, (b) 0200 UTC, (c) 0400 UTC, and (d) 0600 UTC on 31 August 2006 along 14.66°N.	24
2.7	Meridional winds (shaded) and total wind (vectors) at 650 hPa in domain 2 from TOPO simulation for (a) 0000 UTC, (b) 0200 UTC, (c) 0400 UTC, and (d) 0600 UTC on 31 August 2006. The location of the research site is marked by the red star at 14.66°N, 17.10°W.	26
2.8	Maximum reflectivity in dBZ (shaded) and winds at 850 hPa (vectors) in domain 3 from the HALF simulation for (a) 2000 UTC, (b) 2200 UTC on 30 August, and (c) 0000 UTC and (d) 0200 UTC on 31 August 2006. The location of the research site is marked by the red star at 14.66°N, 17.10°W.	30
2.9	Vertical cross section of reflectivity in dBZ (shaded) and total wind vectors in domain 3 from the HALF simulations for (a) 2000 UTC, (b) 2200 UTC on 30 August, and (c) 0000 UTC and (d) 0200 UTC on 31 August 2006 along 14.66°N.	31

2.10	Meridional winds (shaded) and total wind (vectors) at 650 hPa in domain 2 from HALF simulation for (a) 2000 UTC and (b) 2200 UTC on 30 August, and (c) 0000 UTC and (d) 0200 UTC on 31 August 2006. The location of the research site is marked by the red star at 14.66°N, 17.10°W.	32
2.11	Maximum reflectivity in dBZ (shaded) and winds at 850 hPa (vectors) in domain 3 from the FLAT simulation for (a) 0000 UTC, (b) 0200 UTC, (c) 0400 UTC, and (d) 0600 UTC on 31 August 2006. The location of the research site is marked by the red star at 14.66°N, 17.10°W.	33
2.12	Meridional winds (shaded) and total wind (vectors) at 650 hPa in domain 2 from FLAT simulation for (a) 0000 UTC, (b) 0200 UTC, (c) 0400 UTC, and (d) 0600 UTC on 31 August 2006. The location of the research site is marked by the red star at 14.66°N, 17.10°W.	34
2.13	Vertical cross section of reflectivity in dBZ (shaded) and total wind vectors in domain 3 from the FLAT simulations for (a) 0000 UTC, (b) 0200 UTC, (c) 0400 UTC, and (d) 0600 UTC on 31 August 2006 along 14.66°N.	35
3.1	The mean zonal wind speed at 650 hPa (m s^{-1}) from (a) ERA-Interim and (b) domain 1 in TOPO, and vertical cross section of mean zonal wind speed (m s^{-1}) from (c) ERA-Interim and (d) domain 1 in TOPO at 0° longitude averaged over 25 August to 30 September 2006.	41
3.2	(<i>left</i>) Simulated mean total winds (shaded and vector) at 650 hPa in domain 1 in (a) TOPO, (c) HALF and (e) FLAT and (<i>right</i>) the mean potential temperature at 925 hPa in domain 1 in (b) TOPO, (d) HALF and (f) FLAT averaged over the 35.5-day analysis period.	42
3.3	Rainfall accumulation (mm) over the 35.5-day analysis period in Domain 1 in (a) TOPO, (b) HALF and (c) FLAT.	45
3.4	Hovmöller diagrams of 700 hPa meridional winds (m s^{-1}) and precipitation (mm hr^{-1}) averaged between 9° and 15°N for (a and b) TOPO, (c and d) HALF, and (e and f) FLAT. The dashed lines highlight the estimated location of the wave trough.	46
3.5	Time series of zonal mean precipitation (mm hr^{-1}) over East Africa (15° to 30°E averaged between 9° and 15°N) overlain with the time series of (<i>left</i>) zonal mean C_{k1} (blue line), C_{k2} (red line), C_{pk} (green line), and (<i>right</i>) K_E from 15° to 30°E averaged between 5° and 20°N for (a and b) TOPO, (c and d) HALF, and (e and f) FLAT	48

3.6	Time series of zonal mean precipitation (mm hr^{-1}) over West Africa (10°W to 20°E averaged between 9° and 15°N) overlain with the time series of (<i>left</i>) zonal mean C_{k1} (blue line), C_{k2} (red line), C_{pk} (green line), and (<i>right</i>) K_E from 10°W to 20°E averaged between 5° and 25°N for (a and b) TOPO, (c and d) HALF, and (e and f) FLAT	49
3.7	Mean meridional distribution of (<i>top</i>) u and (<i>bottom</i>) $([u'^2 + v'^2]/2g)$ averaged over the West Africa region for (a and d) TOPO, (b and e) HALF, and (c and f) FLAT. Contour intervals are 1 m s^{-1} in (a)-(c) and 0.1 m in (d)-(f). The bold contour marks the zero line.	50
3.8	Mean meridional distribution of (<i>top</i>) $-([u'v']/g)(\partial[u]/\partial y)$ and (<i>bottom</i>) $-([u'\omega']/g)(\partial[u]/\partial p)$ averaged over the West Africa region for (a and d) TOPO, (b and e) HALF, and (c and f) FLAT. Contour intervals are $0.1 \times 10^{-5} \text{ m s}^{-1}$. The bold contour marks the zero line.	51
3.9	Mean meridional distribution of (<i>top</i>) $-([v'T']/\bar{\sigma})(\partial[T]/\partial y)$, (<i>middle</i>) $-([\omega'T']/\bar{\sigma})(\partial[T]^*/\partial p)$, and (<i>bottom</i>) $-(R/pg)[\omega'T']$ averaged over the West Africa region for (a, d and g) TOPO, (b, e and h) HALF, and (c, f, and i) FLAT. Contour intervals are $0.5 \times 10^{-5} \text{ m s}^{-1}$ in (a)-(c) and $0.3 \times 10^{-5} \text{ m s}^{-1}$ in (d)-(i). The bold contour marks the zero line.	53
3.10	Mean meridional distribution of (<i>top</i>) u and (<i>bottom</i>) $([u'^2 + v'^2]/2g)$ averaged over the East Africa region for (a and d) TOPO, (b and e) HALF, and (c and f) FLAT. Contour intervals are 1 m s^{-1} in (a)-(c) and 0.1 m in (d)-(f). The bold contour marks the zero line.	54
3.11	Mean meridional distribution of (<i>top</i>) $-([u'v']/g)(\partial[u]/\partial y)$ and (<i>bottom</i>) $-([u'\omega']/g)(\partial[u]/\partial p)$ averaged over the East Africa region for (a, d, and g) TOPO, (b, e, and h) HALF, and (c, f, and i) FLAT. Contour intervals are $0.1 \times 10^{-5} \text{ m s}^{-1}$. The bold contour marks the zero line.	55
3.12	Mean meridional distribution of (<i>top</i>) $-([v'T']/\bar{\sigma})(\partial[T]/\partial y)$ and (<i>middle</i>) $-([\omega'T']/\bar{\sigma})(\partial[T]^*/\partial p)$, and (<i>bottom</i>) $-(R/pg)[\omega'T']$ averaged over the East Africa region for (a, d and g) TOPO, (b, e and h) HALF, and (c, f and i) FLAT. Contour intervals are $0.5 \times 10^{-5} \text{ m s}^{-1}$ in (a)-(c) and $0.3 \times 10^{-5} \text{ m s}^{-1}$ in (d)-(i). The bold contour marks the zero line.	56

4.1	Annually-averaged (a) seasonal (May to October) TRMM rainfall (mm) and (b) TRMM rainfall accumulated over 1200 UTC 25 August to 0000 UTC 30 September over the period 1998-2013. Rainfall accumulation (mm) over 35.5-day period (1200 UTC 25 August to 0000 UTC 30 September 2006) from (c) TRMM, and domain 2 of (d) TOPO, (e) HALF and (f) FLAT. The bold lined box represents the study region from 20°–10°W and 5°–12°N.	64
4.2	Composites of area-averaged (a) precipitation [mm day ⁻¹], (b) rain type ratio (black = stratiform; red = convective), (c) meridional wind speed [m s ⁻¹], and (d) moisture flux (black = low-level, 1000-850 hPa; red = mid-level, 700-500 hPa) [g kg ⁻¹ m s ⁻¹] centered on the rainiest day in August-September averaged over 1998-2013.	67
4.3	Composites of ERA-Interim 3-5-day filtered deviation from the zonal average in (a) zonal wind [m s ⁻¹], (b) meridional wind [m s ⁻¹], (c) vertical velocity [10 ⁻¹ Pa s ⁻¹], and (d) temperature [K] at 1000-850 hPa (shaded) and 700-500 hPa (contour) on the rainiest day in August-September averaged over 1998-2013.	68
4.4	Daily timeseries of the simulated rainfall in TOPO (blue line), HALF (red line) and FLAT (yellow line).	69
4.5	Composites of 3-5-day filtered deviation from the zonal average in (a) zonal wind [m s ⁻¹], (b) meridional wind [m s ⁻¹], (c) vertical velocity [10 ⁻¹ Pa s ⁻¹], and (d) temperature [K] at 1000-850 hPa (shaded) and 700-500 hPa (contour) on the peak rainfall days during the WRF TOPO simulation.	71
4.6	Composites of 3-5-day filtered deviation from the zonal average in (a) zonal wind [m s ⁻¹], (b) meridional wind [m s ⁻¹], (c) vertical velocity [10 ⁻¹ Pa s ⁻¹], and (d) temperature [K] at 1000-850 hPa (shaded) and 700-500 hPa (contour) on the peak rainfall days during the WRF HALF simulation.	72
4.7	Composites of 3-5-day filtered deviation from the zonal average in (a) zonal wind [m s ⁻¹], (b) meridional wind [m s ⁻¹], (c) vertical velocity [10 ⁻¹ Pa s ⁻¹], and (d) temperature [K] at 1000-850 hPa (shaded) and 700-500 hPa (contour) on the peak rainfall days during the WRF FLAT simulation.	73

List of Tables

3.1 Mathematical expressions for the components in the energy equation. $[\langle \rangle]$ represents a zonal average while $\overline{[\langle \rangle]}$ represents a meridional average of the zonal mean; primes represent deviations from the zonal average, and asterisks represent deviations from the area mean on an isobaric surface. They are related by $\langle \rangle = [\langle \rangle] + \langle \rangle'$ and $\overline{[\langle \rangle]} = \overline{[\langle \rangle]} + \overline{[\langle \rangle]}^*$. Variable names follow the AMS Glossary of Meteorology. 59

List of Symbols

- θ Potential temperature. page 2
- θ_e Equivalent potential temperature. page 5
- q Specific humidity. page 18
- θ_v Virtual potential temperature. page 18
- u Zonal wind speed. page 40
- K_E Eddy kinetic energy. page 43
- A_E Eddy kinetic energy. page 43
- A_z Zonal available potential energy. page 43
- C_k Barotropic energy conversion. page 43
- C_{k1} Barotropic energy conversion through horizontal shear of zonal wind. page 43
- C_{k2} Barotropic energy conversion through vertical shear of zonal wind. page 43
- C_{k3} Barotropic energy conversion through horizontal wind shear of meridional wind. page 43
- C_{k4} Barotropic energy conversion through vertical wind shear of meridional wind. page 43
- C_{pk} Baroclinic energy conversion. page 43
- C_A Conversion of zonal available potential energy to eddy available potential energy due to eddy heat flux along the zonal mean temperature gradient. page 43

G_E	Generation of eddy available potential energy by diabatic heating. page 43
D_E	Frictional dissipation. page 43
Φ_{EB}	Boundary pressure work done by eddies. page 43
K_{EB}	Boundary flux of eddy kinetic energy advecting into and out of the region of interest. page 43
A_{EB}	Boundary fluxes of eddy available potential energy advecting into and out of the region of interest. page 43
u'	Deviation of the zonal wind from its zonal average. page 44
v'	Deviation of the meridional wind from its zonal average. page 44
ω'	Deviation of vertical velocity from its zonal average. page 44
T'	Deviation of temperature from its zonal average. page 44
C_{A1}	Zonal eddy heat flux weighted by the zonal mean temperature gradient. page 52
C_{A2}	Vertical eddy heat flux weighted by the vertical gradient of the zonal mean temperature deviation. page 52
T^*	Temperature deviations from the area mean on an isobaric surface. page 52
v	Meridional wind speed. page 63
ω	Vertical velocity. page 63
T	Temperature. page 63
MF	Moisture Flux. page 65

Acknowledgments

The author wishes to thank Dr. Jenni Evans for her guidance and constant advice throughout the course of her graduate studies. The road was long and bumpy at times but she remained confident in me, even when I failed to believe in myself. I appreciate all her contributions of time, ideas, and funding to make my graduate experience productive and stimulating. I am also thankful for the excellent example she has provided as a successful woman in meteorology and academia.

Thanks to Dr. José Fuentes for his guidance and contribution to this work. Many thanks to Dr. George Young for imparting a great deal of knowledge to me and for being a mentor. I enjoyed having many stimulating conversations with you about meteorology, career and life that has encouraged me to pursue my true passion in life. I am grateful for Dr. Michael Mann and Dr. Robert Crane for being on my doctoral committee and for their valuable contribution to my doctoral work.

Thanks to Marcia DeLonge for providing the rawinsonde observations recorded during the NAMMA/AMMA research campaign. Thanks to Dean Pryles, Glorianne Rivera-Santiago, and Kelly Núñez Ocasio, excellent students of the Research Experience for Undergraduates (REU) program who contributed to the preliminary work on this research. Thanks to Christopher Melhauser and Fuqing Zhang for their help with numerical modeling resources. I am grateful for the assistance of Chuck Pavloski and Chad Bahrmann in database analysis and management.

I am grateful for the love and support from my fiancé, Les, during the last two years of my graduate studies. Every encouraging word you gave motivated me to continue striving towards my goal. Thanks to my family for their undying and unwavering support throughout my entire educational pursuit. This dissertation marks the end of that long journey that began on September 2005. You have been there every step of the way and I am forever grateful.

Dedication

I dedicate this dissertation to my parents, Clifford and Hope Hamilton. I hope that this achievement fulfills the dream that you had for me all those many years ago when you sacrificed to give me the best education you could. Thank you.

Chapter 1 | Introduction

Monsoon rainfall is a critical part of the climate of West Africa and understanding its variability is crucial to the livelihood of the persons inhabiting that region. Mesoscale convective systems (MCSs) are primary contributors of monsoon rainfall required for agriculture and human consumption in West Africa (LeBarbé and Lebel, 1997; D'Amato and Lebel, 1998; Laurent et al., 1998; Laing et al., 1999; Nicholson and Yin, 2001; Mathon et al., 2002; Redelsperger et al., 2002; Fink et al., 2006; Guy et al., 2011). Connections between rainfall deviations from the long-term trend and armed conflicts in Africa reveal the strong dependence of rainfall in this region (Hendrix and Salehyan, 2010; O'Loughlin et al., 2012; Fjelde and von Uexkull, 2012). Greater than average rainfall increases agricultural productivity, which increases both food availability and income for farming households; this economic and food security coincides with decreased conflicts in local areas (O'Loughlin et al., 2012). Also, there are close connections between storm rainfall amounts and onset of malaria and cholera (Robert et al., 2003; Shultz et al., 2005; de Magny et al., 2007) or retreat of meningitis (Kelly-Hope and Thompson, 2008). The impacts of projected future changes in meteorological conditions on vector-borne infectious disease in the region rely on changes in rainfall. Thus, health workers and decision makers as well as community members can utilize rainfall information to prepare for likely disease outbreaks in the short-term, and plan for wide-reaching and timely abatement strategies in the seasonal to longer term.

Variability in seasonal MCS frequency accounts for the difference between dry and wet years in the region (Lebel et al., 1997). The monsoon flow is the main source of moisture for convective activity over West Africa during the rainy season and so plays a major role in determining where MCSs are initiated, and motion of these MCSs in turn influences the geographic distribution of rainfall. Rainfall

gradients are observed as storms traverse strong thermodynamic gradients in their westward propagation from land to ocean. Fast-moving MCSs produce about 50% of the rain in the Soudanian zone (9-12°N) and most of the rain over the Sahel (12-18°N) (Lafore et al., 2011). MCS propagation can be influenced by many different factors, including the distribution of convective available potential energy (CAPE), convective inhibition (CIN), gravity waves, easterly waves, outflow boundaries, and orographic effects (Carlson, 1969a; Zehnder et al., 1999; Thorncroft and Hodges, 2001; Redelsperger et al., 2002; Fink and Reiner, 2003; Baum, 2006; Fink et al., 2006; Nicholson, 2008, 2009; DeLonge et al., 2010).

Despite the extensive knowledge of the formation, propagation, and demise of MCSs in West Africa, little is known about how MCS rainfall yields are varying due to changes in regional (e.g., increased dustiness, deforestation, etc.) and global (e.g., global warming) environmental patterns. Analyses of rainfall distribution and temporal trends are needed to develop adaptation strategies in region impacted by rainfall deficits. Such assessments are required in West Africa where communities are directly susceptible to droughts or floods due to the interplay of weather with human health and agriculture. Timely rainfall information is important in aiding communities to identify variability and limits of adaptive capacity in rain-fed agriculture and in planning for potential future shifts in agricultural practices.

1.1 The West African Monsoon

The rainy season in West Africa generally spans the months of May to October. The intensification of the cross-equatorial southerlies associated with the onset of the West African Monsoon (WAM) triggers the oceanic cooling in the Gulf of Guinea, which sets up the temperature gradient between the cool Gulf waters and the hot Saharan desert. The strong low-level potential temperature (θ) gradients between the Sahara and the Gulf of Guinea sets up the African Easterly Jet (AEJ) at 700-500 hPa and roughly centered at 15°N (Lebel and Ali, 2009). The AEJ transports moisture from eastern and central Africa to the west, and controls rainfall in the Sahel area (Grist and Nicholson, 2001; Nicholson and Yin, 2001; Nicholson, 2008, 2009; Lebel and Ali, 2009).

Large-scale convergence associated with the Inter-Tropical Convergence Zone (ITCZ) is a strong control on rainfall over West Africa. The seasonal migration of

the ITCZ follows that of the maximum incoming solar radiation, so is relatively stable from year to year (Lebel and Ali, 2009). During the boreal summer, the ITCZ migrates northward from around 5°S to its most northern position between 10°N to 12°N in August (Lebel and Ali, 2009). Over the water, the convergence between the Trade winds and the WAM winds mark the ITCZ. The convergence of the warm and moist southwesterly monsoon flow off the tropical Atlantic and the hot and dry northeasterly flow from the Sahara forms a west-east oriented, quasi-stationary moisture-temperature discontinuity known as the Inter-Tropical Front (ITF), which is associated with the regional ITCZ over West Africa (Lélé and Lamb, 2010). Convergence and uplift occur all along this zone, but convective systems do not develop along the ITF due to weak thickness of the monsoon layer along the front and subsidence in the mid-troposphere. The moist layer deepens rapidly equatorward of the ITF at a rate of about 1 km/1°latitude (Lélé and Lamb, 2010). The initiation of deep convection requires the depth of the monsoon flow to be 1 to 2 km. This puts the cloudiness and rainfall maxima about 300-500 km south of the ITF where the moist layer is deeper (Nicholson, 2009; Lélé and Lamb, 2010).

African Easterly Waves (AEWs) are the dominant type of synoptic disturbance over tropical North Africa and the tropical north Atlantic during the summer (Reed et al., 1977; Thompson et al., 1979; Thorncroft and Hodges, 2001; Kiladis et al., 2006; Lafore et al., 2011). Understanding AEWs is important because they are linked to rainfall and the variability of which can have devastating societal impacts on West Africa. Furthermore, AEWs are known to be precursors of tropical cyclones in the tropical Atlantic and east Pacific Ocean basins, extending their effects beyond the West African region.

1.1.1 African Easterly Waves and their convective interactions

AEWs are generally cold core up to 600 hPa with a weak warm core above extending up to about 200 hPa (Kiladis et al., 2006). AEWs that are coupled to convection tend to have a deep vertical structure with significant perturbations (temperature, moisture, and meridional wind) extending up to the tropopause (Kiladis et al., 2006). These waves typically have periods of 3-5 days, wavelengths of 2000-4000 km, and propagate westward at phase speeds of 6-8 m s⁻¹ (Carlson, 1969a; Burpee, 1972;

Reed et al., 1977). AEWs vortices have two tracks—one to the north and south of the African Easterly Jet (AEJ)—that later merge over the Atlantic Ocean (Carlson, 1969a; Reed et al., 1977; Diedhiou et al., 1998; Thorncroft and Hodges, 2001; Pytharoulis and Thorncroft, 1999; Redelsperger et al., 2002; Nicholson, 2009). The southern-AEWs have maximum amplitude close to the African Easterly Jet (AEJ) level and a low-level vorticity maximum near 850 hPa, and are often associated with moist convection (Carlson, 1969a; Burpee, 1972; Reed et al., 1977; Pytharoulis and Thorncroft, 1999; Thorncroft and Hodges, 2001; Redelsperger et al., 2002; Baum, 2006; Nicholson, 2008, 2009). Northern-AEWs are shallow low-level waves that are primarily characterized by dry convective processes, however, they too are capable of influencing precipitation variability in the Sahel through moisture advection within the southerly flow of their low-level vortex (Gu et al., 2004).

Consistent with the Charney and Stern (1962) instability criterion, the southern-AEWs develop along the reversed meridional potential vorticity (PV) gradient near the AEJ core (Burpee, 1972; Pytharoulis and Thorncroft, 1999). These southern-AEWs are driven by barotropic and baroclinic energy conversions, and reach maximum amplitude in West Africa near 700 hPa at about 11°N (Skinner and Dittenbach, 2014). The northern-AEWs grow primarily through baroclinic interactions between the negative meridional PV gradient in the AEJ core and the positive low-level potential temperature (θ) gradient to the north of the AEJ (Thorncroft and Hoskins, 1994a; Pytharoulis and Thorncroft, 1999), and reach their maximum amplitude near 850 hPa at $\sim 20^\circ\text{N}$ (Thorncroft, 1995).

The association of AEWs with convective triggering (i.e., MCSs) in East Africa and both systems increasing in intensity to the west, is consistent with case-studies of Berry and Thorncroft (2005); Lin et al. (2005) and idealized modelling work by Hall et al. (2006). MCSs move with and through the synoptic-scale AEWs and may act as PV sources for the large-scale circulation and contribute to tropical cyclogenesis (Laing et al., 2008). Some tropical cyclones, such as Tropical Storm Alberto (2000), begin as AEW-MCS systems that initiate near the Ethiopian Highlands and undergo cycles of decay and regeneration while propagating westward (Lin et al., 2005; Laing et al., 2008). Deep convective clouds in MCSs commonly occur at or ahead of the AEW trough, but a secondary maxima in MCS occurs in the southerly flow east of the trough over the northern Sahel (Fink and Reiner, 2003; Fink et al., 2006). MCSs can also develop behind the AEW trough and propagate

into the region ahead of the trough (Fink and Reiner, 2003; Fink et al., 2006; Laing et al., 2008). Mekonnen et al. (2006) found strong correlations between the 2-6-day-filtered convection and dynamical measures of AEW activity over West Africa. Laing et al. (2008), however, suggest that MCSs are more influenced by the local diurnal heating over the high terrain and vertical shear than by AEWs, since in most cases the MCSs move faster than the waves (Redelsperger et al., 2002; Fink and Reiner, 2003; Laing et al., 2008).

1.2 Coastal Influences on African Easterly Waves and Mesoscale Convective System Development

A distinct maximum in accumulated rainfall occurs near the southwest coast of West Africa, where the strong large-scale convergence associated with the ITCZ interacts with the WAM and topographic features (Fig. 4.1). AEW-MCS systems attain maximum intensity near the West African coast, however, only 10% of the AEW-MCSs that move from continental to oceanic conditions develop into tropical systems (Jenkins et al., 2010). Understanding the coastal influences in this region can help to reveal why certain convective systems continue to develop as they cross the coastline while other systems disintegrate.

Recent studies have revealed that there are distinct differences in the dynamic and thermodynamic characteristics of the MCS that propagate through West Africa and, in some cases, over the Atlantic Ocean (DeLonge et al., 2010; Jenkins et al., 2010; Guy et al., 2011). Continental systems are more symmetric and develop more rapidly than their marine counterparts. These precipitating storms also tend to be deep and intense convective systems over the continental regions of West Africa and as they travel towards the Atlantic Ocean they develop stratiform features (DeLonge et al., 2010; Xu and Zipser, 2012). Land and ocean regimes differ based on thermodynamics (i.e., CAPE and CIN), aerosol effects (CCN) or morphology of convective core (Xu and Zipser, 2012). Low-level convergence is usually required to initiate convective overturning over the oceans because only air near the surface has sufficiently high equivalent potential temperature (θ_e) to become buoyant when it is forcibly raised. Convection over continental regions can be initiated without significant boundary layer convergence. Strong surface heating can produce positive

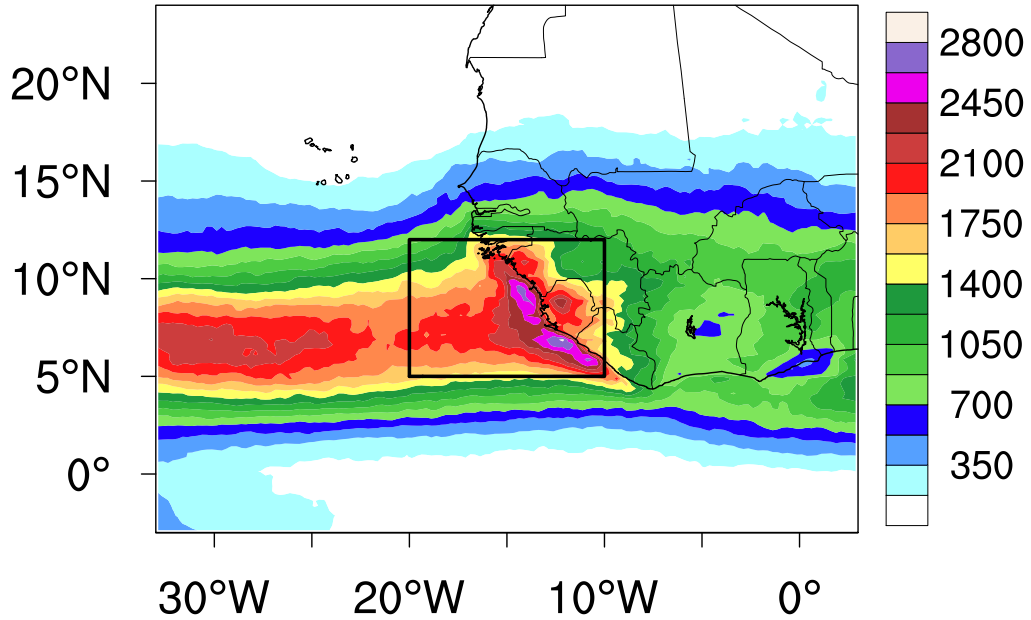


Figure 1.1. Annually-averaged seasonal (May to October 1998-2013) rainfall (in mm) from TRMM rainfall estimates. The bold lined box represents the study region (20° – 10° W and 5° – 12° N) designated to explore the offshore rainfall maximum in chapter 4.

parcel buoyancy all the way to the surface. Sustained deep convection, however, requires mean low-level moisture convergence.

Xu and Zipser (2012) observe that during the monsoon, individual MCS cases can either be convective or oceanic-like. MCSs that occur during active periods of the monsoon are more oceanic-like, while during the break periods of the monsoon they are more continental. Xu and Zipser (2012) observe that the northern portion of West Africa is dominated by squall lines with very intense convection and easterly waves, and the southern portion exhibit more embedded convective MCS during the peak of the monsoon.

1.2.1 Frictional convergence

Mechanical forcing due to changes in surface roughness at a coastline can induce secondary circulations in the boundary layer on the meso-beta scale (10s to 100s km). Roeloffzen et al. (1986) found that upward motion is most pronounced when the geostrophic flow is onshore and makes a small angle ($\sim 20^{\circ}$) with the coastline. The monsoon southwesterlies are potentially creating a favorable environment for

maximum surface convergence and strong ascent along the southwest coastline of West Africa. Strong temperature gradients, increased moisture from the tropical maritime air and strong upward motion force deep convection and heavy rainfall. However, satellite imagery and rainfall estimates show enhanced cloud cover and the rainfall maximum to be just offshore, rather than directly along the coastline. The hypothesis is that the combine effects of orographic forcing and frictional convergence of the wind are potentially leading to strong ascent and hence, strong convection in the Guinea Highland region. Along with the larger-scale convergence associated with the ITCZ and the systems embedded in the upper-level easterly flow develop and propagate away from the coast. This hypothesis is explored in chapter 4.

1.2.2 Interaction with coastal topography

Interactions with the prevailing monsoon flow or large-scale atmospheric flow with complex terrain and topography-generated local circulations can produce enhanced convection and heavy rainfall (Xu et al., 2012; Zehnder, 1991; Zehnder and Gall, 1991; Zehnder et al., 1999). During the Terrain-influenced Monsoon Rainfall Experiment (TiMREX), Xu et al. (2012) find that the topography of Taiwan plays an indirect effect on the persistence of mesoscale systems over the upstream ocean. They observe squall lines passing over south Taiwan, and the following day convection over southwest Taiwan ceases and stratiform precipitation and heavy clouds dominate. Xu et al. (2012) suggest that the persistent rainfall forms a cold pool and the high terrain in Taiwan traps the cold pool from spreading or moving and new convection keeps triggering upstream of the boundary between the precipitation-formed cold pool and the moist monsoon flow. The prevailing southwesterly monsoon flow and the topography in the southwest coast of West Africa – although lower in peak height – is a similar set up to Taiwan, therefore it is possible that the cold pool extending orographic effect can explain the offshore maximum in precipitation over the Atlantic Ocean.

Tracking statistics of AEWs in Thorncroft and Hodges (2001) highlight where the highlands in the coastal region may be a region where the AEWs experience extra development, in association with latent heat release in deep moist convection and orographic processes. Thorncroft and Hodges (2001) show another notable

peak in growth of AEWs just downstream of Mexico. The interaction of easterly flow and easterly waves with the Sierra Madre Mountains in central Mexico have been shown to be responsible for the favored location of AEW development and tropical cyclone initiation in the subtropical Eastern Pacific ocean (Mozer and Zehnder, 1996a,b; Zehnder, 1991; Zehnder and Gall, 1991; Zehnder et al., 1999). The initial cyclonic disturbances are orographically-generated and the warm sea surface temperatures off the coast are favorable for further development.

The largest increase in cyclonic vorticity in the lee of topography occurs during the combined interaction of the easterly wave, the topography and the ITCZ (Zehnder et al., 1999). The easterly waves referred to in (Zehnder et al., 1999) are AEWs. As the easterly wave propagates over the mountain, the anticyclonic vorticity acquired above the mountain causes a northward displacement of the ITCZ. The combined interaction with the wave, topography and ITCZ increases the maximum vorticity of the wave by 100% compared to just a 50% increase when there is only an interaction with the easterly wave and the topography (Zehnder et al., 1999). The enhanced circulation in the lee (i.e., to the west) of the topography is due to the net deflection of parcels ahead of the easterly wave trough plus the advection of the vorticity associated with the ITCZ (Zehnder et al., 1999).

The growth region of AEWs at the West African coast in Thorncroft and Hodges (2001) is collocated with the climatological rainfall maximum in West Africa. The combined interaction of the ITCZ, AEWs, and the topography may explain the climatological rainfall maximum. The Guinea Highlands are similar in height to the Sierra Madre Mountains, but its horizontal extent is much less than the Sierra Madre (150 km compared to 600 km). Zehnder (1991) suggests that there need only be a deviation from a nonzonal flow at sufficiently high latitude (away from the equator) so that it interacts with the topography and persists for about 2-5 days in order to generate cyclonic vorticity maxima. The parcel transit time across the topography also needs to be less than the period of the wave (Zehnder, 1991). A parcel traveling at 10 m s^{-1} will cross the Guinea Highlands in about 4 hours, hence the condition is satisfied. Results of previous studies have indicated that the processes over the Guinea highlands are important in downstream development of MCSs and/or AEWs (Erickson, 1963; Thorncroft and Hodges, 2001; Berry and Thorncroft, 2005; Mohr and Thorncroft, 2006). Erickson (1963) attribute the Guinea highlands as the source of a subsynoptic-scale surface vortex that was

the precursor of Hurricane Debbie (1961). While examining the lifecycle of an intense African easterly wave, Berry and Thorncroft (2005) observed the generation of stationary PV maxima over the Guinea Highlands that later interacted with the westward propagating PV maxima (associated with the AEW trough) and strengthened into Hurricane Alberto (2000).

1.3 Topographic Influence on African Easterly Waves and their Convective Interactions

AEWs are convectively triggered in East and Central Africa (between 15°E and 30°E) downstream of the high terrain of the Ethiopian Highlands and the Darfur Mountains, and grow through mixed barotropic-baroclinic instability of the AEJ (Burpee, 1972; Hodges and Thorncroft, 1997; Pytharoulis and Thorncroft, 1999; Berry and Thorncroft, 2005; Hall et al., 2006; Skinner and Diffenbaugh, 2013). Thorncroft et al. (2008) showed that AEWs are initiated by local convective forcing near the entrance region of the AEJ and the resultant latent heating creates the initial downstream trough that takes 5-7 days to reach the West African coast. Simulations by Leroux and Hall (2009) showed that the strength of the AEJ and meridional PV reversal were weak indicators of the strength of an AEW; rather, the surface area covered by the jet and by the region of PV gradient reversal being better indicators. A wide area of strong baroclinicity proves more beneficial for AEW development than a smaller region of intense baroclinicity (Leroux and Hall, 2009). Thorncroft et al. (2008) used a fixed jet and varied the position of the convective trigger and found that the right jet entrance was most effective for generating AEWs. However, the northern flank of the jet moves very little, therefore the standard position for a convective trigger over the Darfur Mountains is nearly always optimal (Leroux and Hall, 2009). Leroux and Hall (2009) used a geographically fixed convective trigger and a variable jet to show that other factors such as the jet strength, its strength in its southern and western extensions and vertical shear are important independently of the location of the convective trigger. The strength of the PV reversal and hence the baroclinicity also plays a role in AEW development, but most importantly an AEW must remain in the baroclinic zone in order to develop.

Using a three-member 22-yr ensemble of simulations, Wu et al. (2009) show that flattened topography causes the AEJ to disappear, essentially merging with the easterly flow associated with the ITCZ, while the monsoonal flow weakens. The absence of topography in northern Africa eliminated any effect induced by the southward sloping terrain over the Sahel and by the Ethiopian Highlands. Increases in surface temperature due to lower elevation and no topographic uplift lead to reductions in precipitation and latent heat flux across the Sahel and eastern Africa. This result emphasizes the likely importance of topography in creating meridional surface temperature gradients. The absence of the low-level temperature gradient leads to the absence of the AEJ, whose existence results from thermal wind balance and the strong meridional low-level temperature gradient, which both directly and indirectly affect the downstream development of AEWs.

1.4 African Easterly Wave Energetics

Energetics analyses for AEWs reveal the processes that lead to the formation of these waves. Previous energetics analyses using observational data (Norquist et al., 1977) and modern reanalyses (Diedhiou et al., 2002) were not able to include realistic diabatic heating, boundary fluxes, and frictional dissipation. Norquist et al. (1977) used data from Phase III of the Global Atmospheric Research Program (GARP) Atlantic Tropical Experiment (GATE) and found that baroclinic conversions are stronger than barotropic conversions over land and the reverse over the ocean. Diedhiou et al. (2002) used 1979-97 National Centers for Environmental Prediction-National Center for Atmospheric Research (NCEP-NCAR) reanalyses and their energetics analyses suggested that 3-5 day easterly waves over land south of the AEJ grow from barotropic instability of the jet, and the waves north of the jet grow from both baroclinic and barotropic conversions below the jet level. Numerical studies (Rennick, 1976; Estoque and Lin, 1977; Thorncroft and Hoskins, 1994a,b) did not include longitudinal variations in a realistic background state. The simplified models with prescribed basic state of the AEJ tend to find that barotropic energy conversions are the main energy source of AEWs (Thorncroft and Hoskins, 1994a,b), while the models with prescribed cumulus convective heating of ITCZ usually find that diabatic heating is the major energy source for the waves (e.g., Estoque and Lin, 1977). Hsieh and Cook (2007) used a regional climate model with convection

parameterized to explore the energetics of AEWs. They found that baroclinic overturning is the dominant energy source, however barotropic energy conversions can be almost equally important when there is concentrated moist convection or shallow cumulus convection below the jet. The formation of AEWs in their model is usually associated with the occurrence of intense rainfall events over Africa, and is usually a result of nearly in-phase baroclinic and barotropic energy conversions.

1.5 Objectives and outline

The objectives of this research are:

- to examine the topographical influences on MCSs by conducting a sensitivity study on an observed MCS
- to examine the topographical influences on AEWs and the two-way interaction between AEWs and West African MCS, and
- to understand why the small offshore region in West Africa experiences such large amounts of rainfall compared to over the land.

I conduct a sensitivity study of the forcing of the AEJ and generation of AEWs, modulated by the two-way interaction between AEWs and West African MCSs. Weather Research and Forecasting (WRF) model simulations are developed for realistic topography and for two sensitivity simulations: one with the height of topography smoothly reduced by 50% and the other with no topography across Africa. For both cases, only the African topography is altered. An observed case study from the United States National Aeronautics and Space Administration (NASA) African Monsoon Multidisciplinary Analysis (NAMMA) field experiment of 2006 is chosen as the reference West African MCS event. I examine the development of the reference MCS in the three simulations in Chapter 2. In Chapter 3, I explore the impacts of topographical influences on the general circulation and conduct an energetics analysis to evaluate the AEW and convective interactions sensitivity to topography. In Chapter 4, I examine the offshore rainfall maximum using Tropical Rainfall Measuring Mission (TRMM) satellite data, the European Center for Medium-Range Weather Forecasts (ECMWF) Reanalyses (ERA)-Interim, and

the WRF sensitivity simulations. A summary of the findings and conclusions are in Chapter 5.

Chapter 2 | A Case Study of Topographic Influence on the Development of West African Mesoscale Convective Systems

2.1 Introduction

Mesoscale convective systems (MCS) are the primary source of rainfall during the West African Monsoon (WAM) (LeBarbé and Lebel, 1997; D'Amato and Lebel, 1998; Laurent et al., 1998; Laing et al., 1999; Nicholson and Yin, 2001; Mathon et al., 2002; Redelsperger et al., 2002; Fink et al., 2006; Guy et al., 2011). Over the Sahel, these convective systems are typically characterized by bow-like convective lines known as squall lines. The variability in seasonal MCS frequency accounts for the difference between dry and wet years in the region (Lebel et al., 1997). The monsoon flow is the main source of moisture for convective activity over West Africa during the rainy season and so plays a major role in determining where MCS are initiated, and the motion of these MCS in turn influences the geographic distribution of rainfall. Rainfall gradients are observed as storms traverse strong thermodynamic gradients in their westward propagation from land to ocean. MCS propagation can be influenced by many different factors, including the distribution of convective available potential energy (CAPE), convective inhibition (CIN), gravity waves, easterly waves, outflow boundaries, and orographic effects (Carlson, 1969a; Zehnder et al., 1999; Thorncroft and Hodges, 2001; Redelsperger et al., 2002; Fink and Reiner, 2003; Baum, 2006; Fink et al., 2006; Nicholson, 2008, 2009; DeLonge et al., 2010).

The lifecycle behavior of West African mesoscale storms poses unique challenges

in determining the sustainability of the storms in land and ocean environments. The principal attributes and associated rainfall characteristics of MCS over West Africa have mainly been illuminated via satellite analyses; Tsakraklides and Evans (2003) used the IR classification system of Evans and Shemo (1996) to contrast the lifecycles of continental and maritime MCS, finding that continental systems were more symmetric and developed more rapidly than their maritime counterparts. Geerts and Dejene (2005) used Tropical Rainfall Measurement Mission (TRMM) data to define the vertical structure (e.g., reflectivity profiles) of MCS. Over land, MCS tend to be deeper and more intense than MCS over maritime regions of West Africa (Fuentes et al., 2008; Guy and Rutledge, 2012). Given the ongoing limitations in ground-based rainfall data in West Africa, satellite-based rainfall data remain an important tool in advancing the understanding of life cycles and precipitation yields of MCS during a period of relatively rapid regional and global environmental changes.

I investigate the influences of topography on MCS development in the West African region in this chapter. Three-dimensional WRF simulations of the event are developed for realistic topography and for two sensitivity simulations in which only the African topography is altered. The model configuration and design of the runs are described in Section 3.2. An observed case study from the United States National Aeronautics and Space Administration (NASA) African Monsoon Multidisciplinary Analysis (NAMMA) field experiment of 2006 is chosen as the reference MCS event and described in Section 3.3. The results of the model simulations are discussed in Section 3.4. Section 3.5 concludes with a summary of the findings and some brief discussion.

2.2 Numerical Model Configuration and Design of Sensitivity Runs

To determine how topography influences the initiation and development of MCSs in the study region the WRF model was used to create simulations in three scenarios; realistic topography (hereafter called TOPO), topographic height smoothly reduced by 50% (hereafter called HALF), and no topography (hereafter called FLAT). Only the topography over Africa was altered; all other landmasses in the domain retain

realistic topography. The terrain modification begins at sea level (e.g. Suez and Gibraltar) so that no terrain slope artifacts are introduced.

The WRF model version 3.5.1 with WRF Preprocessing System (WPS) version 3.5 is used in this study (Skamarock et al., 2008). Three one-way nested domains are employed with grid spacing of 36, 12, and 4 km, respectively. Each domain has 42 vertical levels extending up to 50 hPa and spaced to provide higher resolution in the lowest 1.5 km of the atmosphere (about 19 vertical levels). The outer domain (D1) spans the continent of Africa and parts of Arabia, Europe and Brazil (Fig. 2.1). The second domain (D2) covers most of West Africa, extending from 32°W to 2°E longitude and 3°S to 25°N latitude (Fig. 2.1). The innermost domain (D3) covers Senegal, Gambia, Guinea-Bissau, and parts of Guinea, Sierra Leone, Mauritania, and Mali (Fig. 2.1). All three model domains used the Dudhia shortwave radiation scheme (Dudhia 1989), the Rapid Radiative Transfer Model (RRTM) longwave radiation scheme (Mlawer et al., 1997), the WRF Single Moment 6-class (WSM6) microphysics scheme (Hong and Lim, 2006), the Noah land surface scheme (Chen and Dudhia, 2001), and the Yonsei University (YSU) ABL scheme (Hong et al., 2006) with the Monin-Obukhov surface layer scheme (Monin and Obukhov, 1954). The Grell-Freitas convective parameterization (Grell and Freitas, 2013) was only employed in the first and second domains (36 and 12 km). The convective parameterization was turned off in the inner domain.

European Centre for Medium-Range Weather Forecasting (ECMWF) Reanalysis (ERA) Interim data are used to prescribe the WRF initial and boundary conditions. The spatial resolution of the ERA-Interim data is approximately 80 km (T255 spectral) on 60 vertical levels from surface up to 0.1 hPa. The NAMMA field campaign of August-September 2006 observed various MCS developments in West Africa. We simulate a case observed on 30-31 August 2006. The WRF model is initialized at 0000 UTC 25 August and ran to 0000 UTC 2 September, a total of eight days (192 hours) of simulation time. Although the MCS case of interest did not develop until 30 August, it interacted with an AEW during its evolution. Thus, the simulations were initialized five days earlier to allow for the evolution of the AEW to respond to the topographic forcing variations in the sensitivity simulations. It is important to note that these simulations are not forecasts due to the extended lead time between initialization of the model and the storm's occurrence. The statistics and analyses of these simulations exclude the first 12

hours of each simulation to account for model spinup.

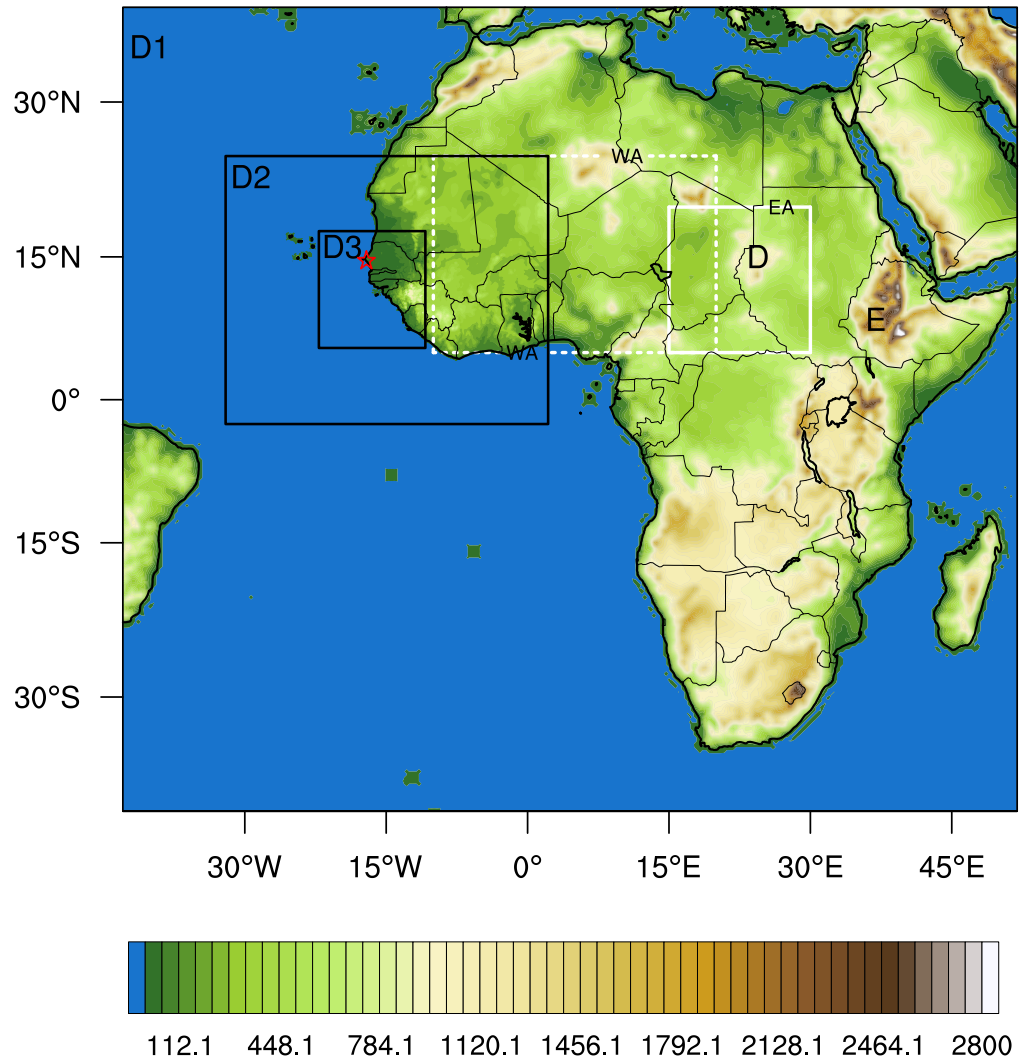


Figure 2.1. Model terrain height in meters from WRF model. The outer domain has a grid spacing of 36 km. The second domain has a grid spacing of 12 km and the inner domain has a grid spacing of 4 km. The dashed and solid white boxes highlight the domains marked as West Africa (WA; 5-25°N, 10°W-20°E) and East Africa (EA; 5-20°N, 15-30°E) respectively, used in the energetics analysis. The letter D marks the location of the Darfur Mountains and E marks the location of the Ethiopian Highlands. The location of the research site during the NASA African Monsoon Multidisciplinary Analysis (NAMMA) field campaign is marked by the red star.

2.3 Observed Case Description (OBS)

During August and September 2006, the NAMMA field campaign observed a series of MCS developments. These data provide high temporal resolution and detailed boundary layer measurements at the experiment site and serve to supplement larger-scale analyses based on satellite retrievals and model fields. We select a case observed on 30-31 August 2006 that encompasses a developing AEW traversing West Africa and, generating a well-observed MCS (DeLonge et al., 2010). The data used to analyze this case are summarized now, then the development of the AEW and MCS are described.

2.3.1 Satellite Data

The Version 7 TRMM Multi-satellite Precipitation Analysis (TMPA) 3B42, was analyzed for this study. This dataset is developed with rainfall estimates from geostationary infrared (IR) observations, then adjusts these estimates using an optimal combination of inputs from the TRMM and polar orbiting satellites. The final gridded precipitation rates [p (mm hr^{-1})] and precipitation-error estimates (mm hr^{-1}) have a 3-hour temporal resolution and a $0.25^\circ \times 0.25^\circ$ spatial resolution in a global belt extending from 50°S to 50°N (Huffman et al., 2007).

2.3.2 Field Experiment Site Description and Data Collected

A research site was established in Kawsara, Senegal (14.66°N , 17.10°W) during August and September 2006 as part of the NAMMA field campaign (Fig. 2.1). The research site is located 10 km inland and 40 km southeast of Dakar, Senegal. The site is situated in a relatively flat landscape (74 m above sea level) in the semi-arid Sahel savannah. This site is in the center of a climatological meridional rainfall gradient and on the cooler edge of an east-to-west temperature gradient in Senegal (Nzeukou and Sauvageot, 2002; Fall et al., 2006).

Rawinsondes launched at the research site recorded measurements of air temperature, pressure, relative humidity, wind speed, and wind direction were recorded every 2 s during ascent (DeLonge et al., 2010). The soundings that were analyzed in this study were launched on 30 August (1758 UTC), 31 August (0000, 0501, 0907, 1152, and 1806 UTC), and 1 September (0148, 0624, and 1702 UTC). Specific

humidity (q , in g kg^{-1}), virtual potential temperature (θ_v , in K), and equivalent potential temperature (θ_e , in K) were calculated from the rawinsonde measurements and used to investigate the thermodynamic and dynamic states of the atmosphere before and after the MCS passage. This suite of observations are used to evaluate the model results.

2.3.3 AEW and MCS Event of 30-31 August 2006

The MCS in this case study was a well-organized, fast-moving squall line with the expected features: a strong gust front, a bow-shaped convective leading edge, and an extensive trailing stratiform region. It originated to the northeast of Kawsara, Senegal around 1400 UTC on 30 August 2006 in the highland regions near Mali and passed over the research site at 0805 UTC (equivalent to local standard time in this region) on August 31, 2006. The MCS developed and strengthened as it approached the coast of Senegal during the overnight hours and crossed the coastline during the early morning of 31 August 2006 (Fig. 2.2). Six-hourly wind vectors and meridional wind at 700 hPa from ERA-Interim data identify the AEW and its trough axis just ahead of the MCS (Fig. 2.2a). MCSs are known to move with and through AEWs and there may be periods when the convection aids in the intensification of the waves and vice versa (Fink and Reiner, 2003; Fink et al., 2006; Laing et al., 2008).

The MCS moved southwesterly towards the Senegalese coast and at 0000 UTC on 31 August 2006 took on the shape of a squall line (Fig. 2.2). Between 0000 and 0600 UTC, the MCS propagated into the region west of the wave trough, where convection is associated with maximum low-level convergence and cyclonic vorticity (Reed et al., 1977; Fink and Reiner, 2003; Fink et al., 2006). At 0600 UTC 31 August, the system approached the coastline; TRMM observations register convective rainfall ($\geq 3.2 \text{ mm hr}^{-1}$) in the leading edge of the squall line and lighter rainfall falling from the trailing stratiform region (Fig. 2.2c). By 1200 UTC, IR images show that the leading edge of the squall line crossed the coastline while the stratiform deck still straddled the Senegalese coast. The convective squall line maintained its organization as it continued moving southwest, however it began to break away from the stratiform deck after reaching the coast, and the squall line became less organized and weakened over the Atlantic Ocean. The stratiform region passed over the site by 1300 UTC (Fig. 2.2e). For a more comprehensive

description and discussion of the observed MCS, the reader is referred to DeLonge et al. (2010).

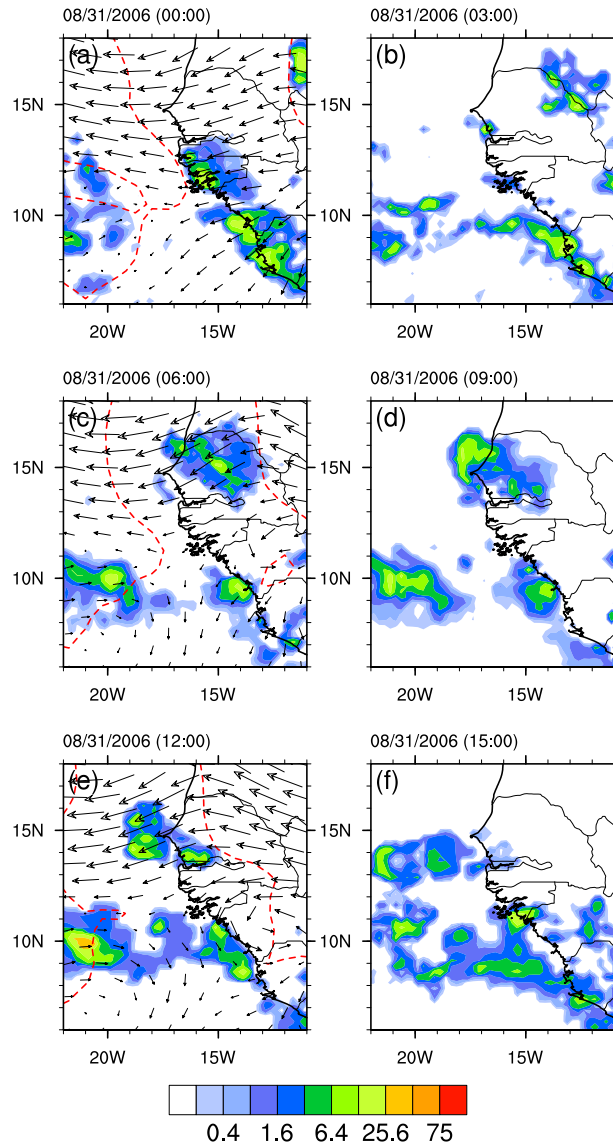


Figure 2.2. Three-hourly precipitation rates (mm hr^{-1}) from TRMM showing the lifecycle of the observed MCS case study on 31 August 2006 at (a) 0000 UTC, (b) 0300 UTC, (c) 0600 UTC, (d) 0900 UTC, (e) 1200 UTC, and (f) 1500 UTC. Note the MCS is located in the top right corner of panel (a) and travels southwesterly towards the Senegalese coast. Arrows indicate 700 hPa wind vectors and the red dashed contour indicates where the 700 hPa meridional wind is zero from six-hourly ERA-Interim data.

Rawinsonde observations indicate the research site was experiencing warm and very moist atmospheric conditions before the approach of the MCS with a deep, moist layer extending up to 850 hPa (Fig. 2.3a-c). The onshore flow extending up to 950 hPa is primarily responsible for these thermodynamic conditions (Fig. 2.4). In the mid-levels, the rawinsonde indicates a jet core at about 600 hPa with a wind speed maximum of 16 m s^{-1} (Fig. 2.4a). During the passage of the storm, the low-level flow became easterly simultaneous with an intensification in the wind speed (Fig. 2.4b). The rawinsonde measured total wind speeds as high as 28 m s^{-1} at low-levels, with the maximum elevated about 1 km above the surface (Fig. 2.4a). Changes in the mid-levels immediately after the system passage were not observed because the rawinsonde launched into the storm at 0907 UTC 31 August failed at around 800 hPa. The θ_v indicates the presence of a cold pool near the surface as the squall line passes over the research site (Fig. 2.3a). Both θ_e and q indicate the transport of cool, dry mid-level air to the surface through convective downdrafts (Figs. 2.3b-c). By the next rawinsonde launch, more than two hours later, the wind speeds have begun to subside but the cooler and drier thermodynamic conditions still prevail (Figs. 2.3a-c and 2.4a-b). The convective leading edge of the squall line crossed the coastline by 1200 UTC, marked by a gradual change in the wind at the site. The stratiform deck, however, extended back over land until 1300 UTC, so stratiform rainfall still contributed to evaporatively-cooled air at low-levels over the site. The low-level air begins to warm and moisten by 1806 UTC, after the complete passage of the squall line past the site (Fig. 2.3a-c). By 1 September, the observations indicate the presence of a strong AEJ core over the site, the low-level winds begin to revert back to westerlies and the thermodynamic conditions resemble those of the pre-MCS conditions (Figs. 2.3a-c and 2.4a-b).

2.4 Simulations of MCS

All discussion on the simulated MCS analyses are based on the innermost domain with the finest horizontal resolution of 4 km, while all analyses on the AEJ and AEW are conducted on domains D1 and D2 in order capture the features on a regional field.

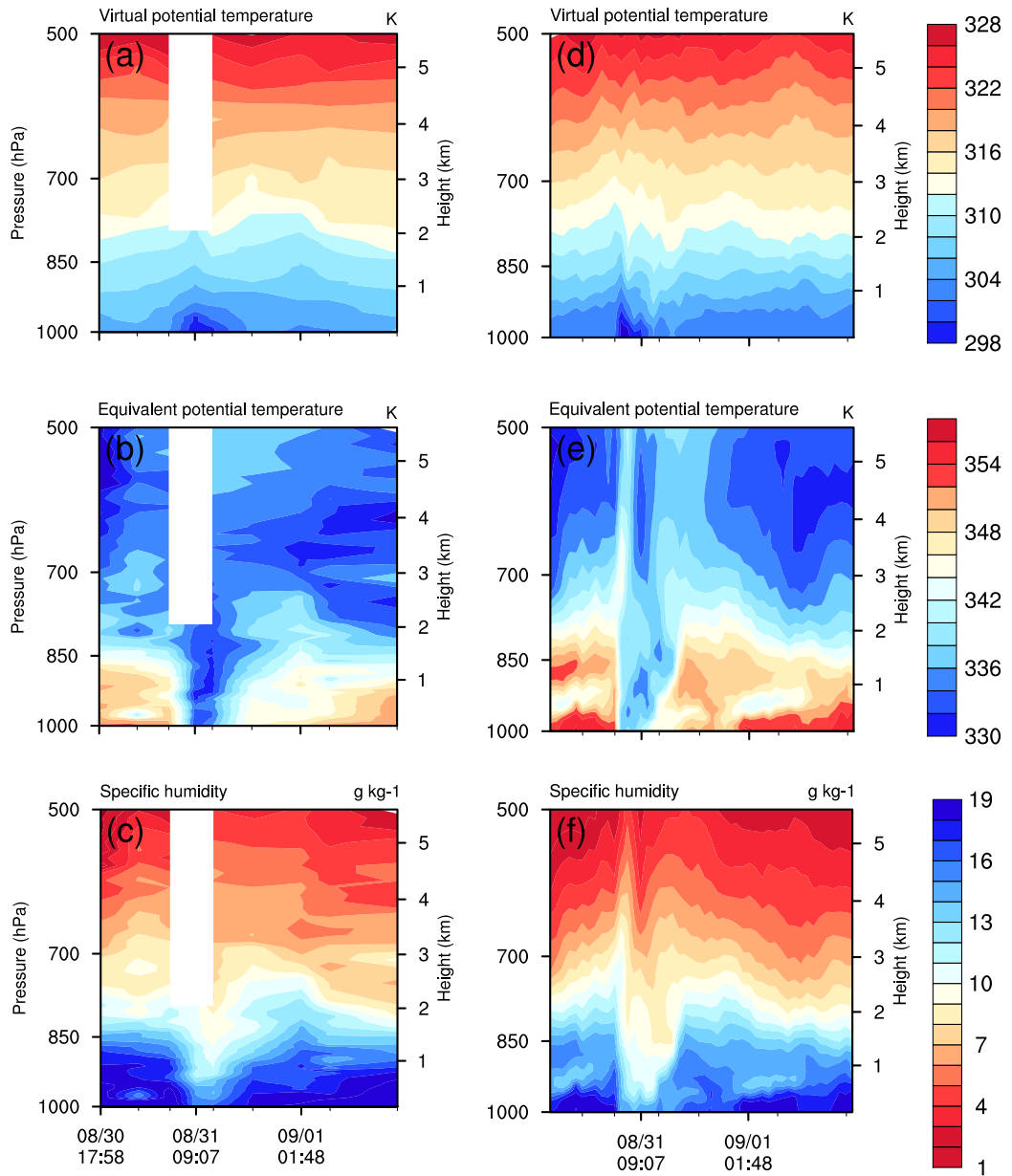


Figure 2.3. Time series of the (a) virtual potential temperature, (b) equivalent potential temperature, and (c) specific humidity measured by the rawinsondes at the research site on 30 August at 1758 UTC, 31 August at 0000, 0501, 0907, 1152, 1806 UTC, and 1 September at 0148, 0624, and 1702 UTC. The 0907 rawinsonde failed shortly after launch. Time series of the (d) virtual potential temperature, (e) equivalent potential temperature, and (f) specific humidity from the TOPO run from 1900 UTC 30 August to 1800 UTC 01 September at 1 hour intervals.

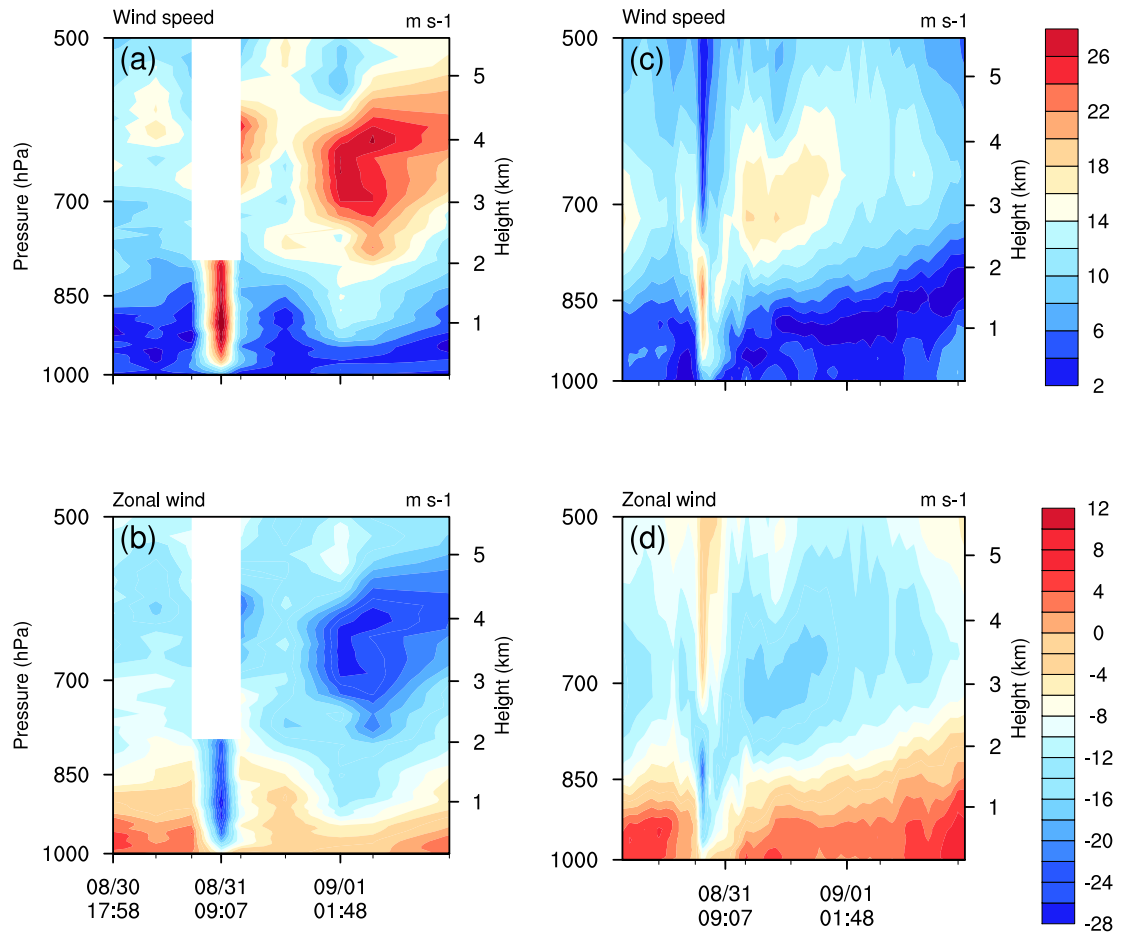


Figure 2.4. Time series of the (a) total wind speed and (b) zonal wind speed measured by the rawinsondes at the research site on 30 August at 1758 UTC, 31 August at 0000, 0501, 0907, 1152, 1806 UTC, and 1 September at 0148, 0624, and 1702 UTC. The 0907 failed shortly after launch. Time series of the (c) total wind speed and (d) zonal wind speed from the TOPO run from 1900 UTC 30 August to 1800 UTC 01 September at 1 hour intervals.

2.4.1 Control simulation (TOPO)

The TOPO WRF simulation considers two convective systems that merge to form a squall line that eventually resembles the observed squall line (Fig. 2.5). At 1700 UTC 30 August a collection of afternoon convective cells develop northeast of the research site in Mauritania (near 16°N, 12°W), relatively close to where the observed MCS initiated. The convective cells merge and develop into an organized squall line between 2000 UTC and 2200 UTC (MCS-A in Figs. 2.5a-b). Meanwhile,

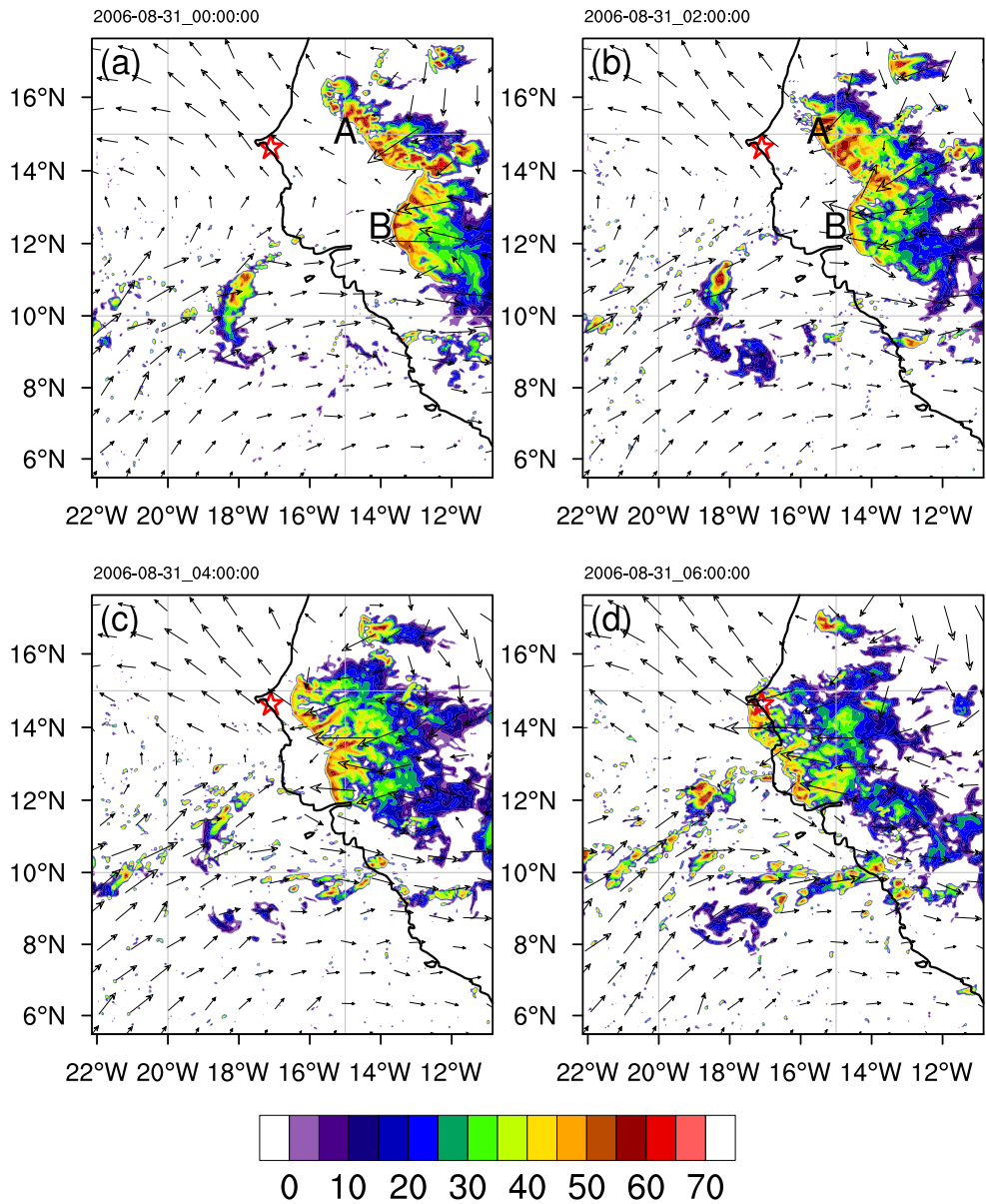


Figure 2.5. Maximum reflectivity in dBZ (shaded) and winds at 850 hPa (vectors) in domain 3 from the TOPO simulations for (a) 0000 UTC, (b) 0200 UTC, (c) 0400 UTC, and (d) 0600 UTC on 31 August 2006. The location of the research site is marked by the red star at 14.66°N, 17.10°W.

another squall line associated with a weak AEW propagates westward towards the coast (MCS-B in Figs. 2.5a-b). The 650-hPa meridional wind shows a weak wave trough where the winds shift from southerlies to northerlies near 12°W (Fig. 2.7a). That squall line (centered at 12.5°N) propagates into the third domain by 1900

UTC 30 August and is located west of the 650-hPa AEW trough axis.

By 2300 UTC the two MCSs merge and continue to develop and strengthen as the resulting squall line travels westward toward the coast (Fig. 2.5a). Low-level convergence (between 0 and 1 km) is occurring ahead of the MCS supporting inflow into the storm (Fig. 2.6a,b). The squall line possesses a strong convective leading edge extending up to 14 km high in the atmosphere (Fig. 2.6a,b). The leading edge of the squall line reaches the location of the research site at 0540 UTC 31 August in the TOPO simulation, a bit earlier than was observed (DeLonge et al., 2010). The TOPO squall line shows signs of weakening as it approaches the coast due to

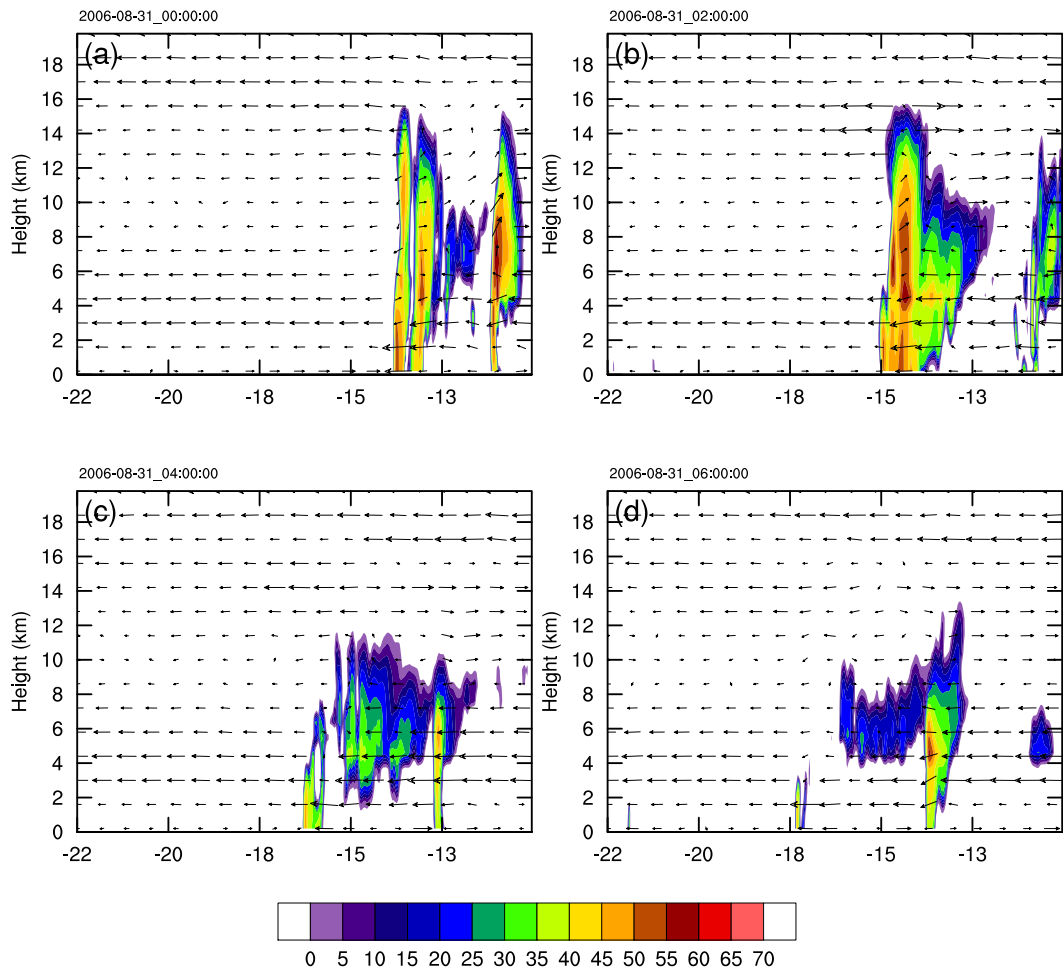


Figure 2.6. Vertical cross section of reflectivity in dBZ (shaded) and total wind vectors in domain 3 from the TOPO simulations for (a) 0000 UTC, (b) 0200 UTC, (c) 0400 UTC, and (d) 0600 UTC on 31 August 2006 along 14.66°N.

reduced convergence ahead of the storm; mainly because the low-level onshore flow weakens significantly ahead of the squall line (Figs. 2.5c-d, 2.6c-d). The onshore flow close to the surface begins weakening at 0200 UTC (Fig. 2.6b), leading to a reduction in moisture convergence and moist inflow into the storm that would otherwise help to sustain the system. When the northernmost edge of the squall line crosses the coastline at 0600 UTC the entire system shows signs of weakening and disorganization. The entire leading edge crosses the coastline by 0740 UTC. The cold pool outruns the storm as it crosses the coastline, cutting off the warm, moist inflow that had been feeding the MCS, so the MCS weakens, becomes less organized and disintegrates.

Ahead of the MCS, the atmospheric boundary layer over the research site is warm ($\theta_v = 302\text{-}304$ K up to 0.5 km) and moist (19 g kg⁻¹ up to 0.5 km) (Figs. 2.3d and f). These conditions prevail due to the westerly onshore flow (4 m s⁻¹) that also transports high θ_e inland (> 346 K up to 850 hPa) (Figs. 2.3e and 2.4b). As the simulated MCS approaches the research site location, the zonal wind shifts (westerly to easterly), wind speed increases, and q , θ_v , and θ_e decrease between 0500 and 0600 UTC 31 August (Figs. 2.3d-f).

The TOPO simulation produces a deeper moist and unstable boundary layer than that indicated in the rawinsonde observations (Figs. 2.3d-f). Moreover, the onshore flow over the research site is stronger and deeper in the TOPO simulation than in the observations (Figs. 2.4b, d). Similar to the rawinsonde observations, the time series show a strengthening of the easterlies at low-levels to 24 m s⁻¹ at 0600 UTC, but the observations show stronger winds. The weaker reduction in θ_e in TOPO compared to the observations suggests that the convective downdrafts are weaker in that simulation (Figs. 2.3b,e). The intensification of the AEJ after the passage of the MCS is also weaker in the simulation and occurs much sooner (within 6 hours) compared to the observations (within 14 hours). Due to the track of the storm in this simulation the northern edge of the simulated squall line passes over the location of the research site, while radar observations indicate the central portion of the observed squall line crossing the site (DeLonge et al., 2010). However, changes in atmospheric conditions during the passage of the simulated MCS at a model location near the mid-point of the leading edge are comparable with the changes observed at the study site.

Overall, the WRF model generally captures the main features of the storm case

study; it produced a squall line with similar features and track to the observed case. The model simulation provides a continuous outlook on the effects the MCS has on its surrounding environment and vice versa through time contrary to the rawinsonde observations. The atmospheric conditions at the research site returned to pre-MCS conditions about 2 to 4 hours sooner after the MCS passage in the

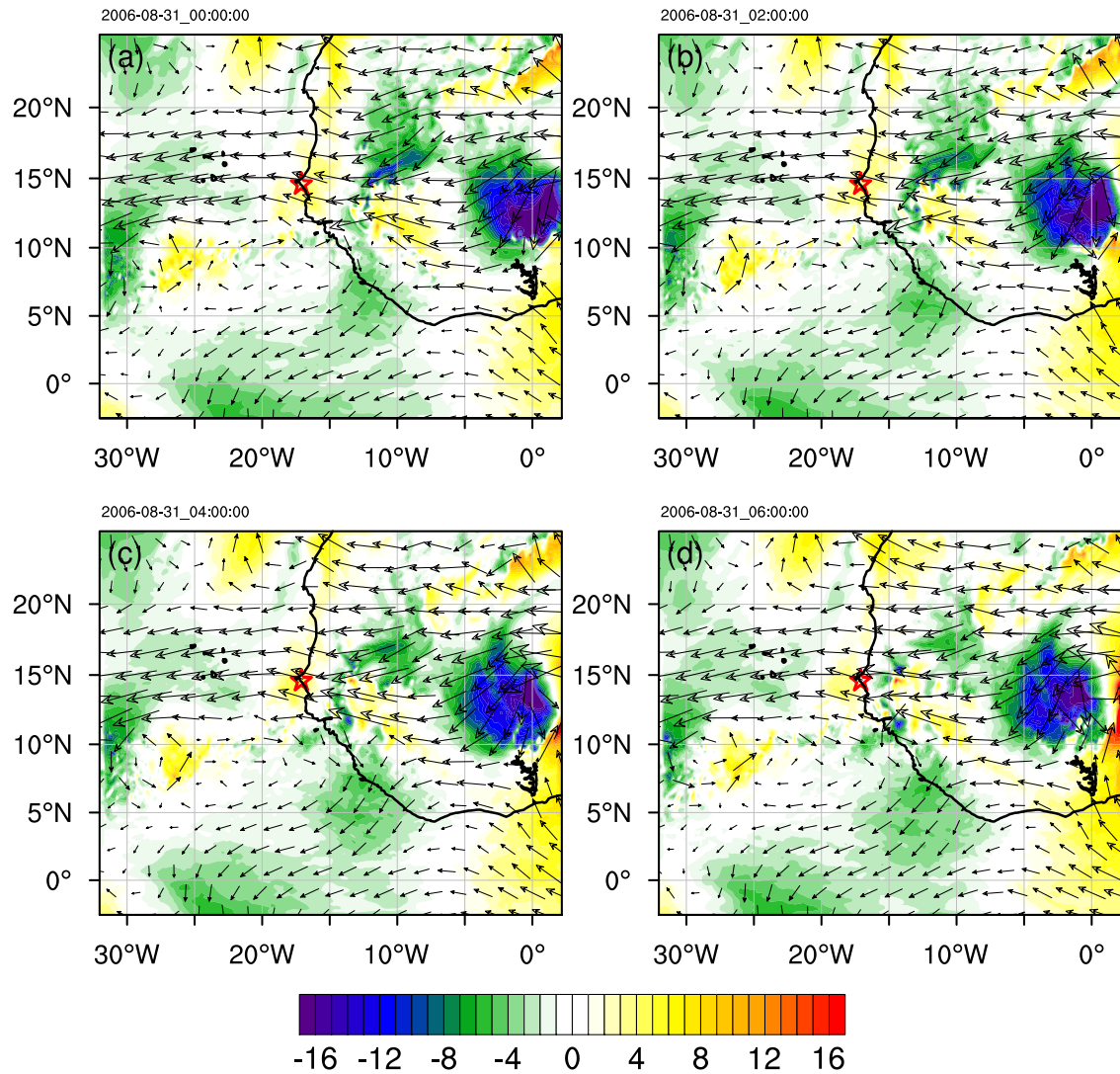


Figure 2.7. Meridional winds (shaded) and total wind (vectors) at 650 hPa in domain 2 from TOPO simulation for (a) 0000 UTC, (b) 0200 UTC, (c) 0400 UTC, and (d) 0600 UTC on 31 August 2006. The location of the research site is marked by the red star at 14.66°N, 17.10°W.

simulation than the observations. The simulated TOPO MCS was short-lived after reaching the coast compared to the observed system, and the lack of a persistent stratiform clouds over the study site allowed the low- to mid-level atmosphere to return to pre-MCS conditions sooner in the TOPO simulation.

2.4.2 HALF simulation

The MCS in the HALF run results from the accumulation and merger of strong convective cells (maximum reflectivity ≥ 50 dBZ) that develop around 1720 UTC on 30 August similar to the observed and TOPO MCSs (Fig. 2.8a). The cells initiate east and southeast of the research site and merge into a squall line by 2300 UTC (Fig. 2.8a,b). The cells located east of the research site extend between 12 to 14 km deep in the vertical with maximum reflectivities between 55 and 65 dBZ (Fig. 2.9a,b). As the squall line propagates westward towards the coast it develops a long leading edge extending about 500 km and has maximum reflectivity values exceeding 50 dBZ (Fig. 2.8c), the same as TOPO and OBS. The HALF MCS develops and propagates quicker than the systems in TOPO and OBS. The 650-hPa meridional winds indicate the presence of a wave trough axis to the east of the MCS located near 10°W (Fig. 2.10). However, the wave appears to stall over the period of the storm's existence, causing the 650-hPa winds over the research site to be purely zonal (Fig. 2.10).

By 0000 UTC 31 August the northern portion of the squall line is showing signs of weakening (Figs. 2.8c, 2.9c). The near-surface wind vectors in Figure 2.9c indicate that low-level convergence is occurring about 100 km ahead of the convective storm, which suggests the storm's cold pool has ran ahead of the storm and is ultimately cutting the storm off from moist inflow. The leading edge of the squall line is over the research site by 0200 UTC, 4 hours earlier than when the squall line in TOPO reached the site (Fig. 2.8d). Weaker convergence ahead of the squall line leads to weaker inflow into the system and the MCS begins to weaken and becomes disorganized as it approaches the coastline (Figs. 2.8d, 2.9d). By 0400 UTC the squall line disintegrates as it crosses the coastline.

The MCS modeled in this simulation had similar features to the simulated MCS in TOPO and OBS. The MCS, however, is the result of afternoon convective heating and hence the storm is short-lived. The MCS is located to the far west of

a trough that contributed little to the development of the MCS in this simulation. Hence, the change in topography changed the role of the AEW in the life cycle of the West African MCS.

2.4.3 FLAT simulation

A MCS forms on 1940 UTC 28 August at 12°N, 5°W and propagates westward ahead of an AEW. The MCS cycles through periods of decay and regeneration until it gets to 12.5°N, 10°W at 0500 UTC 30 August, when it finally develops into the system that propagates towards the coast. By 1200 UTC the system develops into a squall line, which stays to the west of the 850-hPa AEW vortex (Fig. 2.11) and ahead of the AEW trough (Fig. 2.12). The flow at 850 hPa shows the presence of the low-level circulation associated with the AEW (Fig. 2.11). Along with that low-level circulation there is a strong onshore flow towards the storm, which provides low-level moist convergence and inflow into the MCS. At 0000 UTC 31 August the vertical cross section along 14.66°N slices through the strongest cell in the squall line, which extends up to 14 km high with maximum reflectivity of 60-65 dBZ measured at 5 km (Fig. 2.13a).

The leading edge of the MCS begins to disintegrate when it reaches the research site at 0400 UTC 31 August (Fig. 2.11c). There is a break in the northern portion of the squall line at that time and there is weaker low-level (surface to 850 hPa) convergence ahead of that portion of the squall line (Figs. 2.11c-d, 2.13c-d). The system crosses the coastline completely by 1140 UTC 31 August and dissipates over the Atlantic Ocean by around 1700 UTC.

The FLAT simulation proved to provide the best environment for the simulated MCS to develop in with a strong onshore flow, and low-level convergence and cyclonic vorticity associated with a low-level AEW vortex. This allowed the system to survive the transition from the land to ocean environment better than the other two simulated MCS.

2.5 Conclusion

The WRF model was used to demonstrate the topographic influences on the development of the AEJ, AEWs and the resulting MCS in West Africa. The MCS

from TOPO and HALF possessed similar features to the observed MCS during August 30-31, 2006. The MCSs in the TOPO and HALF simulations were both ahead of a weak AEW trough. The MCS from the FLAT run also possessed similar features but was strongly associated with an AEW vortex. The model's persistence in simulating these MCSs in conjunction with AEWs highlights the robustness of the well-known connection between the two systems in West Africa. The development of the simulated MCSs differ in each run due to their interaction with the AEW and the onshore flow that are in turn impacted by the topography. The removal of the coastal topography allowed the onshore flow to travel further inland unimpeded, which help to sustain the MCS in the FLAT run.

These results led to further investigation into how the removal of topography affected the generation and growth of AEWs in the next chapter. Since the observed MCS case was associated with an AEW, it is of interest how the changes in AEW activity affect the development of this particular storm and general MCS development in tropical north Africa. An energetics analysis is conducted in Chapter 3 to examine why the modeled AEWs and their associated MCSs behave differently in the sensitivity simulations.

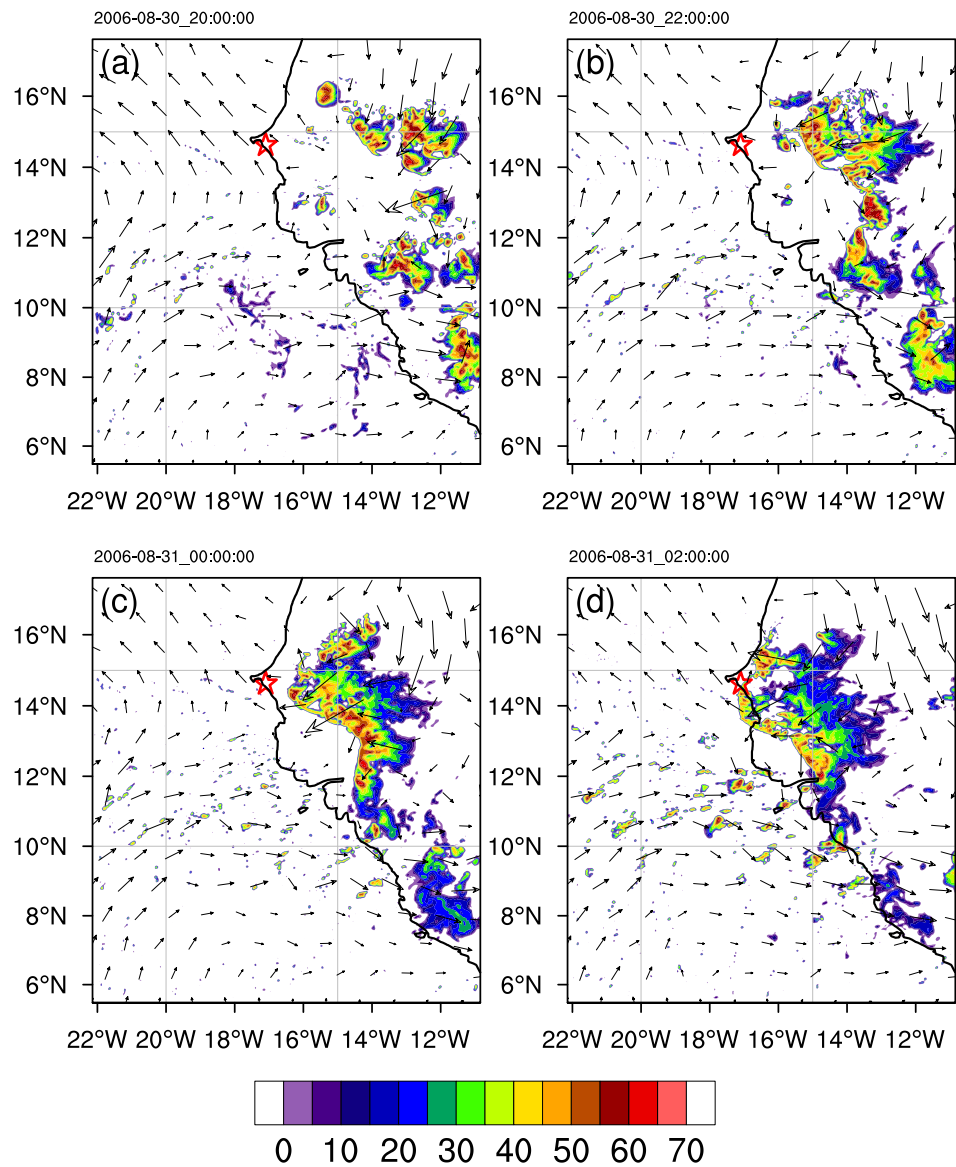


Figure 2.8. Maximum reflectivity in dBZ (shaded) and winds at 850 hPa (vectors) in domain 3 from the HALF simulation for (a) 2000 UTC, (b) 2200 UTC on 30 August, and (c) 0000 UTC and (d) 0200 UTC on 31 August 2006. The location of the research site is marked by the red star at 14.66°N, 17.10°W.

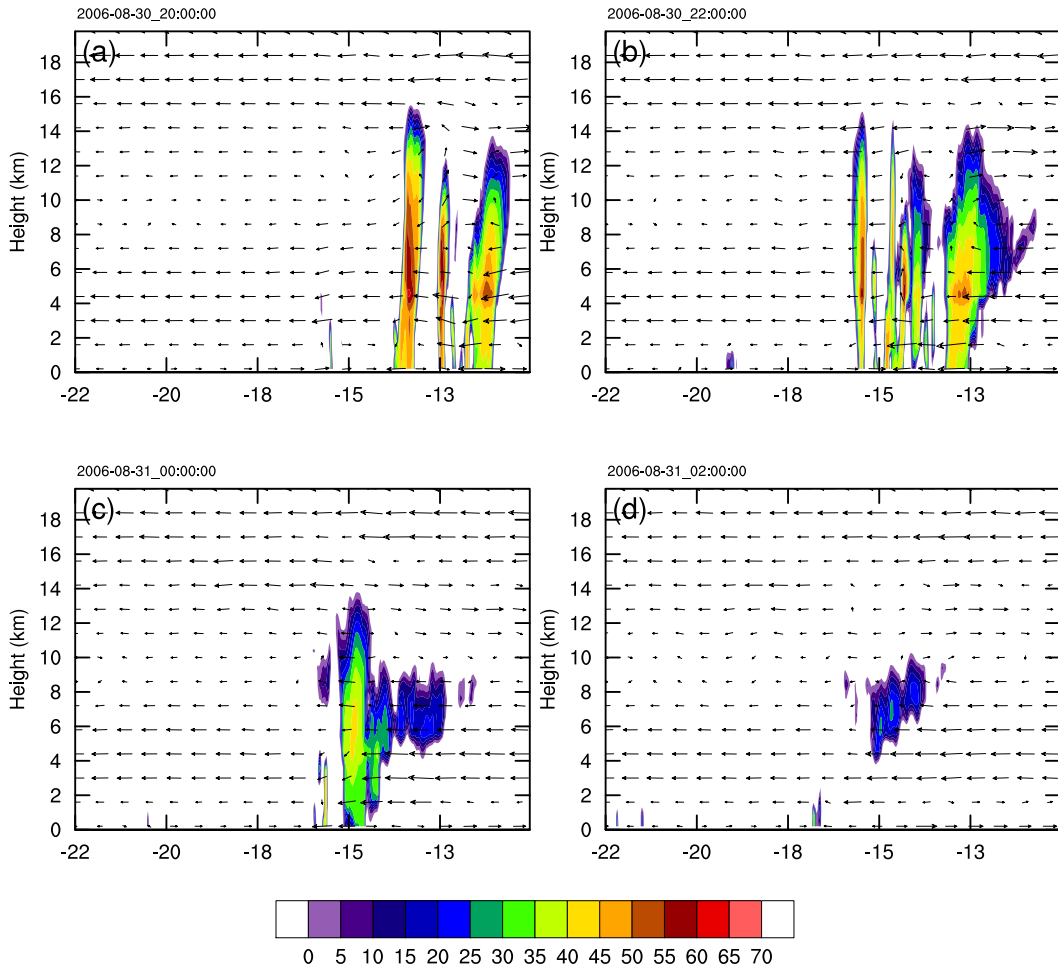


Figure 2.9. Vertical cross section of reflectivity in dBZ (shaded) and total wind vectors in domain 3 from the HALF simulations for (a) 2000 UTC, (b) 2200 UTC on 30 August, and (c) 0000 UTC and (d) 0200 UTC on 31 August 2006 along 14.66°N.

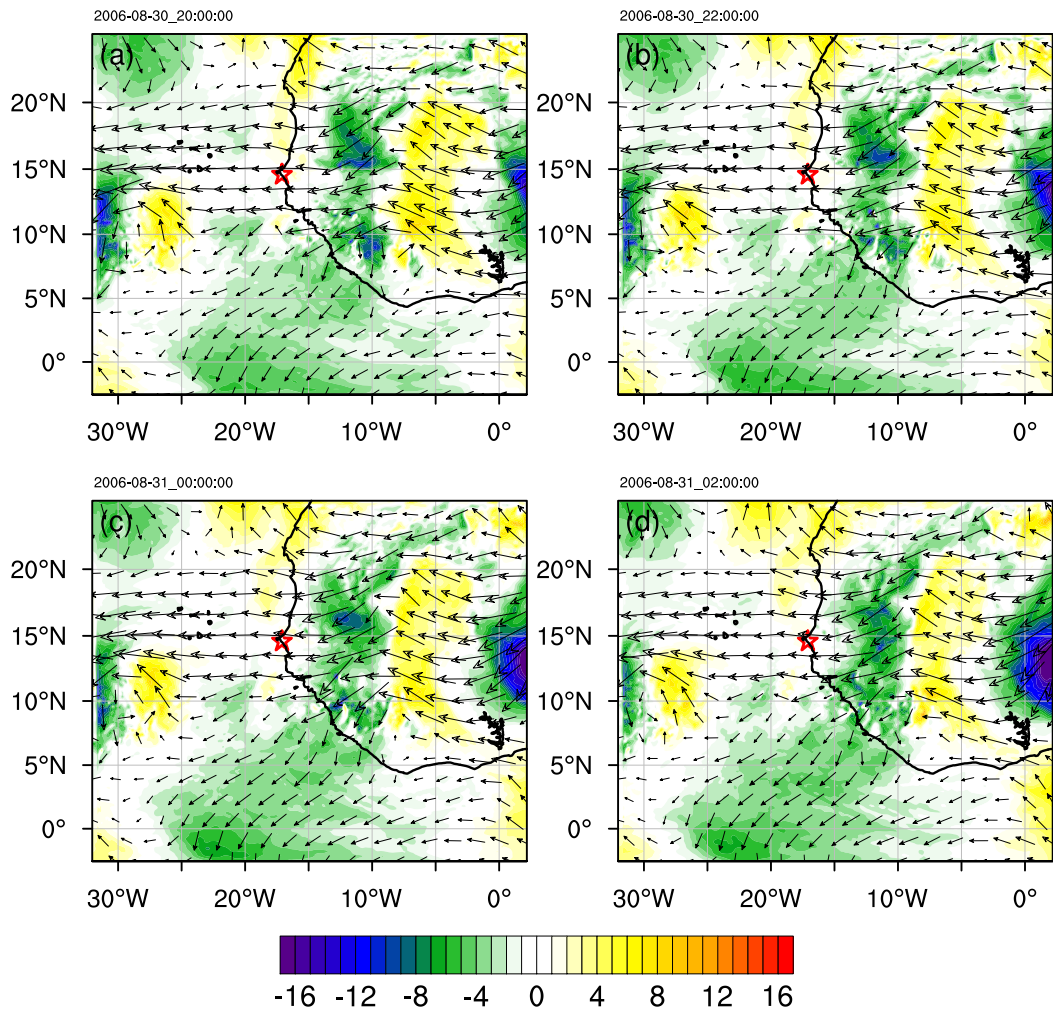


Figure 2.10. Meridional winds (shaded) and total wind (vectors) at 650 hPa in domain 2 from HALF simulation for (a) 2000 UTC and (b) 2200 UTC on 30 August, and (c) 0000 UTC and (d) 0200 UTC on 31 August 2006. The location of the research site is marked by the red star at 14.66°N, 17.10°W.

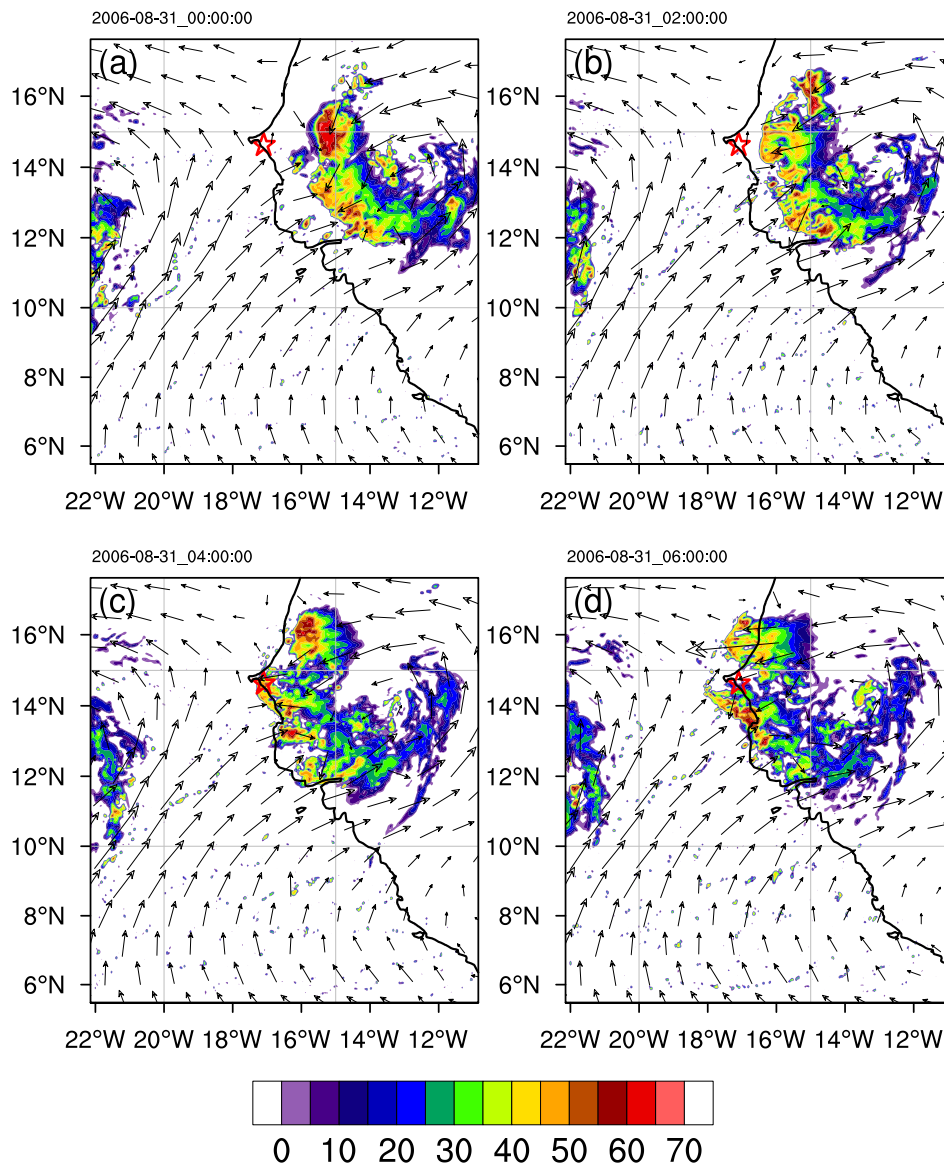


Figure 2.11. Maximum reflectivity in dBZ (shaded) and winds at 850 hPa (vectors) in domain 3 from the FLAT simulation for (a) 0000 UTC, (b) 0200 UTC, (c) 0400 UTC, and (d) 0600 UTC on 31 August 2006. The location of the research site is marked by the red star at 14.66°N, 17.10°W.

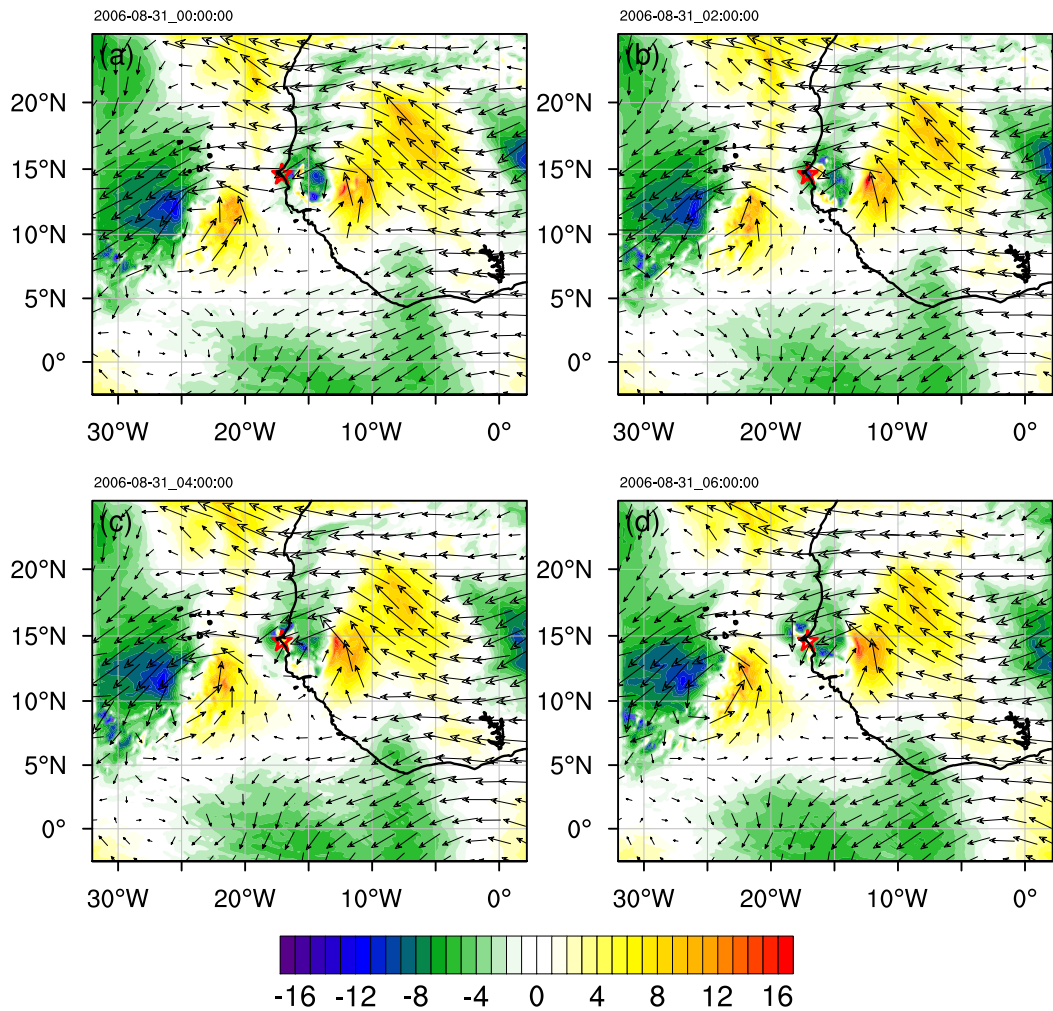


Figure 2.12. Meridional winds (shaded) and total wind (vectors) at 650 hPa in domain 2 from FLAT simulation for (a) 0000 UTC, (b) 0200 UTC, (c) 0400 UTC, and (d) 0600 UTC on 31 August 2006. The location of the research site is marked by the red star at 14.66°N, 17.10°W.

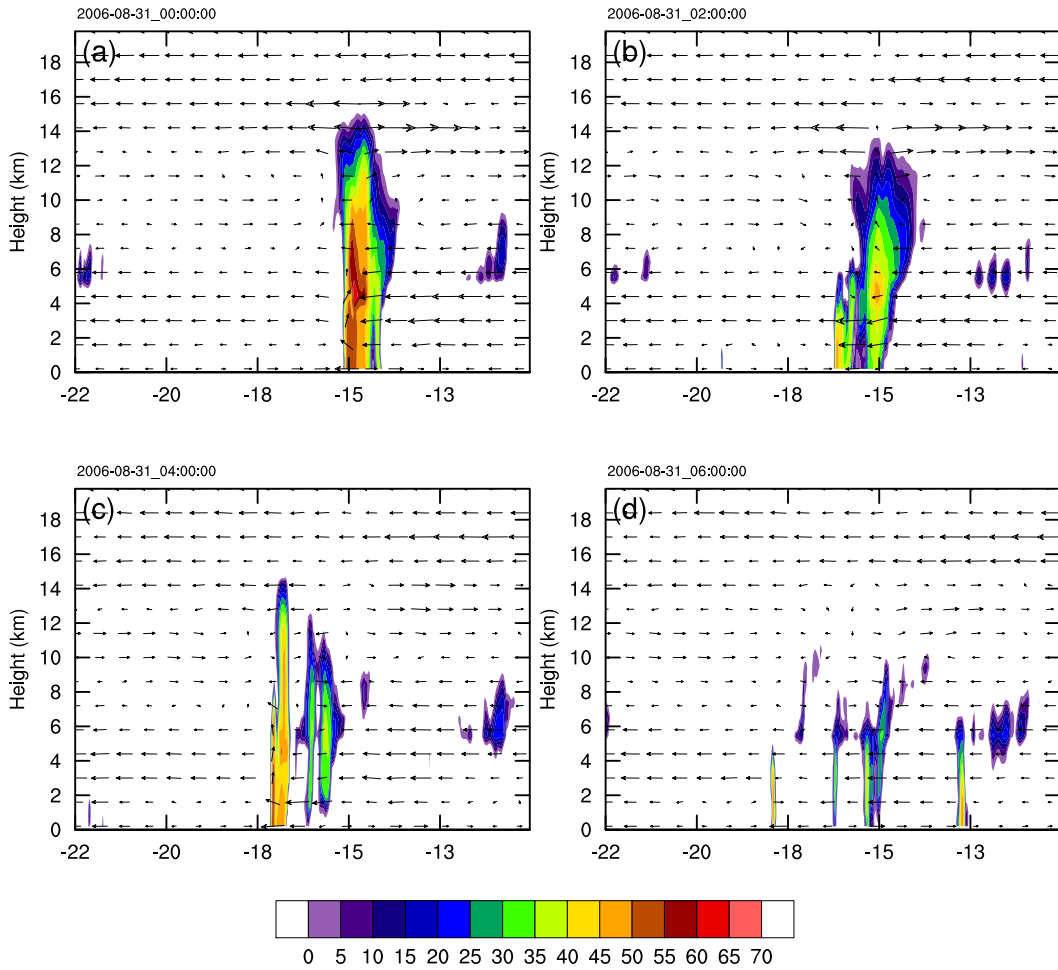


Figure 2.13. Vertical cross section of reflectivity in dBZ (shaded) and total wind vectors in domain 3 from the FLAT simulations for (a) 0000 UTC, (b) 0200 UTC, (c) 0400 UTC, and (d) 0600 UTC on 31 August 2006 along 14.66°N.

Chapter 3 | Topographic Influence on AEW Energetics and Convective Interactions

3.1 Introduction

African Easterly Waves (AEWs) are the dominant type of synoptic disturbance over tropical North Africa and the tropical north Atlantic during the summer (Reed et al., 1977; Thompson et al., 1979; Thorncroft and Hodges, 2001; Kiladis et al., 2006; Lafore et al., 2011). AEWs are convectively triggered in East and Central Africa (between 15°E and 30°E) downstream of the high terrain of the Ethiopian Highlands and the Darfur Mountains (E and D in Fig. 2.1), and grow through mixed barotropic-baroclinic instability of the African Easterly Jet (AEJ) (Burpee, 1972; Hodges and Thorncroft, 1997; Pytharoulis and Thorncroft, 1999; Berry and Thorncroft, 2005; Hall et al., 2006; Skinner and Diffenbaugh, 2013). Observations of vorticity maxima show that AEW activity occur along two parallel tracks—one to the north of the African Easterly Jet (AEJ) and one to the south over the continent—that later merge over the Atlantic Ocean (Carlson, 1969a; Reed et al., 1977; Diedhiou et al., 1998; Thorncroft and Hodges, 2001; Pytharoulis and Thorncroft, 1999; Redelsperger et al., 2002; Nicholson, 2009). The southern-AEWs have maximum amplitude close to the AEJ level and a low-level vorticity maximum near 850 hPa, and are often associated with moist convection (Carlson, 1969a; Burpee, 1972; Reed et al., 1977; Pytharoulis and Thorncroft, 1999; Thorncroft and Hodges, 2001; Redelsperger et al., 2002; Baum, 2006; Nicholson, 2008, 2009; Zawislak and Zipser, 2010). Northern-AEWs are shallow low-level waves that are primarily characterized by dry convective processes, however, they too are capable of influencing precipitation variability in the Sahel through moisture advection

within the southerly flow of their low-level vortex (Gu et al., 2004).

Consistent with the Charney and Stern (1962) instability criterion, the southern-AEWs develop along the reversed meridional potential vorticity (PV) gradient near the AEJ core (Burpee, 1972; Pytharoulis and Thorncroft, 1999). These southern-AEWs are driven by barotropic and baroclinic energy conversions, and reach maximum amplitude in West Africa near 700 hPa at about 11°N (Skinner and Diffenbaugh, 2014). The northern-AEWs grow primarily through baroclinic interactions between the negative meridional PV gradient in the AEJ core and the positive low-level potential temperature (θ) gradient to the north of the AEJ (Thorncroft and Hoskins, 1994a; Pytharoulis and Thorncroft, 1999), and reach their maximum amplitude near 850 hPa at $\sim 20^\circ\text{N}$ (Thorncroft, 1995).

The goal of this study is to examine and understand the topographic influence on the AEJ and AEWs, as well as the convective systems that initiate the waves and interact with them as they propagate downstream. Understanding the processes and interactions between these features is essential to better predict rainfall activity during the rainy season and provide insight on the effects that a changing climate might have on rainfall activity and distribution across tropical North Africa.

The association of AEWs with convective triggering in East Africa and both systems increasing in intensity to the west, is consistent with case-studies of Berry and Thorncroft (2005); Lin et al. (2005) and idealized modelling work by Hall et al. (2006). MCSs move with and through the synoptic-scale AEWs and may act as potential vorticity sources for the large-scale circulation and contribute to tropical cyclongenesis (Laing et al., 2008; Cifelli et al., 2010). Some tropical cyclones, such as TS Alberto (2000), begin as AEW-MCS systems that initiate near the upstream topography and undergo cycles of decay and regeneration while propagating westward (Lin et al., 2005; Laing et al., 2008). Climate and synoptic-scale simulations by Hsieh and Cook (2005) suggest that the convection associated with the ICTZ is of more importance than the AEJ as a cause of AEW activity. Thorncroft et al. (2008) showed that AEWs are initiated by local convective forcing near the entrance region of the AEJ and the resultant latent heating creates the initial downstream trough that takes 5-7 days to reach the West African coast. Thorncroft et al. (2008) used a fixed jet and varied the position of the convective trigger and found that the right jet entrance was most effective for generating AEWs. However, the northern flank of the jet moves very little, therefore the standard

position for a convective trigger over the Darfur Mountains is nearly always optimal (Leroux and Hall, 2009). Leroux and Hall (2009) used a geographically fixed convective trigger and a variable jet to show that other factors such as the jet strength, its strength in its southern and western extensions and vertical shear are important independently of the location of the convective trigger. Using a three-member 22-yr ensemble of simulations, Wu et al. (2009) show that flattened topography causes the AEJ to disappear, essentially merging with the easterly flow associated with the ITCZ, and weakens the monsoonal flow. The absence of topography in northern Africa eliminated any effect induced by the southward sloping terrain over the Sahel and by the Ethiopian Highlands. Increases in surface temperature due to lower elevation and no topographic uplift lead to reductions in precipitation and latent heat flux across the Sahel and eastern Africa. This results emphasize the likely importance of topography in creating meridional surface temperature gradients (Wu et al., 2009).

Energetics analyses for AEWs have been used in various studies to reveal the processes that lead to the formation of these waves (Rennick, 1976; Estoque and Lin, 1977; Norquist et al., 1977; Thorncroft and Hoskins, 1994a,b; Diedhiou et al., 2002; Hsieh and Cook, 2007). Previous energetics analyses using observational data (Norquist et al., 1977) and modern reanalyses (Diedhiou et al., 2002) were not able to include realistic diabatic heating, boundary fluxes, and frictional dissipation. Norquist et al. (1977) used data from Phase III of the Global Atmospheric Research Program (GARP) Atlantic Tropical Experiment (GATE) and found that baroclinic conversions are stronger than barotropic conversions over land and the reverse over the ocean. Diedhiou et al. (2002) used 1979-97 National Centers for Environmental Prediction-National Center for Atmospheric Research (NCEP-NCAR) reanalyses and their energetics analyses suggested that 3-5 day easterly waves over land south of the AEJ grow from barotropic instability of the jet, and the waves north of the jet grow from both baroclinic and barotropic conversions below the jet level. Numerical studies (Rennick, 1976; Estoque and Lin, 1977; Thorncroft and Hoskins, 1994a,b) did not include longitudinal variations in a realistic background state. The simplified models with prescribed basic state of the AEJ tend to find that barotropic energy conversions are the main energy source of AEWs (Thorncroft and Hoskins, 1994a,b), while the models with prescribed cumulus convective heating of ITCZ usually find that diabatic heating is the major energy source for the waves

(e.g., Estoque and Lin, 1977). Hsieh and Cook (2007) used a regional climate model with convection parameterized to explore the energetics of AEWs. They found that baroclinic overturning is the dominant energy source, however barotropic energy conversions can be almost equally important when there is concentrated moist convection or shallow cumulus convection below the jet. The formation of AEWs in their model is usually associated with the occurrence of intense rainfall events over Africa, and is usually a result of nearly in-phase baroclinic and barotropic energy conversions.

Motivated by these studies that suggest the importance of both convective triggers and the East African topography in AEW formation, we conduct a sensitivity study of the forcing of the AEJ and generation of AEWs, modulated by the two-way interaction between AEWs and West African MCSs. Weather Research and Forecasting (WRF) model simulations are developed for realistic topography and for two sensitivity simulations: one with the height of topography reduced by 50% and the other with no topography across Africa (described in Section 4.2). For both cases, only the African topography is altered. We examine the impacts of topographical influences on the regional circulation (Section 4.3) and convective systems (Section 4). We also conduct an energetics analysis to evaluate the AEW sensitivity to topography in Section 4.4 and summarize the results in Section 4.5.

3.2 Numerical Model Configuration and Design of Sensitivity Runs

To determine how topography influences the evolution of AEWs, and the related initiation and development of MCSs over West Africa, the newer WRF model version 3.7.1 with WRF Preprocessing System (WPS) version 3.7.1 (Skamarock et al., 2008) was used to simulate three scenarios: realistic topography (hereafter called TOPO), topographic height smoothly reduced by 50% (HALF), and no topography (FLAT). The model is initialized at 0000 UTC 25 August and ran to 0000 UTC 30 September, a total of thirty-six days of simulation time, to observe how AEW activity changes in the different scenarios. We modeled this specific period in order to comparison to observations made during the National Aeronautics and Space Administration (NASA) African Monsoon Multidisciplinary Analyses

(NAMMA).

The three one-way nested domains have the same resolution and cover the same spacial area as discussed in Section 2.2 (Fig. 2.1). All three model domains use the Dudhia shortwave radiation scheme (Dudhia, 1989), the Rapid Radiative Transfer Model (RRTM) longwave radiation scheme (Mlawer et al., 1997), the WRF Single Moment 6-class (WSM6) microphysics scheme (Hong and Lim, 2006), the Noah land surface scheme (Chen and Dudhia, 2001), and the Yonsei University (YSU) ABL scheme (Hong et al., 2006) with the Revised Monin-Obukhov surface layer scheme (Jiménez et al., 2012). The Grell-Freitas convective parameterization (Grell and Freitas, 2013) is employed in the first and second domains (36 and 12 km) with the shallow convection option turned on. The convective parameterization is turned off in the inner domain.

Similarly to the shorter WRF runs discussed in Chapter 2, European Centre for Medium-Range Weather Forecasting (ECMWF) Reanalyses (ERA) Interim data are used to prescribe the WRF initial and boundary conditions. The statistics and analyses of these simulations exclude the first 12 hours of each simulation to account for model convection spinup.

3.3 African Easterly Wave Sensitivity to Large-Scale Topography

The realistic topography (TOPO) simulation produces a large-scale easterly jet with a mean zonal wind speed (u) of 10 m s^{-1} between 10°N and 20°N that is weaker by 2 m s^{-1} than the mid-level easterly jet observed from the ERA-Interim data (Fig. 3.1a and b). The westerly monsoon does not advance as far inland in the TOPO simulation compared to the reanalyses, while the low-level easterly winds coming from the Sahara Desert are stronger in TOPO compared to the reanalyses (Fig. 3.1c and d).

The reduction in African topography in the HALF and FLAT runs leads to a weakening of the θ gradients in the low troposphere across northern tropical Africa (Fig. 3.2b and e, c and f). The AEJ is a geostrophic response to the low-level temperature gradient; therefore the presence of a weaker AEJ coincides with the weak low-level θ gradient in both reduced topography runs, with the weakest AEJ

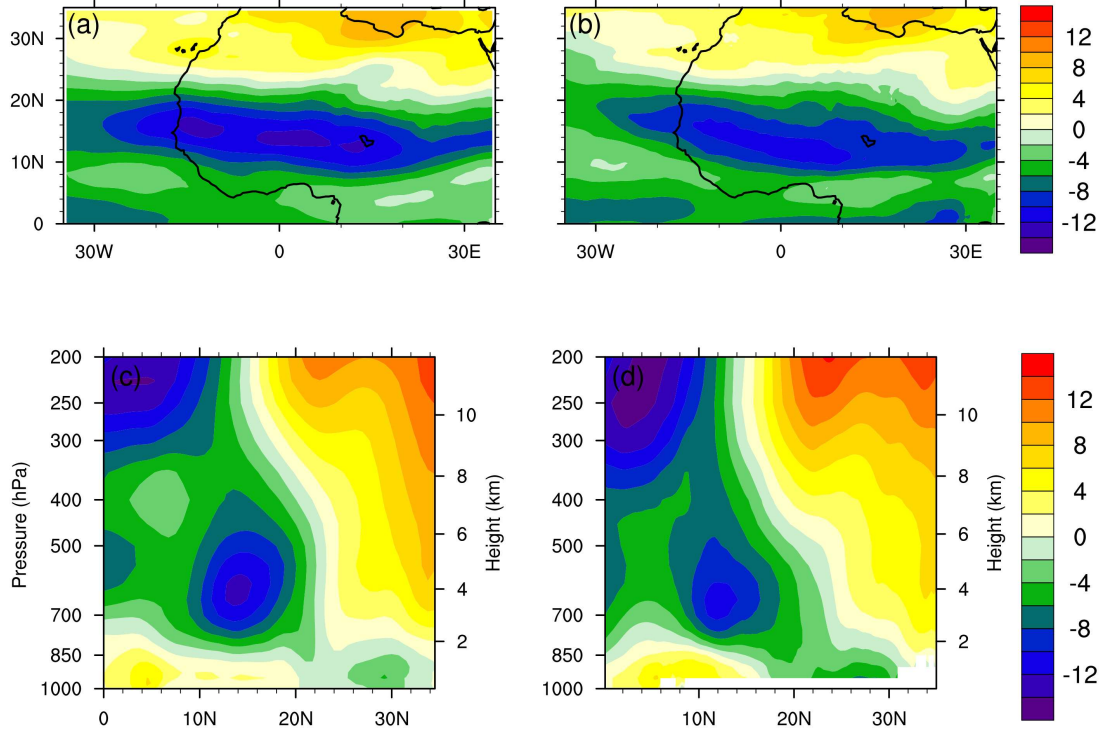


Figure 3.1. The mean zonal wind speed at 650 hPa (m s^{-1}) from (a) ERA-Interim and (b) domain 1 in TOPO, and vertical cross section of mean zonal wind speed (m s^{-1}) from (c) ERA-Interim and (d) domain 1 in TOPO at 0° longitude averaged over 25 August to 30 September 2006.

and θ gradient in the FLAT simulation (Figs. 3.2c and f). The low-level θ gradient, in combination with the mid-tropospheric PV gradient across northern tropical Africa, contribute to conditions for mixed barotropic-baroclinic instability along the AEJ. The weakening of the low-level θ gradient is thus expected to affect the baroclinic processes that develop the northern-AEWs. This effect would be in addition to impacts on AEW initiation resulting from MCS triggering over East African topography.

The alterations in the topography on the African continent not only affects the regional circulation but also how and where MCSs are spawned in the region. Based on previous studies (e.g., Berry and Thorncroft, 2005; Lin et al., 2005; Laing et al., 2008) changes in the topography in East Africa are expected to affect the genesis of AEWs through the frequency and location of MCS initiation there.

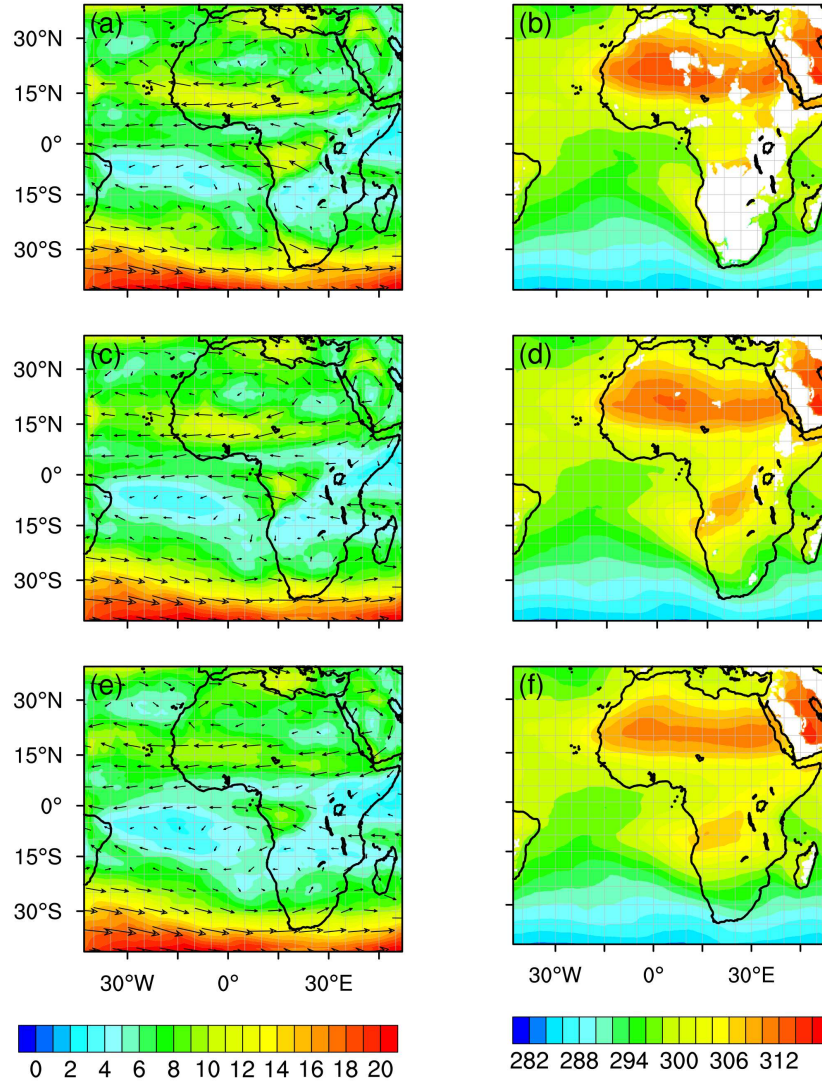


Figure 3.2. (*left*) Simulated mean total winds (shaded and vector) at 650 hPa in domain 1 in (a) TOPO, (c) HALF and (e) FLAT and (*right*) the mean potential temperature at 925 hPa in domain 1 in (b) TOPO, (d) HALF and (f) FLAT averaged over the 35.5-day analysis period.

3.3.1 Computation of African Easterly Wave Energetics

To understand the processes for the generation of AEWs in the different sensitivity runs, computations of the 3-5 day wave energetics are carried out in the region from (5° to 25°N, 10°W to 20°E) over Africa (see Fig. 2.1), similar to Hsieh and Cook (2007). AEWs usually form near 20°E, and attain their maximum intensity between 10°E and the west coast (Carlson, 1969b; Albignat and Reed, 1980), extending well into our specified region. To examine whether the mechanism that initiates AEWs in East Africa is different from that over our analysis domain covering West Africa. We perform similar wave energetics analyses over a smaller region between 5° and 20°N and 15° and 30°E (Fig. 2.1), the origin of AEWs as noted by (Burpee, 1972). The governing equations for eddy kinetic and available potential energy in an open system are

$$\frac{\partial K_E}{\partial t} = C_k + C_{pk} - D_E + K_{EB} + \Phi_{EB} \quad (3.1)$$

and

$$\frac{\partial A_E}{\partial t} = C_A - C_{pk} + G_E + A_{EB}. \quad (3.2)$$

The mathematical expressions and the definition of the variables in Eqns. (1) and (2) are listed in Table 1. K_E is the average eddy kinetic energy in one of the specified domains (white boxes in Fig. 2.1). The barotropic energy conversion, C_k , represents the sum of four barotropic conversion terms (C_{k1} , C_{k2} , C_{k3} and C_{k4}) [see Table 3.1]. C_{pk} is the baroclinic energy conversion [see Table 3.1]. The conversion of zonal available potential energy (A_Z) to eddy available potential energy (A_E) due to eddy heat flux along the zonal mean temperature gradient is represented by C_A [see Table 3.1]. The variables in Eqns. (1) and (2) that are not discussed further here are as follows: G_E is the generation of eddy available potential energy by diabatic heating, D_E is frictional dissipation, and Φ_{EB} denotes boundary pressure work done by eddies. The variables, K_{EB} and A_{EB} represent boundary fluxes of eddy kinetic and available potential energy, respectively.

The variables are interpolated from sigma surfaces to 41 pressure levels ranging from 1000 hPa to 125 hPa. The zonal and meridional averages are calculated on pressure surfaces and then vertically integrated between $P_1 = 125$ hPa and $P_2 = P_S$, the surface pressure. To isolate the 3-5-day wave activity, the perturbation

terms (u' , v' , ω' , and T') are filtered with a 3-5-day bandpass filter. The filtering is conducted by continuous wavelet transform using the complex Morlet wavelet (Torrence and Compo, 1998). Vertical integration uses the trapezoidal rule for the pressure levels from the surface to 125 hPa. Those points with topography start to contribute to the zonal and meridional averages when the pressure levels are above the topography height. The vertical integral from the surface to 125 hPa expresses the total amount of energy of AEWs and the AEJ in the defined three dimensional limited volume.

3.4 African Easterly Wave and Convective Interactions

During the summertime West African Monsoon (WAM) most of the rainfall occurs north of the Equator with maxima in rainfall accumulation occurring over the Atlantic Ocean (Fig. 3.3). The modeled rainfall maximum south of the Equator is associated with the rainforest in Central Africa (Fig. 3.3). The model simulates the offshore rainfall maximum located off the West African coast (Fig. 3.3a), which weakens gradually as the topography is altered (Fig. 3.3b and c). This suggests that the climatological offshore rainfall maximum is linked to topography. A narrow band of high rainfall accumulation across Central and West Africa between 5° and 13°N reflects strong ITCZ convection (Fig. 3.3a). The rainfall accumulation within that band reduces in HALF and FLAT indicating the lack of deep convection generated within the ITCZ (Fig. 3.3b and c). A significant amount of rainfall associated with the high terrain occurs between 30° and 45°E (Fig. 3.3a). The removal of topography eliminates the local topographically-forced rainfall maximum but allows the rainfall band to extend towards the east coast of Africa (Fig. 3.3b and c). In FLAT, however, a rainfall maximum develops over the southern end of the Red Sea as a result of the unhindered southwesterly flow interacting with the high terrain on the west coast of Saudi Arabia and Yemen (Fig. 3.3c).

To demonstrate the association between wave activity and moist convection over Africa in these simulations, Hovmöller diagrams of the meridional wind and the average simulated rainfall between 9° and 15°N are created (Fig. 3.4). The meridional average of precipitation between 9° and 15°N is calculated to capture the

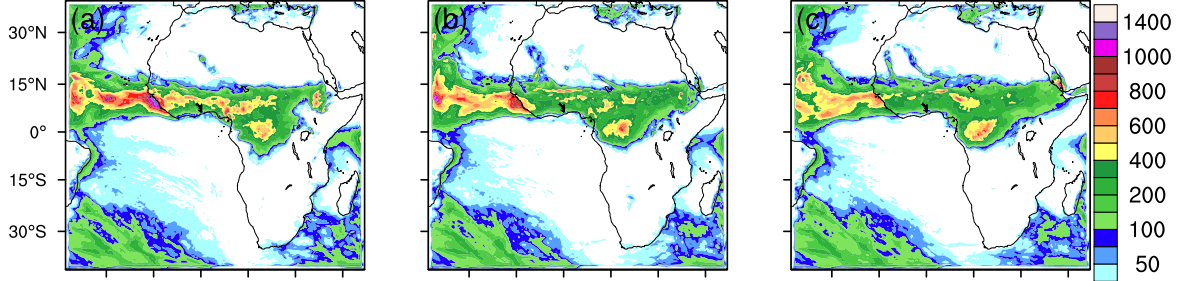


Figure 3.3. Rainfall accumulation (mm) over the 35.5-day analysis period in Domain 1 in (a) TOPO, (b) HALF and (c) FLAT.

average intensity of the Inter-Tropical Convergence Zone (ITCZ) convection over the region near the AEJ. AEWs are identified as reversals (northerly to southerly) of the meridional wind direction; the dashed lines in Figs. 3.4a and 3.4b highlight two examples of the collocation of wave troughs and precipitation maxima. Indeed, precipitation between 9° and 15°N intensifies when moving westward, consistent with enhanced precipitation coinciding with the wave trough (Fig. 3.4b). In all three simulations, intense rainfall events occur with active waves indicating that this close association between intense ITCZ convection and AEWs is sustained regardless of topography (Fig. 3.4). However, the occurrence of strong AEWs decreases significantly in the FLAT simulation compared to TOPO and HALF, which corresponds to reduced intense rainfall events (Fig. 3.4f).

Many of the modeled AEWs are generated east of 30°E , outside of the preferred source origin between 15° and 30°E established in Burpee (1972) (Figs. 3.4a, c and e). Intense isolated rainfall events occur frequently between 30° and 45°E , near the Ethiopian Highlands, in the TOPO simulation (Fig. 3.4b, Fig. 2.1, label E). These topographically triggered rainfall events are progressively less frequent in the HALF and FLAT simulations (Fig. 3.4d and f). If these rainfall events help to trigger AEWs, their reduced occurrence in the reduced topography cases may also explain the presence of weaker waves in the FLAT simulation.

An energetics analysis is performed to understand the processes for the generation of African waves in association with heavy rainfall events for East and West Africa. The time series of C_{k1} , C_{k2} , and C_{pk} averaged over the box representing East Africa (5° and 20°N , 15° and 30°E) show that baroclinic energy conversion, C_{pk} , is the dominant energy source for the AEWs (Fig. 3.5a, c and e). Intense

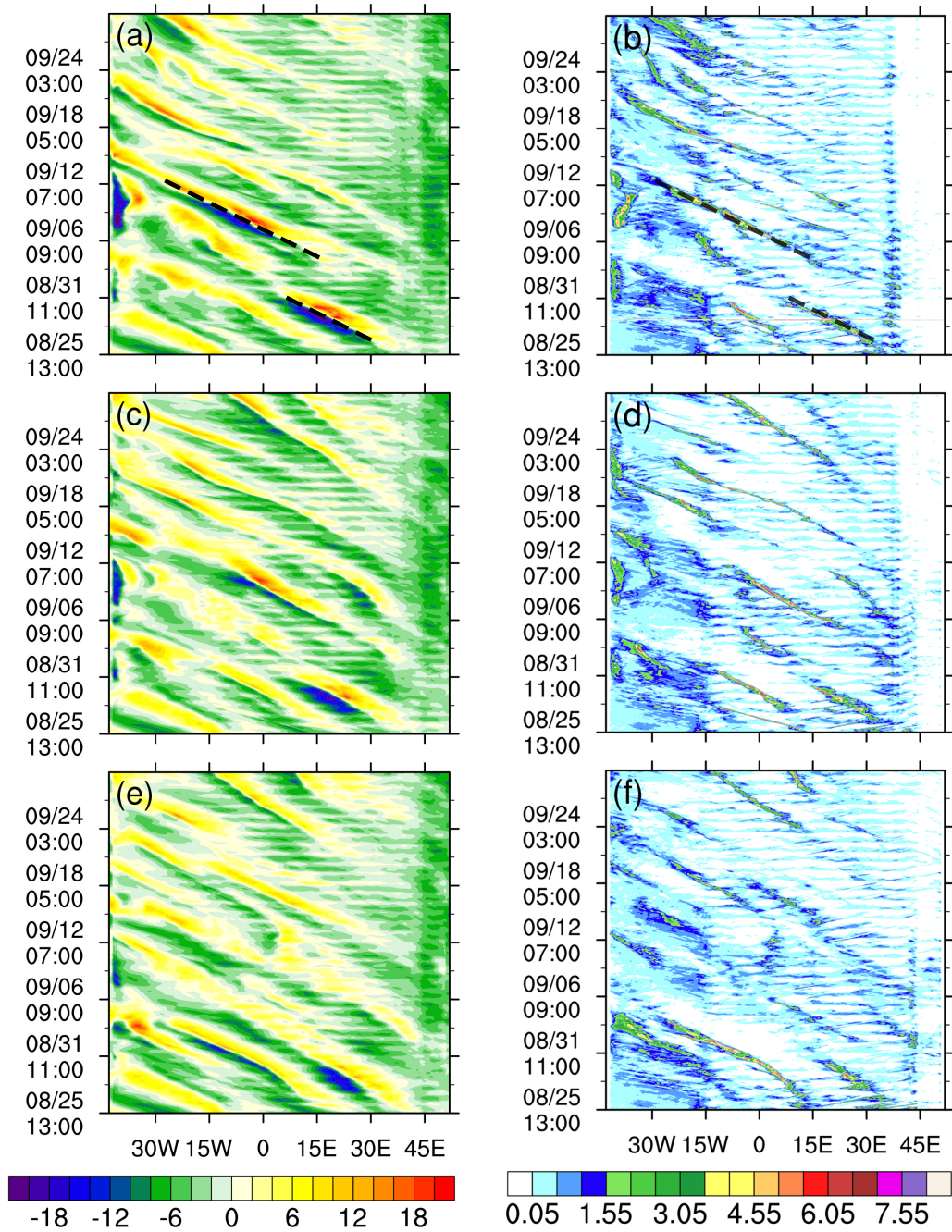


Figure 3.4. Hovmöller diagrams of 700 hPa meridional winds (m s^{-1}) and precipitation (mm hr^{-1}) averaged between 9° and 15°N for (a and b) TOPO, (c and d) HALF, and (e and f) FLAT. The dashed lines highlight the estimated location of the wave trough.

rainfall events (deep, moist convective systems) precede or coincide with significant spikes in C_{pk} (Fig. 3.5a, c and e) and K_E (Fig. 3.5b, d and f), highlighting the connection between convection and wave generation. Also, when ITCZ convection weakens the waves decay rapidly (Fig. 3.5d-f). Generally, C_{k2} is larger than C_{k1} in this region, which suggests the importance of strong shallow cumulus convection and the lack of deep convection for the initiation of AEWs over East Africa, in agreement with findings of Hsieh and Cook (2007).

Similar to East Africa, the time series of ITCZ convection and wave activity in West Africa show a connection between heavy rainfall events and wave growth (Fig. 3.6). Baroclinic processes still remain the dominant source of energy, and when C_{pk} is gradually increasing it is generally associated with increasing rainfall (Fig. 3.6a, c and e).

In the TOPO simulation, C_{k1} over West Africa increases compared to its value in East Africa indicating increase in cyclonic shear on the southern side of the jet in this region. The presence of deep convection on the southern side of the jet increases cyclonic shear due to the eddy forcing associated with the convection. The increase in C_{k1} also enhances and organizes convection south of the jet, which helps to maintain the waves as they propagate downstream. The dominance of C_{k1} over C_{k2} in the TOPO simulation suggests the importance of deep convection in maintaining the AEWs in West Africa. However, C_{k1} decreases in the FLAT simulation Fig. 3.6f), even producing negative contributions, which suggest that energy is being extracted from the eddies to strengthen the zonal flow (i.e., the weaker jet). The negative C_{k1} contributes to the overall lack of organized deep convection in the FLAT simulation, hinting at why the AEWs are not intensifying as they propagate downstream.

3.4.1 Energy conversions in West Africa

The mean meridional distribution of u in Figures 3.7a-c shows a gradual weakening and narrowing of the AEJ and a small intensification of the westerly monsoon flow near the surface from TOPO to FLAT simulations. The AEJ core shifts northward from 12°N (TOPO; Fig. 3.7a) to about 16°N (Figs. 3.7b,c). These changes in the mean flow, especially in the AEJ, can affect how the AEWs are energized as they propagate along the jet. The mean K_E distribution averaged

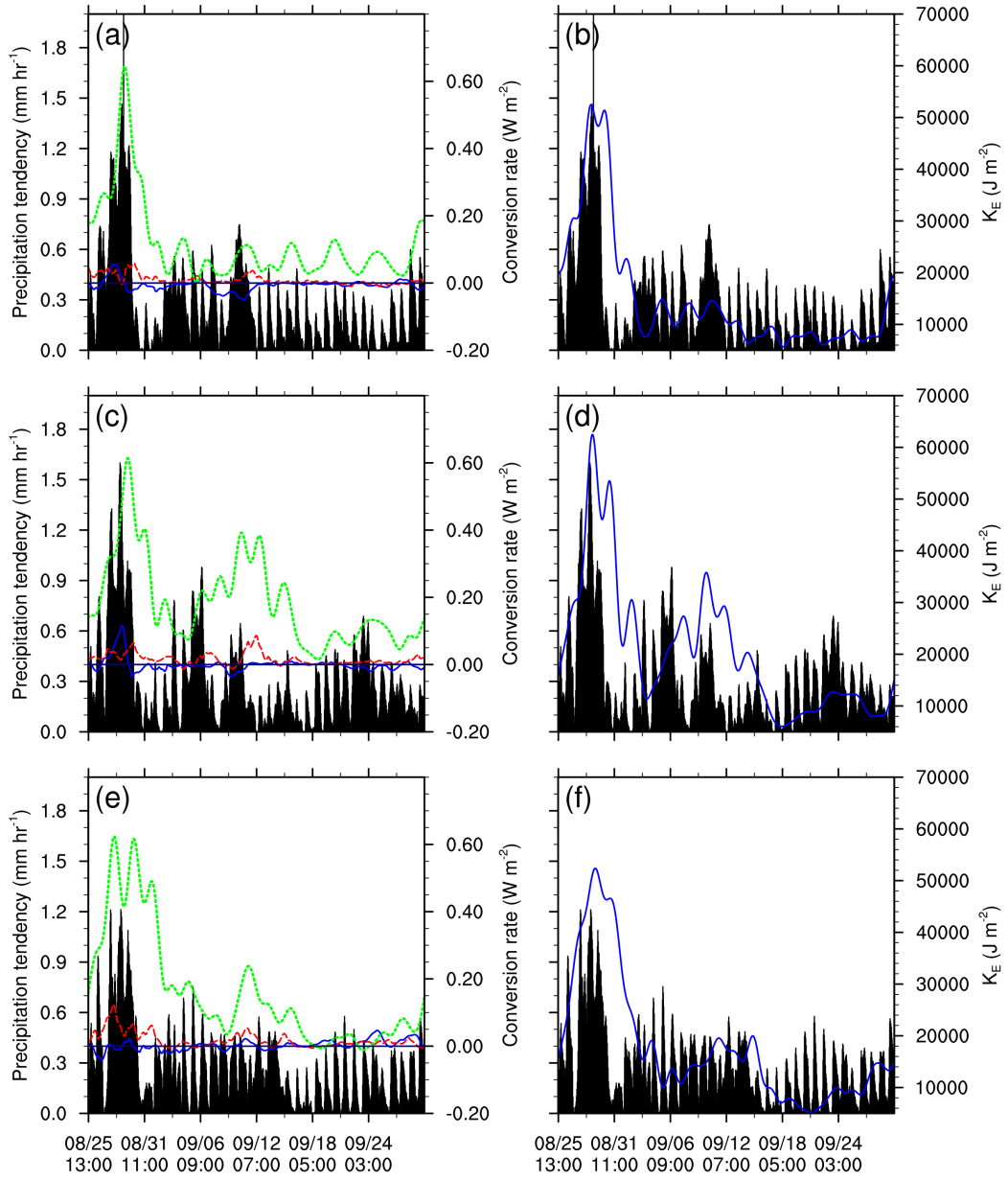


Figure 3.5. Time series of zonal mean precipitation (mm hr⁻¹) over East Africa (15° to 30°E averaged between 9° and 15°N) overlain with the time series of (*left*) zonal mean C_{k1} (blue line), C_{k2} (red line), C_{pk} (green line), and (*right*) K_E from 15° to 30°E averaged between 5° and 20°N for (a and b) TOPO, (c and d) HALF, and (e and f) FLAT

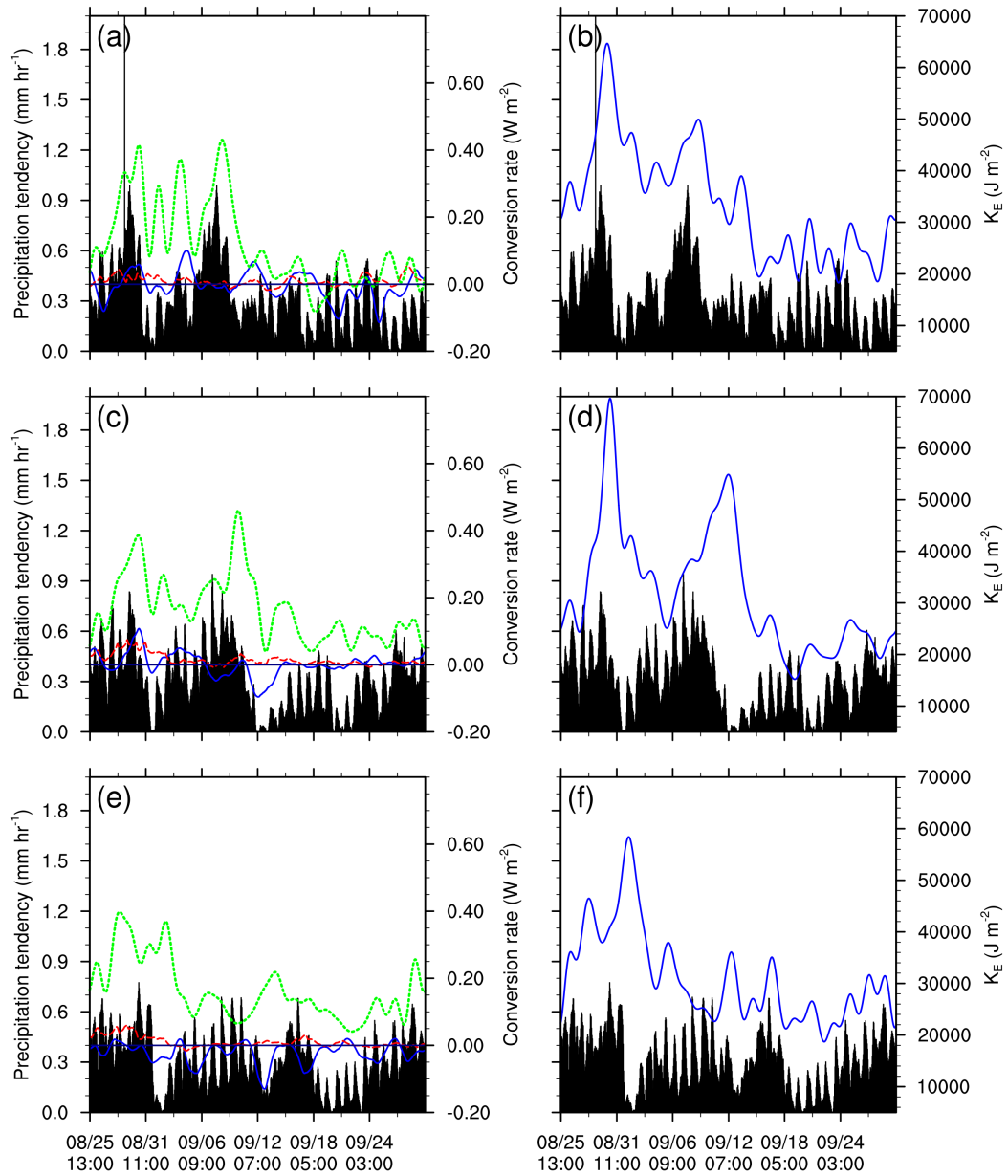


Figure 3.6. Time series of zonal mean precipitation (mm hr^{-1}) over West Africa (10°W to 20°E) averaged between 9° and 15°N) overlain with the time series of (*left*) zonal mean C_{k1} (blue line), C_{k2} (red line), C_{pk} (green line), and (*right*) K_E from 10°W to 20°E averaged between 5° and 25°N for (a and b) TOPO, (c and d) HALF, and (e and f) FLAT

between 10°W and 20°E depicts the two main track of AEWs, in agreement with Pytharoulis and Thorncroft (1999) (Figs. 3.7d-f). The modeled AEW activity near 700 hPa and south of the jet results mainly from barotropic energy conversion. At lower levels north of the jet AEW activity results mainly from the temperature gradient and baroclinic instability. There is also a significant amount of K_E near 200 hPa, consistent with the secondary zonal wind maxima at that level; the subtropical westerly jet (STJ) at 25 °N and the tropical easterly jet (TEJ) near the Equator. The mean K_E distribution weakens progressively from the TOPO to FLAT simulations, indicating the generation of weaker waves in the flattened topography environment (Fig. 3.7d-f).

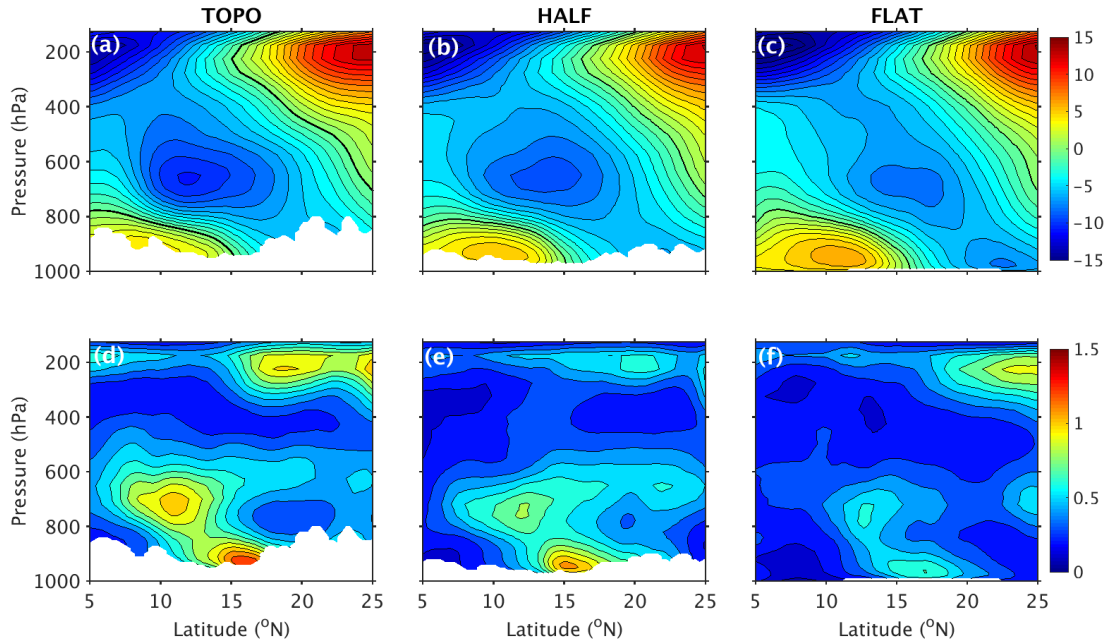


Figure 3.7. Mean meridional distribution of (*top*) u and (*bottom*) $([u'^2 + v'^2]/2g)$ averaged over the West Africa region for (a and d) TOPO, (b and e) HALF, and (c and f) FLAT. Contour intervals are 1 m s^{-1} in (a)-(c) and 0.1 m in (d)-(f). The bold contour marks the zero line.

The spatial distribution of the energy sources offers insight into how the energy conversions occur to energize the waves. Figures 3.8a-f display the vertical and meridional distribution of the two major terms of the barotropic conversions, C_{k1} and C_{k2} , for the three simulations. In the TOPO simulation, large values of C_{k1} are on the southern flank of the jet located at 9°N between 600 and 800 hPa. Weaker values of C_{k1} are between 600 and 700 hPa on the northern side of the jet. This may

be caused by a strong dry convection at low levels from the Sahara or the formation of squall lines north of the jet Hsieh and Cook (2007). The downgradient ($\partial[u]/\partial y$) eddy momentum flux ($[u'v']$) converts zonal kinetic energy into eddy kinetic energy in the mid-troposphere. Two other regions of production of K_E by C_{k1} appear near the surface at 20°N and the tropopause (Figs. 3.8a-c). Large values of C_{k1} near the tropopause are associated with the anticyclonic divergent flow of the ITCZ and the large horizontal shear of the TEJ. The presence of C_{k1} near the surface is associated with the surface confluent zone between 15° and 20°N . C_{k1} on the southern flank of the jet along and at low-levels north of the jet weaken in the HALF run and even moreso in the FLAT run (Figs. 3.8b,c). Areas where K_E is converted to A_E by C_{k1} show up in the simulations between 11° and 15°N in the low- to mid-troposphere, corresponding to the region of negative $[u'v']$ just behind the surface confluent zone (Figs. 3.8a-c). This negative conversion of C_{k1} below the jet indicates that the horizontal eddy momentum flux is consumed to strengthen the zonal flow.

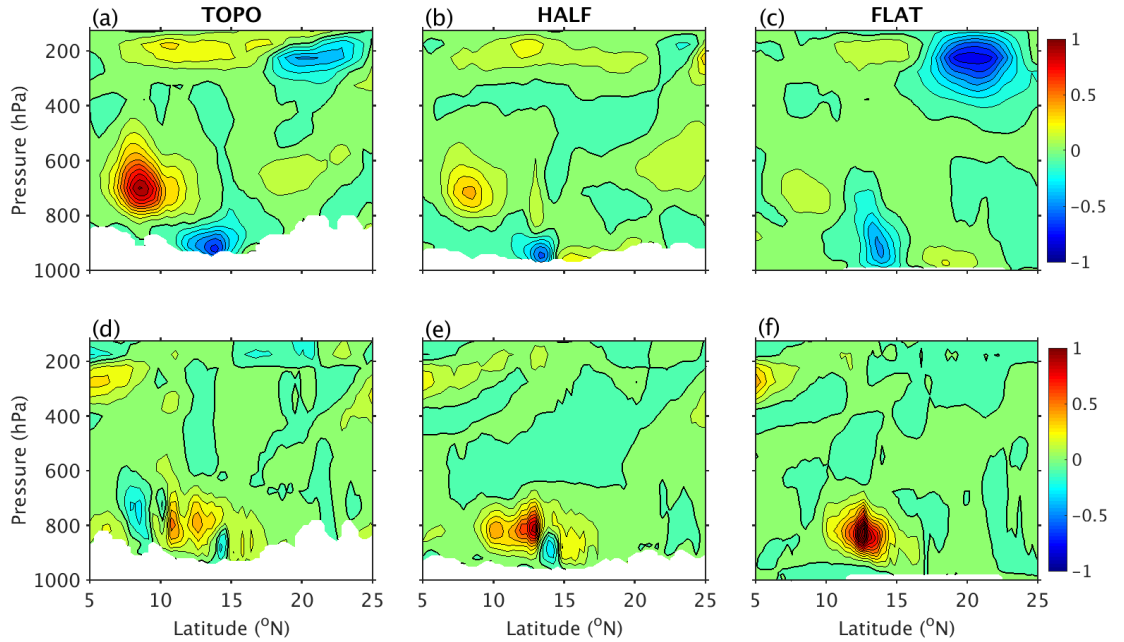


Figure 3.8. Mean meridional distribution of (top) $-\frac{[u'v']}{g} \frac{\partial[u]}{\partial y}$ and (bottom) $-\frac{[u'\omega']}{g} \frac{\partial[u]}{\partial p}$ averaged over the West Africa region for (a and d) TOPO, (b and e) HALF, and (c and f) FLAT. Contour intervals are $0.1 \times 10^{-5} \text{ m s}^{-1}$. The bold contour marks the zero line.

The distribution of C_{k2} is mostly confined below 700 hPa where there are large

vertical shears below the jet (Fig. 3.8d-f). Positive values of C_{k2} are a result of the downward transport of easterly momentum ($[u'\omega'] < 0$), interacting with the vertical shear ($\partial[u]/\partial p$). The presence of strong shallow cumulus convection beneath the jet in the Tropics over Africa can make C_{k2} more important than C_{k1} , and can initiate and maintain AEWs (Hsieh and Cook, 2007). In the FLAT simulation, the maximum in C_{k2} below 700 hPa occurs between 10° and 15°N collocated with the vertical shear between the jet and the monsoon. Since the vertical shear beneath the jet weakens slightly in FLAT compared to TOPO, the presence of strong shallow cumulus convection must be contributing to the enhanced maximum in C_{k2} in this location compared to TOPO and HALF. The area of production of K_E by C_{k2} between 200 and 400 hPa is associated with the vertical shear beneath the TEJ interacting with the vertical eddy momentum flux in deep convection south of the AEJ (Fig. 3.8d-f).

Now exploring the production of A_E through C_A , which C_{pk} converts into K_E . The distribution of C_{A1} is mainly located in the lower troposphere centered near 15°N (Figs. 3.9a-c), at the surface confluent zone. Thermal advection associated with correlations between southward heat fluxes $[v'T']$ and large meridional temperature gradients converts A_Z into A_E . The removal of topography somewhat weakens and spreads out the production of A_E by C_{A1} in the FLAT simulation compared to the two other simulations (Fig. 3.9f). This reduction is expected due to the weaker low-level $\partial[T]^*/\partial y$ in the FLAT simulation. The energy conversion C_{A2} is a measure of the correlation between the vertical heat flux $[\omega'T']$ and the vertical gradient of zonal mean temperature deviations ($\partial[T]^*/\partial p$). The mean distribution of C_{A2} shows positive conversion of A_Z to A_E north of 15°N at low-levels, where $-\omega'T' > 0$ correlates with positive values of $\partial[T]^*/\partial p$. Lower values of C_{A2} between 200 and 300 hPa, where $-\omega'T' > 0$ in deep convection interacts with positive $\partial[T]^*/\partial p$ at these levels, which is associated with a more uniform condensational heating in clouds at these levels (Hsieh and Cook, 2007).

The distribution of C_{pk} averaged between 10°W and 20°E (Figs. 3.9g-i) show that large baroclinic overturning (positive C_{pk}) generates eddy kinetic energy (K_E) mostly in the upper troposphere on the southern flank of the jet. The energy conversion, C_{A2} is closely related to the baroclinic overturning of C_{pk} (see Table 3.1). The major production of K_E by C_{pk} between 600 and 200 hPa is a result of warm ascending or cool descending air ($[\omega'T'] < 0$) associated with latent heat

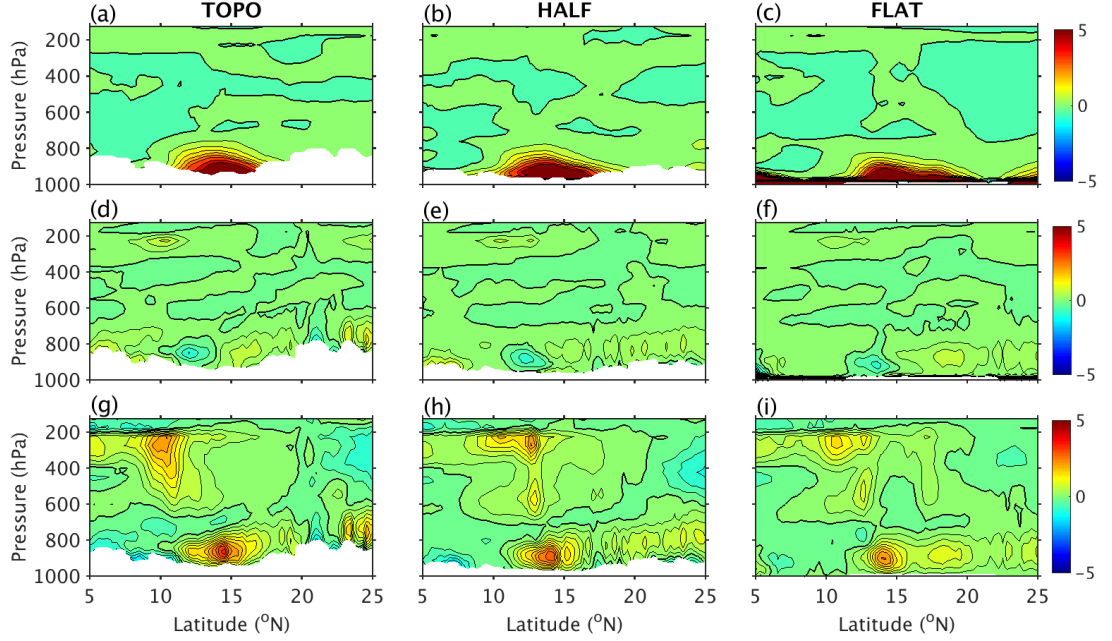


Figure 3.9. Mean meridional distribution of (top) $-([v'T']/\bar{\sigma})(\partial[T]/\partial y)$, (middle) $-([\omega'T']/\bar{\sigma})(\partial[T]^*/\partial p)$, and (bottom) $-(R/pg)[\omega'T']$ averaged over the West Africa region for (a, d and g) TOPO, (b, e and h) HALF, and (c, f, and i) FLAT. Contour intervals are $0.5 \times 10^{-5} \text{ m s}^{-1}$ in (a)-(c) and $0.3 \times 10^{-5} \text{ m s}^{-1}$ in (d)-(i). The bold contour marks the zero line.

release or evaporative cooling due to convection above the midtroposphere in the wave troughs or ridges. The production of K_E by C_{pk} in the low troposphere near 15°N is strongly correlated with the production of A_E by C_{A1} (Figs. 3.9a-c, g-i). The positive conversions of C_{pk} converts most of the A_E generated from C_{A1} into K_E directly. The positive C_{pk} below 800 hPa between 15° and 20°N is associated with dry convection in the Saharan heat low (Figs. 3.9g-i). The upper tropospheric baroclinic overturning in the FLAT simulation is weaker than the other two runs indicating a weakening in deep convection in that region (Figs. 3.9g-i). There is little change in the magnitude of C_{pk} generation in the lower troposphere, indicating no significant change in shallow convection (Figs. 3.9g-i).

The absence of topography leads to a decrease in K_E at low-levels north of the jet and at the jet level on the southern flank of the jet, which indicates weaker AEWs. The weak production of K_E by C_{pk} and C_{k1} at upper levels indicate that there is less presence of deep convection on the southern flank of the jet in the flattened topography environment, which greatly affects the generation of barotropic

instability due to horizontal shear. The increased production of C_{k2} beneath the jet suggests more presence of shallow convection.

3.4.2 Energy conversions in East Africa

The mean meridional distribution of u averaged between 15°E and 30°E in Figures 3.10a-c shows a 2 m s^{-1} decrease in the intensity of the AEJ and a gradual strengthening of the low-level westerly flow from the TOPO to FLAT simulations. The mean K_E distribution for East Africa indicates AEWs are active near 700 hPa south of the jet and at lower levels north of the jet (Figs. 3.10d-f). The mean K_E distribution suggests some weakening in wave intensity between the simulations with topography and with flattened topography.

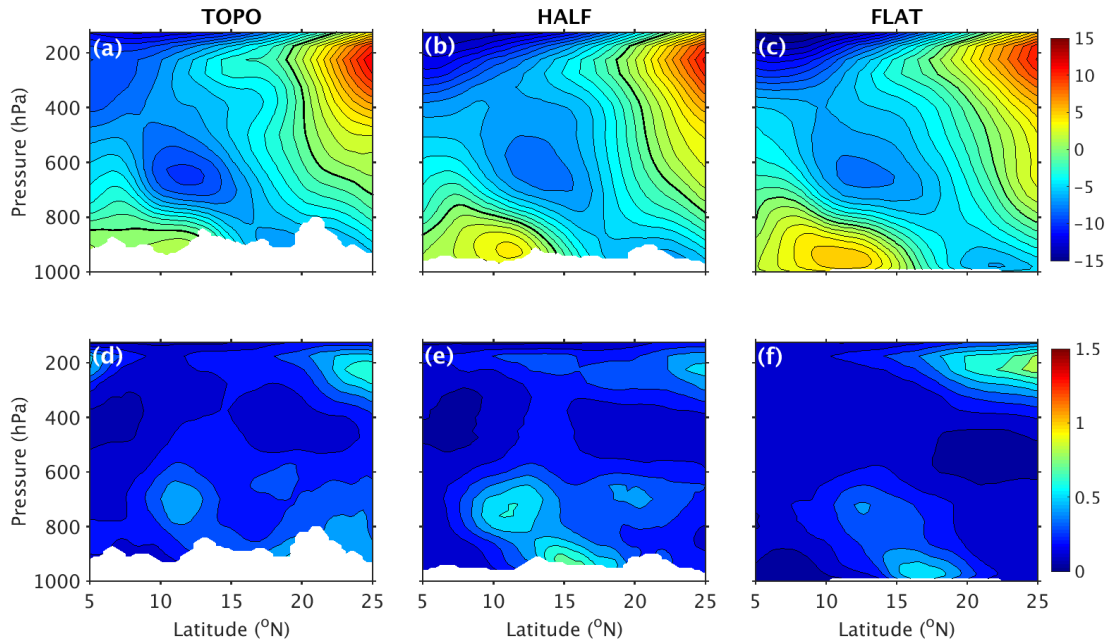


Figure 3.10. Mean meridional distribution of (*top*) u and (*bottom*) $[u'^2 + v'^2]/2g$ averaged over the East Africa region for (a and d) TOPO, (b and e) HALF, and (c and f) FLAT. Contour intervals are 1 m s^{-1} in (a)-(c) and 0.1 m in (d)-(f). The bold contour marks the zero line.

Figures 3.11a-c display the vertical and meridional distribution of C_{k1} for the three simulations. The maximum of C_{k1} distribution is located near 10°N between 600 and 800 hPa in the TOPO and HALF simulations (Figs. 3.11a-c). The production of K_E by C_{k1} on the southern flank of the jet weakens in the FLAT

simulation, indicative of a weaker jet and weaker horizontal shear of the jet (Fig. 3.11c). Similar to West Africa, the distribution of C_{k2} is primarily located below 600 hPa beneath the jet (Figs. 3.11d-f). The production of K_E by C_{k2} centered at 800 hPa changes very little between the three simulations (Figs. 3.11d-f); this is because the simultaneous weakening of the jet and strengthening of the monsoon cause little change in $\partial[u]/\partial p$ directly beneath the jet (Figs. 3.10a-c). However, a weaker jet means that downward transport of weaker easterly momentum occurs in shallow convection beneath the jet in the FLAT simulation.

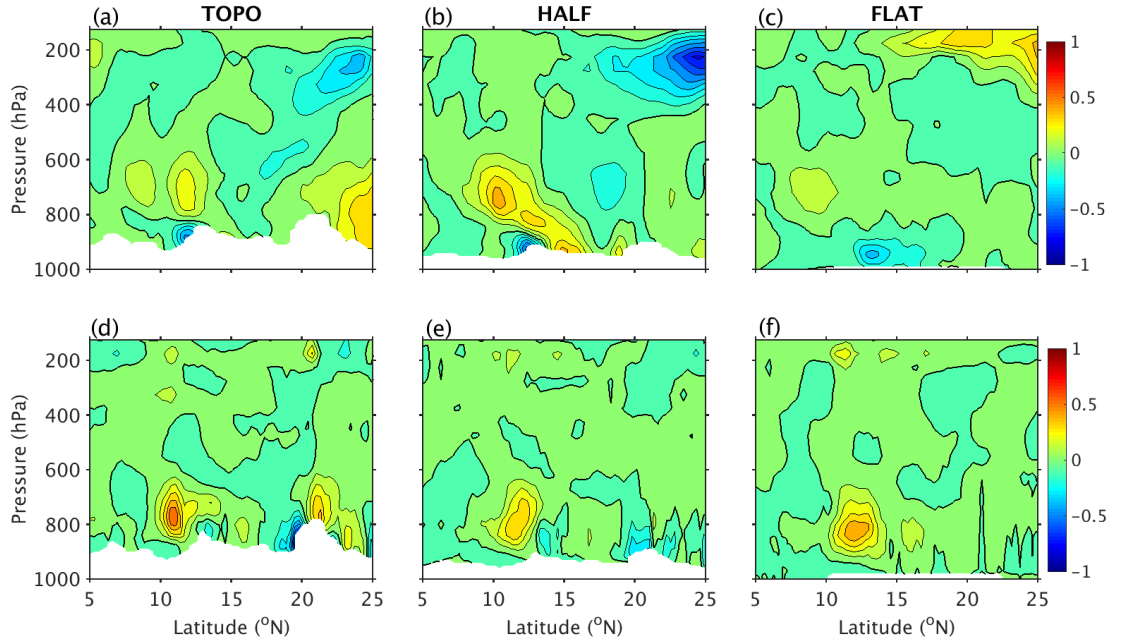


Figure 3.11. Mean meridional distribution of (*top*) $-([u'v']/g)(\partial[u]/\partial y)$ and (*bottom*) $-([u'\omega']/g)(\partial[u]/\partial p)$ averaged over the East Africa region for (a, d, and g) TOPO, (b, e, and h) HALF, and (c, f, and i) FLAT. Contour intervals are $0.1 \times 10^{-5} \text{ m s}^{-1}$. The bold contour marks the zero line.

Similar to West Africa, the distribution of C_{A1} is mainly located in the lower troposphere centered near 15°N , and weakens as the low-level meridional temperature gradient from TOPO to FLAT (Figs. 3.12a-c). The distribution of C_{A2} shows an area of positive conversion of A_Z to A_E below 800 hPa (Figs. 3.12d-f). Negative values of $[\omega'T']$ in the lower troposphere are due to ascent of warm, dry air from the north or descent of cool, moist air from the south, depending on the phase of the wave. The generation of A_E by C_{A2} in the lower troposphere between 15° and 20°N strengthens in the FLAT simulation.

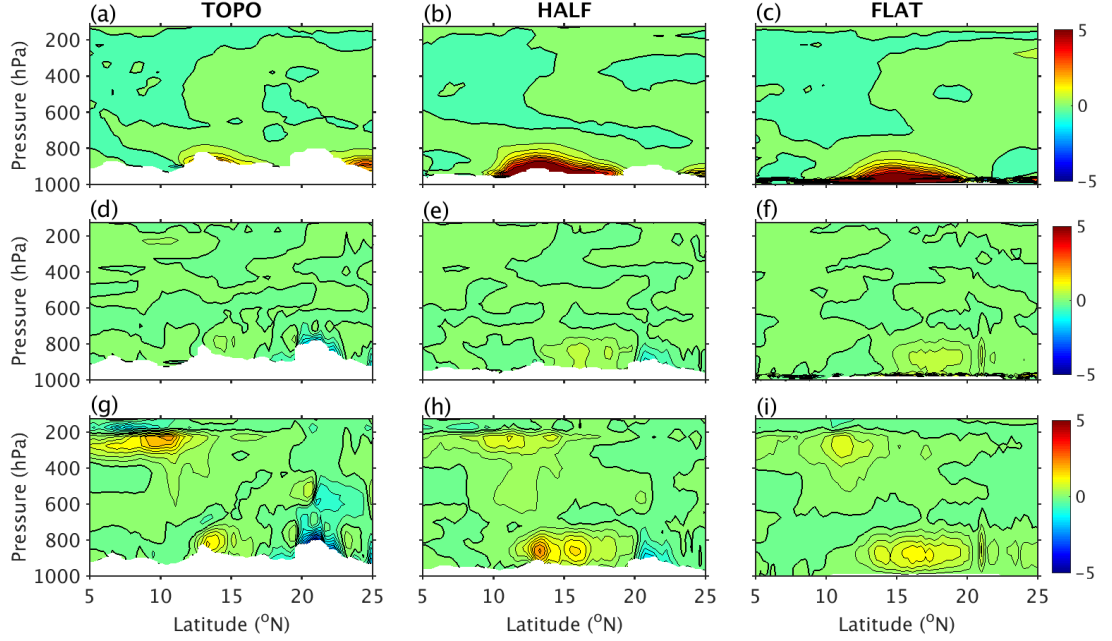


Figure 3.12. Mean meridional distribution of (*top*) $-([v'T']/\bar{\sigma})(\partial[T]/\partial y)$ and (*middle*) $-([\omega'T']/\bar{\sigma})(\partial[T]^*/\partial p)$, and (*bottom*) $-(R/pg)[\omega'T']$ averaged over the East Africa region for (a, d and g) TOPO, (b, e and h) HALF, and (c, f and i) FLAT. Contour intervals are $0.5 \times 10^{-5} \text{ m s}^{-1}$ in (a)-(c) and $0.3 \times 10^{-5} \text{ m s}^{-1}$ in (d)-(i). The bold contour marks the zero line.

Similar to West Africa, there is a generation of K_E by large baroclinic overturning in the upper troposphere on the southern flank of the jet (Figs. 3.12g-i). The magnitude of the positive C_{pk} is, however, weaker in East Africa than that observed in West Africa for each simulation. The difference in the magnitude of the major production of K_E by C_{pk} between East and West Africa shows the difficulty in growing an AEW from a small perturbation causing the energy conversions to be weaker earlier in the lifecycle of the AEW when its amplitude is smaller. Again, the upper tropospheric baroclinic overturning in the FLAT run is weaker than the other two runs (Figs. 3.12g-i). The generation of K_E by C_{pk} between 15° and 20°N is greater in FLAT than in TOPO, which corresponds with the increase in C_{A2} in that area (Figs. 3.12g-i). In this area, more dry convection in the hotter Sahara converts A_E into K_E in the FLAT simulation.

Over East Africa, barotropic instability is weaker than baroclinic overturning indicating that AEWs in East Africa in the model are not initiated by barotropic instability of the jet, which is in agreement with Hsieh and Cook (2007). Barotropic

instability associated with the vertical wind shear (C_{k2}) is greater than barotropic instability associated with the horizontal wind shear (C_{k1}) indicating the importance of shallow cumulus convection for the initiation of AEWs. The removal of topography allows the southwesterly monsoon flow to strengthen and advance further into tropical North Africa. The weakening in the low-level temperature gradient, however, reduces baroclinicity, which causes little to no change in low-level production of C_{pk} near 14°N (Figs. 3.12g-i).

3.5 Conclusions

The influence of topography on the development of the AEJ, AEWs and the resulting MCSs in West Africa is examined. WRF simulations are used to examine the sensitivity of these systems to variations in the topography over Africa; the control simulation (TOPO) agrees well with observations. The sensitivity simulations emphasized the importance of the African topography in creating meridional surface temperature gradients that produce the AEJ. The removal of topography weakens the low-level temperature gradient, especially between the Sahara and the Sahel. The weakening of the positive low-level temperature gradient leads to the weakening of the AEJ, whose existence results from thermal wind balance and the strong meridional low-level temperature gradient. AEWs grow at the expense of the AEJ; therefore, a weaker jet provides less zonal kinetic energy for conversion into eddy kinetic energy to maintain the waves.

The gradual increase in the intensity of the AEWs as they propagate towards the West African coast is consistent with wave development by baroclinic and barotropic processes. The mean distribution of eddy kinetic energy in East Africa indicates that weaker AEWs are initiated in the FLAT simulation compared to TOPO and HALF at both the jet level and near the surface. The barotropic conversion associated with the vertical wind shear is greater than that associated with the horizontal shear. This is due to strong shallow convection beneath the jet. Weak barotropic conversion associated with the horizontal wind shear at the jet level indicates that the AEWs are less likely growing by barotropic processes but rather by baroclinic overturning associated with deep convection on the southern flank of the jet. However, the lack of deep moist convection leads to weaker barotropic and baroclinic processes at the jet level in the FLAT simulation.

In West Africa, eddy kinetic energy increases significantly in TOPO and HALF cases compared to that in East Africa (with eddy kinetic energy in HALF weaker than that in TOPO) while there is little change in the magnitude of energy in the FLAT run between East and West Africa. This suggests that the presence of topography influences the growth of the waves as they propagate downstream. The lack of topography removes processes such as topographic uplift, PV generation through lee-side cyclogenesis and latent heating by topographically triggered MCS that would influence AEW and MCS downstream development.

As topography is altered the rainfall accumulation decreases over West Africa and the Atlantic Ocean indicating the lack of downstream development of AEWs and their MCSs. This suggest that the climatological offshore rainfall maximum is linked to topography and AEW activity. I investigate this further in the next chapter.

<i>Variable</i>	<i>Equation</i>	<i>Definition</i>
K_E	$\int_{p_1}^{p_2} \frac{[u'^2 + v'^2]}{2g} dp$	Eddy kinetic energy
A_E	$\int_{p_1}^{p_2} \frac{[T'^2]}{2\bar{\sigma}} dp$	Eddy available potential energy
C_k	$C_{k1} + C_{k2} + C_{k3} + C_{k4}$	Barotropic energy conversion of zonal kinetic energy to K_E through the zonal and meridional wind shears
C_{k1}	$-\int_{p_1}^{p_2} \overline{[u'v']} \frac{\partial [u]}{\partial y} \frac{dp}{g}$	Eddy momentum flux weighted by horizontal shear of the zonal wind
C_{k2}	$-\int_{p_1}^{p_2} \overline{[u'\omega']} \frac{\partial [u]}{\partial p} \frac{dp}{g}$	Eddy momentum flux weighted by vertical shear of the zonal wind
C_{k3}	$-\int_{p_1}^{p_2} \overline{[v'^2]} \frac{\partial [v]}{\partial y} \frac{dp}{g}$	Eddy momentum flux weighted by the horizontal shear of the meridional wind
C_{k4}	$-\int_{p_1}^{p_2} \overline{[v'\omega']} \frac{\partial [v]}{\partial p} \frac{dp}{g}$	Eddy momentum flux weighted by the vertical shear of the meridional wind
C_{pk}	$-\int_{p_1}^{p_2} \frac{R}{p} \overline{[\omega'T']} \frac{dp}{g}$	Baroclinic energy conversion of A_E to K_E through vertical overturning
C_A	$C_{A1} + C_{A2}$	Conversion of zonal available potential energy to A_E due to eddy heat flux along the zonal mean temperature gradient
C_{A1}	$-\int_{p_1}^{p_2} \frac{[v'T']}{\bar{\sigma}} \frac{\partial [T]}{\partial y} dp$	Zonal eddy heat flux weighted by the zonal mean temperature gradient
C_{A2}	$-\int_{p_1}^{p_2} \frac{[\omega'T']}{\bar{\sigma}} \frac{\partial [T]^*}{\partial p} dp$	Vertical eddy heat flux weighted by the vertical gradient of the zonal mean temperature deviation

Table 3.1. Mathematical expressions for the components in the energy equation. $[\]$ represents a zonal average while $\overline{[\]}$ represents a meridional average of the zonal mean; primes represent deviations from the zonal average, and asterisks represent deviations from the area mean on an isobaric surface. They are related by $() = [\] + ()'$ and $() = \overline{[\]} + ()^*$. Variable names follow the AMS Glossary of Meteorology.

Chapter 4 | Climatology of the West African Off-shore Rainfall Maximum and its relationship with topography

4.1 Introduction

Recent studies have revealed that there are distinct differences in the dynamic and thermodynamic characteristics of the MCS that propagate through West Africa and, in some cases, over the Atlantic Ocean (DeLonge et al., 2010; Jenkins et al., 2010; Guy et al., 2011). Continental systems are more symmetric and develop more rapidly than their marine counterparts. These precipitating storms also tend to be deep and intense convective systems over the continental regions of West Africa and as they travel towards the Atlantic Ocean they develop stratiform features (DeLonge et al., 2010; Xu and Zipser, 2012). Land and ocean regimes differ based on thermodynamics (i.e., CAPE and CIN), aerosol effects (CCN) or morphology of convective core (Xu and Zipser, 2012). Low-level convergence is usually required to initiate convective overturning over the oceans because only air near the surface has sufficiently high θ_e to become buoyant when it is forcibly raised. Convection over continental regions can be initiated without significant boundary layer convergence. Strong surface heating can produce positive parcel buoyancy all the way to the surface. Sustained deep convection, however, requires mean low-level moisture convergence.

Past studies showed that MCS are located preferentially at and ahead of the trough of African Easterly Waves (AEWs) in the southern part of the Sahel and at and behind the AEW trough in the northern Sahel (Mathon et al., 2002). Previous

studies have used satellite and radar in order to comprehend convection and rainfall in West Africa (Fuentes et al., 2008; Nicholls and Mohr, 2010; Guy and Rutledge, 2012; Guy et al., 2011). Guy and Rutledge (2012) partitioned the AEW into four phases: trough, northerly, ridge and southerly, and a fifth category when no AEW was present. They revealed that the northerly phase of the wave was characterized by reduced convective strength and larger stratiform fractions.

Thorncroft and Hodges (2001) suggest that the Guinea Highlands may be a region where the AEWs experience extra development, in association with latent heat release in deep moist convection and orographic processes. The growth region of AEWs located in the lee of the Guinea Highlands in Thorncroft and Hodges (2001) is collocated with the climatological maximum in rainfall. A similar rainfall maximum occurs in the lee of Mexico's Sierra Madre Mountains where another notable peak in AEW growth occurs (Thorncroft and Hodges, 2001). The interaction of easterly flow and easterly waves (which were AEWs) with the Sierra Madre Mountains is responsible for the favored location of AEW development and tropical cyclone initiation in the subtropical Eastern Pacific ocean (Mozer and Zehnder, 1996a,b; Zehnder, 1991; Zehnder and Gall, 1991; Zehnder et al., 1999). The interaction between easterly waves and topography results in the cyclonic vorticity maxima of waves increasing by 50% (Zehnder et al., 1999). While the combined interaction of the Intertropical Convergence Zone (ITCZ), AEWs, and topography results in the cyclonic vorticity maxima of the waves to increase by 100% in the lee of the topography (Zehnder et al., 1999). A similar interplay of topographic forcing, monsoon environment may explain the location of the climatological rainfall maximum in West Africa.

The maximum in rainfall is likely influenced by the elevated terrain in the West African region, and further enhanced by the land-sea contrasts. We examine the offshore rainfall maximum in West Africa using Tropical Rainfall Measuring Mission (TRMM) satellite data and the European Center for Medium-Range Weather Forecasts (ECMWF) Reanalyses (ERA)-Interim to create a sixteen-year climatology of rainfall. We employ the Weather Research and Forecast (WRF) model to perform simulations examining the sensitivity of the offshore rainfall maximum to upstream topography. Our objective is to understand why such a stable rainfall maximum is located just offshore of West Africa.

4.2 Data

Observations for May to October for the 16 years 1998-2013 are used to examine variations in the West African Monsoon (WAM) season and active periods of AEWs. This period spans the lifetime of the TRMM satellite.

4.2.1 TRMM Products

The Version 7 TRMM Multi-satellite Precipitation Analysis (TMPA) 3-hourly product, 3B42, is analyzed for this study. This dataset is developed using the 3B42 algorithm that begins with rainfall estimates from geostationary IR observations and adjusts these using an optimal combination of inputs from the TRMM and polar orbiting satellites. The final gridded precipitation rates [p (mm hr^{-1})] and precipitation-error estimates have a 3-hour temporal resolution and a $0.25^\circ \times 0.25^\circ$ spatial resolution in a global belt extending from 50°S to 50°N (Huffman et al., 2007). Precipitation less than 0.2 mm day^{-1} is referred to as a trace and is ignored in this study based on the World Meteorological Organization definition.

The Version 6 TRMM Precipitation radar (PR) Level 2 Rainfall Rate and Profile Product, 2A25, is also used in this study as it corrects the rain attenuation in measured radar reflectivity and estimates the instantaneous three-dimensional distribution of rain from the TRMM precipitation radar data (Kummerow et al., 1998). The spatial coverage is between 38°S and 38°N due to the inclination of the satellite. It provides extensive coverage with a vertical resolution of 250 m and a temporal resolution of 16 orbits per day.

4.2.2 Reanalysis data

Pressure level and surface data utilized in this study were acquired from ERA-Interim 6-hourly global atmospheric reanalysis. The spatial resolution of the data set is approximately 80 km (T255 spectral) on 60 vertical levels from the surface up to 0.1 hPa (Dee et al., 2011). We use variables such as zonal wind (u), meridional wind (v), vertical velocity (ω), specific humidity (q), and temperature (T) and derived quantities such as equivalent potential temperature (θ_e) and moisture divergence to analyze the atmospheric conditions in the study region. The ERA-Interim data

are also used as initial and boundary conditions in the WRF simulations described below.

4.3 Model Sensitivity Runs

I use the output from the WRF sensitivity runs developed from the WRF model version 3.7.1 with WRF Preprocessing System (WPS) version 3.7.1 (discussed in Chapter 3) to determine how topography influences the climatological offshore rainfall maximum in West Africa. I conduct the statistics and analyses of these simulations in D2 (Fig. 2.1) and exclude the first 12 hours of each simulation to account for model convection spinup.

4.4 Rainfall Climatology

The 3-hourly TRMM 3B42 rainfall estimates are averaged over May to October to study the rainfall activity during the West African Monsoon (WAM) months. During the WAM most of the rainfall occurs north of the Equator with maxima in rainfall accumulation occurring over the Atlantic Ocean (Fig. 4.1). The seasonal precipitation amount averaged over the sixteen years displays the area of high rainfall accumulation over the Atlantic Ocean. These high accumulations are linked to the ITCZ where WAM southwesterlies converge with the northeasterly Trade winds (Fig. 4.1a). A small region of very high rainfall accumulations of 2250–2750 mm occur within this zone just off the coast (Fig. 4.1a). To examine why this small area experiences such copious amount of rainfall we designate the study region as a $7^\circ \times 10^\circ$ box ($20^\circ\text{--}10^\circ\text{W}$, $5^\circ\text{--}12^\circ\text{N}$) encompassing the offshore maximum in the averaged seasonal rainfall (Fig. 4.1a). On average during the period of 25 August to 30 September, TRMM rainfall estimate indicate 300–750 mm of rainfall occurs within this zone, up to 40% of the mean seasonal rainfall (1838.7 mm) in the study region (Fig. 4.1b).

The spatial rainfall distribution over 25 August to 30 September 2006 indicates the model produces more rainfall in the region compared to the TRMM rainfall estimates for that period (Fig. 4.1c,d). The model simulates the offshore rainfall maximum but produces a maximum more than double than that observed by TRMM (1511 mm vs. 826 mm) (Fig. 4.1c,d) compared to TRMM (Fig. 4.1d).

The area-averaged total rainfall accumulation over that time for the study region is 373.81 mm based on TRMM rainfall estimates and 597.99 mm in TOPO, which is about 32% of the seasonal total. The area-averaged total rainfall accumulation decreases as the height of topography is reduced – 509.84 mm in HALF and 390.67 mm in FLAT. The offshore rainfall maximum weakens until it becomes non-existent as the height of topography is reduced (Fig. 4.1d-f). This suggests that the climatological offshore rainfall maximum is linked to topography. The flattening of topography leads to the weakening of the AEJ and AEWs. Since the Guinea Highlands have been identified as a region where AEWs may experience extra development, the weakening of the offshore rainfall maximum indicates that its existence has some connection with AEW-MCS systems as well. We examine the atmospheric conditions that lead to the offshore rainfall maximum observed in the reanalysis data and WRF simulations.

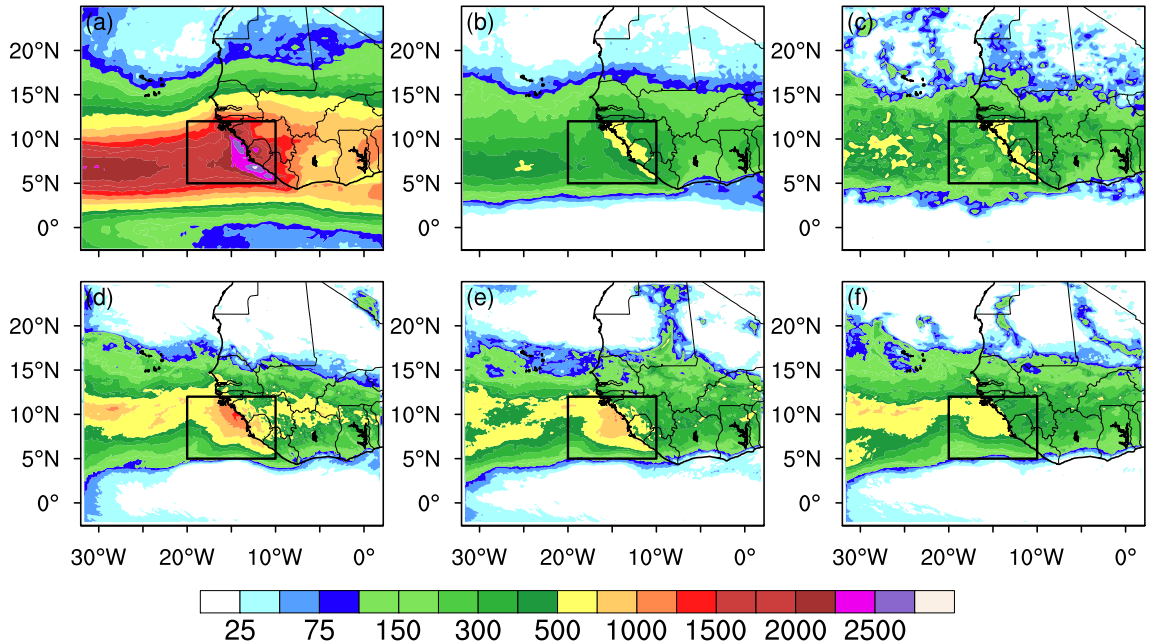


Figure 4.1. Annually-averaged (a) seasonal (May to October) TRMM rainfall (mm) and (b) TRMM rainfall accumulated over 1200 UTC 25 August to 0000 UTC 30 September over the period 1998-2013. Rainfall accumulation (mm) over 35.5-day period (1200 UTC 25 August to 0000 UTC 30 September 2006) from (c) TRMM, and domain 2 of (d) TOPO, (e) HALF and (f) FLAT. The bold lined box represents the study region from 20°–10°W and 5°–12°N.

4.4.1 Moisture Flux Convergence

First we examine the horizontal moisture convergence into the coastal region. Equations (1) and (2) define the moisture transports in terms of q (g kg^{-1}) and v (m s^{-1}) for latitudinal cross sections or u (m s^{-1}) for longitudinal cross sections.

$$\text{MoistureFlux}_{LAT} = vxq \quad (4.1)$$

$$\text{MoistureFlux}_{LON} = uxq \quad (4.2)$$

We calculate these kinematic moisture fluxes for the lower troposphere (boundary layer; 1000-850 hPa) and mid-troposphere (mid-level; 700-500 hPa). The total kinematic moisture fluxes are calculated for each day using Equations (3)-(5).

$$\text{NetMoisture}_{LAT} = \text{MoistureFlux}_{12^{\circ}N} - \text{MoistureFlux}_{5^{\circ}N} \quad (4.3)$$

$$\text{NetMoisture}_{LON} = \text{MoistureFlux}_{10^{\circ}W} - \text{MoistureFlux}_{20^{\circ}W} \quad (4.4)$$

$$MF = \text{NetMoisture}_{LAT} + \text{NetMoisture}_{LON} \quad (4.5)$$

Total kinematic moisture fluxes averaged over the season indicate that moisture flux convergence ($-MF$) occurs in the boundary layer in the coastal region. This result is expected since the region is located within the WAM and ITCZ where strong convergence drives the rainfall. Moisture flux divergence ($+MF$) occurs in the midlevels of the troposphere during the rainy season. Total kinematic moisture fluxes calculated for August 2006 indicated low-level moisture flux convergence but the mid-levels experienced periods of moisture convergence and divergence with 2-3 day intervals. The periodicity in the moisture fluxes indicated the presence of AEWs and we further examined the implications of those systems in producing the rainfall maximum.

4.5 Rainfall Composites

The day with the highest rainfall amount for the coastal region was determined from the area-averaged daily precipitation time series between the months of August and September (hereafter referred to as AS) for each year. We average the time series of precipitation over the sixteen years to produce composites centered on the

maximum rainfall day (day 0).

4.5.1 Composites of area-averaged terms

To understand how the atmospheric conditions change along with the precipitation time series, we create composites for the mid-level (700-500 hPa) meridional wind component, moisture flux and rain type centered on the maximum rainfall day (Fig. 4.2).

On average the peak daily rainfall measures at about 32 mm day⁻¹ during AS for the coastal region. Five days before and after the peak the coastal region gets between 10–20 mm day⁻¹ of rainfall (Fig. 4.2a). We extract the rain type from the TRMM PR data and calculate rain type ratios for the region by finding the number of grid points that are experiencing either convective (CONV) or stratiform (STRAT) rain.

$$\text{Rain Type Ratio} = \frac{\text{No. of gridpoints with CONV or STRAT}}{\text{Total no. of gridpoints raining}} \quad (4.6)$$

The ratios of rain type show that stratiform rain is the dominant rain type in the region and peaks to about 40% on the maximum rainfall day (Fig. 4.2b). The reflectivity composite produces values between 17 and 18 dBZ for the region (not shown), as expected since the lower rain rates of stratiform clouds have lower reflectivity values and have smaller and fewer raindrops. Very little of the rainfall is convective in this region (about 6%), but on the maximum rainfall day the composite suggests an increase to about 10% (Fig. 4.2b).

The mid-level meridional wind composite indicates that the northerlies intensify the a day before the maximum rainfall day (Fig. 4.2c). While low-level moisture convergence and mid-level moisture divergence peaks on the maximum rainfall day (Fig. 4.2d). We know that favorable conditions for MCSs, such as low-level convergence and mid-level divergence, exist ahead of the AEW trough (the northerly phase). These composites suggest that rainfall in the study region may be dominated by MCSs moving through in the northerly phase of AEWs. As MCSs cross the coast, they generally lose their convective characteristics and develop stratiform features.

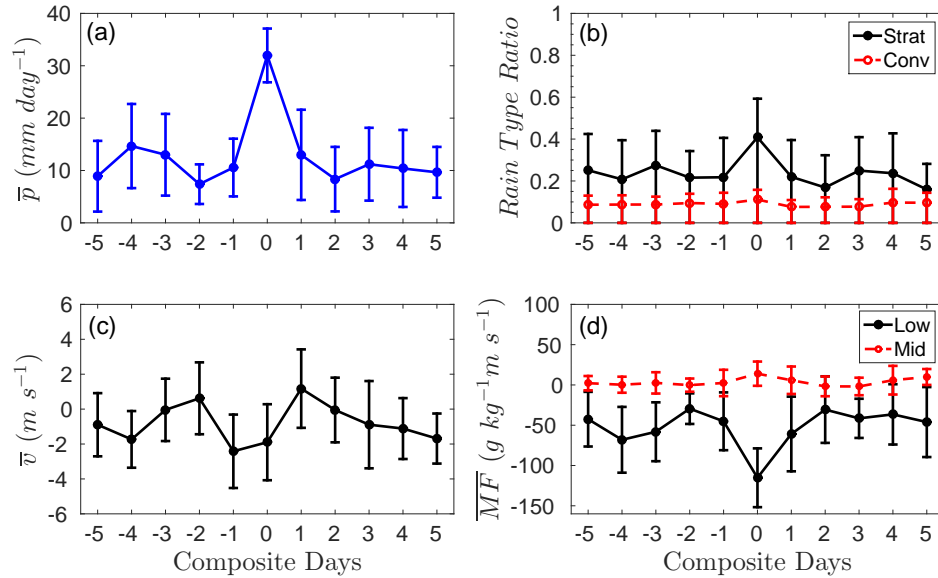


Figure 4.2. Composites of area-averaged (a) precipitation [mm day^{-1}], (b) rain type ratio (black = stratiform; red = convective), (c) meridional wind speed [m s^{-1}], and (d) moisture flux (black = low-level, 1000-850 hPa; red = mid-level, 700-500 hPa) [$\text{g kg}^{-1} \text{m s}^{-1}$] centered on the rainiest day in August-September averaged over 1998-2013.

4.5.2 Composites of deviations from the zonal mean

To further investigate the link between the offshore rainfall maximum and AEW activity we compute the deviations from the zonal average of the zonal wind (u'), meridional wind (v'), vertical velocity (ω'), and temperature (T'). To capture the more common 3–5-day easterly waves in this region we pass the variables through a 3–5-day bandpass filter using the method described in Chapter 3.

Similar to the mean composites, we analyze the evolution of the atmospheric setup from 5 days before to 5 days after the maximum rainfall day in AS. Figure 4.3 shows the spatial map composites of u' , v' , ω' , and T' on the maximum rainfall day (day 0). The pattern of u' at both low- and mid-levels show an area of negative u' (easterlies) over land and between 16°W and 20°W and positive u' (westerlies) just off the coast (Fig. 4.3a). The pattern of v' at both levels show positive values (southerlies) between 10°W and 14°W and negative values (northerlies) between 16°W and 20°W (Fig. 4.3b). These patterns indicate the flow associated with the AEWs and their vortices as they propagate through the region; note the wave axis in the middle of our coastal region (Fig. 4b). Ascent ($\omega' < 0$) is greatest along the

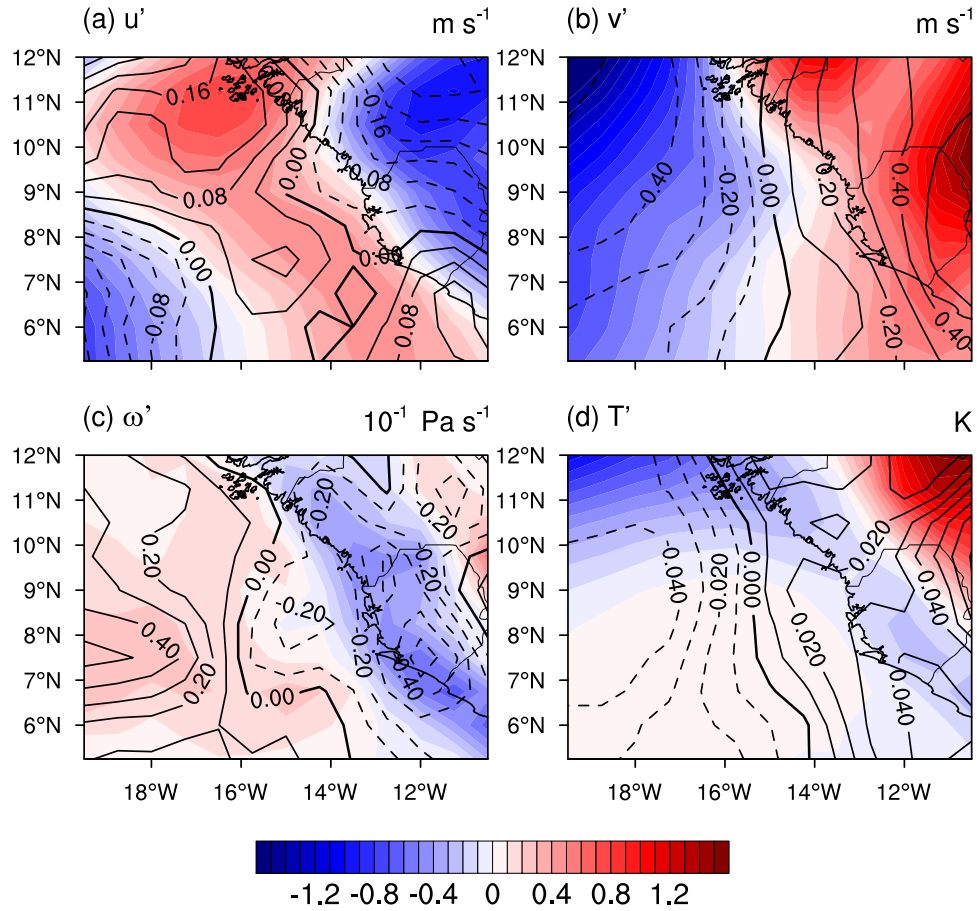


Figure 4.3. Composites of ERA-Interim 3-5-day filtered deviation from the zonal average in (a) zonal wind [m s^{-1}], (b) meridional wind [m s^{-1}], (c) vertical velocity [$10^{-1} \text{ Pa s}^{-1}$], and (d) temperature [K] at 1000-850 hPa (shaded) and 700-500 hPa (contour) on the rainiest day in August-September averaged over 1998-2013.

coastline (west of the Guinea Highlands) at low-level where cool ($T' < 0$) westerly onshore flow converges with the warm ($T' > 0$) easterly offshore flow (Fig. 4.3c and d). At mid-level, ascent is greatest along the coastline also, but T' is an order of magnitude smaller than that observed at low-levels (Fig. 4.3c and d). Typically at the coast, AEWs have maximum temperature anomalies between 850 and 950 hPa, which we observe in the T' composites (Fig. 4.3d). The patterns of mid-level v' , ω' , and T' indicate generation of eddy kinetic energy by baroclinic overturning as a result of southerly warm ascending (northerly cool descending) air associated with latent heat release (evaporative cooling) due to convection in the AEW trough (Fig. 4.3b,c and d). The release of latent heat from convection in precipitation regions

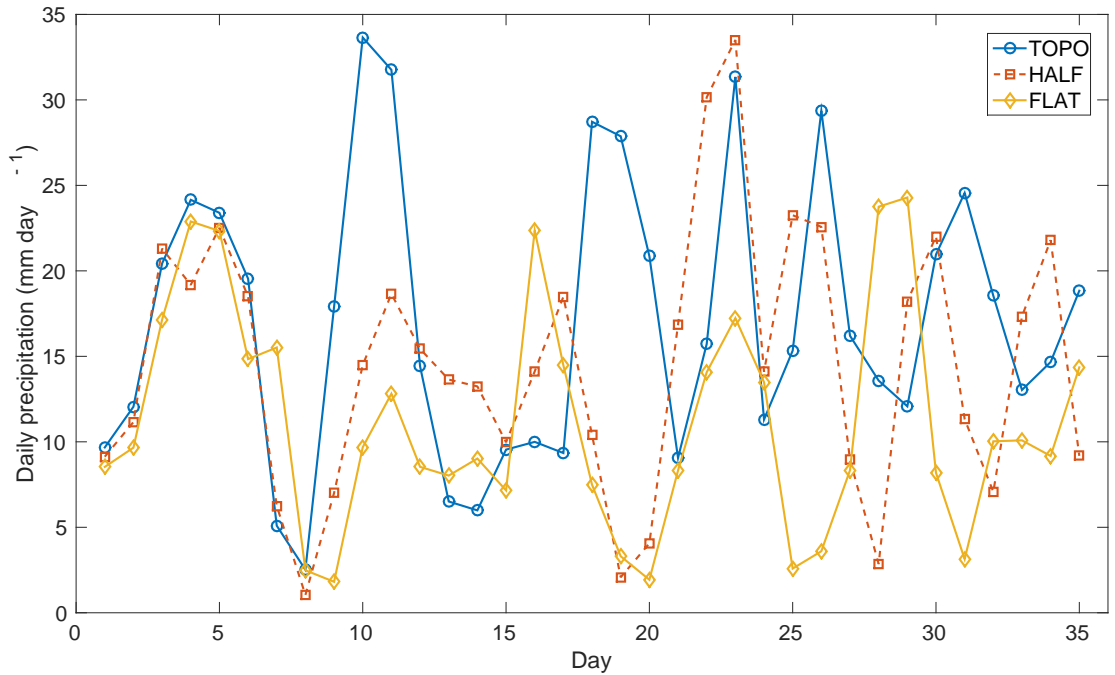


Figure 4.4. Daily timeseries of the simulated rainfall in TOPO (blue line), HALF (red line) and FLAT (yellow line).

has been diagnosed as a major source of wave energy at lower latitudes (Holton, 1972; Nitta, 1972), which explains the extra development in AEWs in this coastal region that also leads to increased rainfall amount from its associated convection. Enhanced AEW development can also be attributed to the interaction of the wave and the topography. This interaction leads to an increase in cyclonic vorticity of the wave in the lee of the topography and this is attributed to the net deflection of the air parcels by the mountain anticyclone (Zehnder, 1991).

Maximum rainfall days are defined as days that experience at least 25% over the mean daily rainfall observed in the study region for each WRF simulation (Fig. 4.4). The mean daily rainfall in the study region in TOPO is $17.08 \text{ mm day}^{-1}$, $14.57 \text{ mm day}^{-1}$ in HALF, and $11.16 \text{ mm day}^{-1}$ in FLAT. Figures 4.5-4.7 show spatial map composites of u' , v' , ω' , and T' based on peak rainfall days observed in the study region during the WRF sensitivity simulations. The composites are based on six maximum rainfall days in TOPO, five maximum rainfall days in HALF and four maximum rainfall days in FLAT. The low- and mid-level patterns of u' , v' , ω' ,

and T' on the maximum rainfall days in the TOPO composites are similar to the patterns in the ERA composites (Fig. 4.5a-d). Southeasterly anomalies over land and northwesterlies over the ocean with ascent along the coastline (Fig. 4.5a-c). Low-level T' is negative along the coast and positive further inland (Fig. 4.5d). Mid-level T' is a magnitude smaller than that observed at lower levels and is mostly negative over the ocean (Fig. 4.5d). The composites for HALF display similar patterns to TOPO and the ERA composites (Fig. 4.6), but with notably weaker ascent ($\omega' < 0$) along the coast and more upward motion occurring offshore (Fig. 4.6c). Maximum ascent continues to shift further offshore in the FLAT composites until there is very little indication of rising air over land at low- and mid-levels (Fig. 4.7c). This result indicates the role of the coastal topography in forcing ascent and creating favorable conditions for cyclogenesis. The composite of v' displays a similar pattern as the other simulations (Fig. 4.7b), but the u' composite indicates westerly motion between 10° and 16° W and easterlies between 16° W and 20° W at both levels. The absence of the topography allows the onshore monsoon flow to advance inland providing moisture for convective development.

4.6 Conclusion

Analyses of 16 years of 3-hourly rainfall data created using the Version 7 TRMM Multi-satellite Precipitation Analysis (TMPA) 3B42 data indicate the dominance of AEWs in organizing the local environment and also the strong influence of topography on the climatological stability of the rainfall maximum offshore of West Africa.

Composites of observed daily rainfall and meridional winds centered on the maximum rainfall days showed strong northerly winds in the study region, which supports the link between increased rainfall in our study region and the convergence zone ahead of an AEW (the northerly phase of the wave). Reflectivity and rain type (stratiform and convective) composites all suggest a distinct presence of stratiform rain throughout the region consistent with the rainfall being dominated by the trailing stratiform portion of continental MCSs moving offshore and through the rainfall maximum region. Spatial map composites of 3–5-day filtered deviations from the zonal mean from ERA- Interim reanalyses and the WRF simulations also support the connection between peak rainfall events and AEW activity in the study

region.

The amplitude of the rainfall maximum is reduced as topography is reduced (HALF and FLAT simulations), supporting the connection between the two features. The absence of the Guinea Highlands (FLAT) results in the absence of forced ascent in the coastal zone adjacent to the rainfall maximum; with the Highlands (TOPO, HALF) convection is enhanced near the coast. AEWs have been observed to experience extra development over the Guinea Highlands. Consistent with this result, weaker AEJ and AEWs are diagnosed in the FLAT sensitivity run compared to the more realistic TOPO run reducing the likelihood of both enhanced convective development of these weaker AEW-MCS systems and cyclogenesis at the coast.

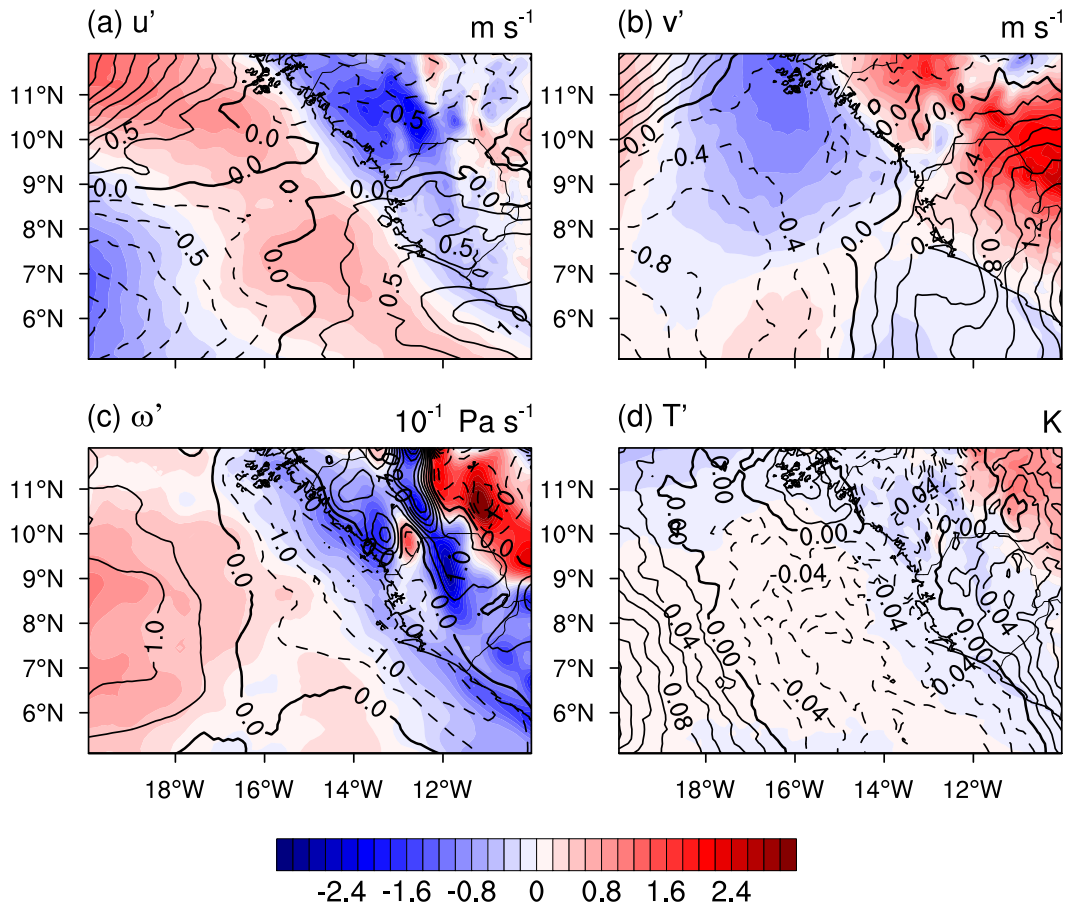


Figure 4.5. Composites of 3-5-day filtered deviation from the zonal average in (a) zonal wind [m s^{-1}], (b) meridional wind [m s^{-1}], (c) vertical velocity [$10^{-1} \text{ Pa s}^{-1}$], and (d) temperature [K] at 1000-850 hPa (shaded) and 700-500 hPa (contour) on the peak rainfall days during the WRF TOPO simulation.

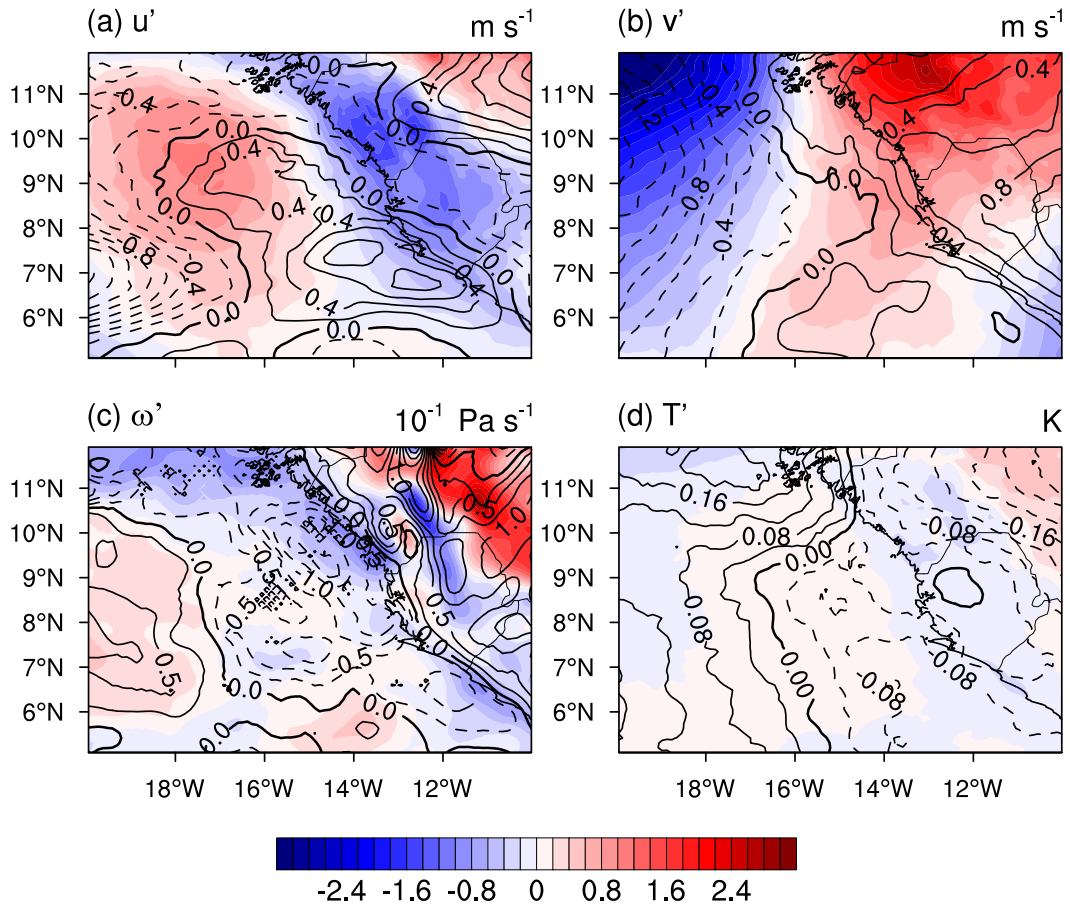


Figure 4.6. Composites of 3-5-day filtered deviation from the zonal average in (a) zonal wind [m s^{-1}], (b) meridional wind [m s^{-1}], (c) vertical velocity [$10^{-1} \text{ Pa s}^{-1}$], and (d) temperature [K] at 1000-850 hPa (shaded) and 700-500 hPa (contour) on the peak rainfall days during the WRF HALF simulation.

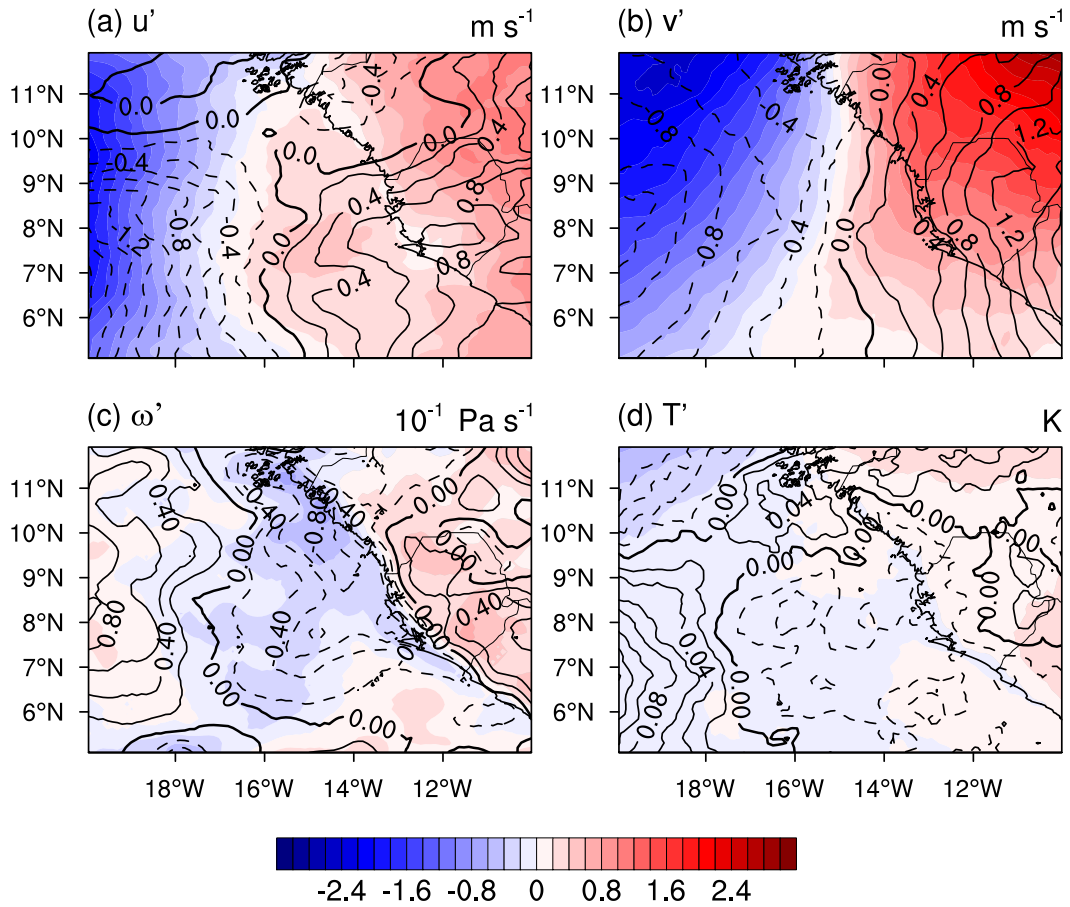


Figure 4.7. Composites of 3-5-day filtered deviation from the zonal average in (a) zonal wind [m s^{-1}], (b) meridional wind [m s^{-1}], (c) vertical velocity [$10^{-1} \text{ Pa s}^{-1}$], and (d) temperature [K] at 1000-850 hPa (shaded) and 700-500 hPa (contour) on the peak rainfall days during the WRF FLAT simulation.

Chapter 5 |

Summary and Conclusions

The influences of the topography over Africa on the strength and location of the AEJ, and its impact on the evolution of AEWs and MCSs have been examined. The importance of AEWs as a source of rainfall in West Africa and as tropical cyclone precursors motivated this study.

Three WRF sensitivity simulations were used to explore key influences on MCS in West Africa. To focus the project, a case study storm observed during the NAMMA field experiment during August 30-31, 2006 was investigated in three simulations with varying topography: realistic (TOPO), half-height (HALF), and no topography (FLAT). In all three sensitivity simulations, an MCS was observed at around the same time the observed storm developed. However, the development of the simulated MCSs differed in each run due to their interaction with the AEW and the onshore flow that were in turn impacted by the topography. In TOPO the MCS was located ahead of a weak AEW trough that influenced the development of the system as it travelled over land. As the squall line crossed the coastline it weakened, became less organized and eventually disintegrated over the Atlantic. The mid-troposphere winds in HALF indicated the presence of an AEW trough to the east of the simulated MCS; however, the storm was so far ahead of the trough that its development was not influenced by the AEW. As a result the storm simulated in HALF was the shortest lived out of all three sensitivity simulations, only lasting four hours. The MCS in FLAT was located ahead of an AEW trough, in the northerly phase of the wave, where strong low-level convergence occurs. The 850-hPa winds indicated strong low-level cyclonic vorticity associated with the system. The removal of the topography allowed the moist onshore flow to travel further inland, which also helped to sustain the MCS in the FLAT run.

The model was persistent in simulating the case study MCSs in conjunction

with AEWs. This highlighted the robustness of the well-known connection between the two systems in West Africa. However, the removal of topography affected the generation and development of the simulated MCSs and AEWs in West Africa. Energetics analyses emphasized the importance of the African topography in creating meridional temperature gradients. Smoothly decreasing the topographic elevations between the three sensitivity studies led to reduced meridional temperature gradients and a weaker AEJ. The weakening of the positive low-level temperature gradient led to the weakening of the AEJ, whose existence results from thermal wind balance and the strong meridional low-level temperature gradient. A weaker jet provides less zonal kinetic energy for conversion into eddy kinetic energy to grow and maintain AEWs. Weaker waves were generated in East Africa in FLAT compared to TOPO and HALF, but the greatest difference in the wave intensity between the three simulations occurred in West Africa. This supports topographic influences on the growth of the waves and their convective interactions as they propagate downstream. Consequently, the amplitude of the rainfall amount decreased over West Africa and the Atlantic Ocean.

TRMM rainfall estimates averaged over May to October indicated that the majority of the rainfall occurs north of the Equator with maxima in rainfall accumulation occurring over the Atlantic Ocean during the West African Monsoon (WAM) months. A small region of very high rainfall accumulations occurs within this zone just off the coast—this is the offshore rainfall maximum. Composites of observed daily rainfall and meridional winds centered on the maximum rainfall days showed strong northerly winds in the rainfall maximum region, which supports the link between increased rainfall in our study region and the convergence zone ahead of an AEW (the northerly phase of the wave). Reflectivity and rain type (stratiform and convective) composites all suggest a distinct presence of stratiform rain throughout the region consistent with the rainfall being dominated by the trailing stratiform portion of continental MCSs moving offshore and through the rainfall maximum region. Map composites of 3–5-day filtered deviations from the zonal mean from ERA-Interim reanalyses and the WRF simulations also support the connection between peak rainfall events and AEW activity in the study region. The climatological rainfall maximum weakened as topography is reduced, supporting the connection between the two features. On a local scale, the absence of the Guinea Highlands results in the lack of forced ascent in the coastal region adjacent to the

rainfall maximum. AEWs have been observed to experience extra development over the Guinea Highlands, where they experience increase in cyclonic vorticity and convection. Therefore, consistent with the weaker AEJ and AEWs diagnosed in FLAT, the likelihood of enhanced convective development of these weaker AEW-MCS systems and cyclogenesis at the coast is reduced leading to less rainfall in the rainfall maximum region.

Further studies are needed to confirm the role of the local topography in enhancing AEW development near the West African coast and subsequent feedbacks to the MCS evolution, so ultimately supporting the long-term offshore rainfall maximum. In particular, the relative influence of the ITCZ as a preferred region of cyclogenesis, the moist convection that occurs in this region and their interaction with AEW and topography should be explored further. Understanding of the mechanisms that lead to convective development and the offshore rainfall maximum will prove helpful in improving forecasts of the AEW-MCS systems that can become tropical cyclone precursor disturbances.

These results motivate consideration of the evolution of AEWs in global climate models. The coarser resolution of the climate models requires smoothing of the model topography, similar to the smoothing performed here in constructing the sensitivity studies (i.e., HALF). Thus, these experiments suggest that realistic representations of AEWs in climate models may require higher resolution simulations.

Bibliography

- Albignat, J. P. and Reed, R. J. (1980). The origin of African wave disturbances during Phase III of GATE. *Mon. Wea. Rev.*, 108:1827–1839.
- Baum, J. D. (2006). African easterly waves and their relationship to rainfall on a daily timescale. Master’s thesis, Florida State University.
- Berry, G. J. and Thorncroft, C. D. (2005). Case study of an intense African easterly wave. *Mon. Wea. Rev.*, 133:752–766.
- Burpee, R. W. (1972). The origin and structure of easterly waves in the lower troposphere of North Africa. *J. Atmos. Sci.*, 29:77–90.
- Carlson, T. N. (1969a). Some remarks on African disturbances and their progress over the tropical Atlantic. *Mon. Wea. Rev.*, 97:716–726.
- Carlson, T. N. (1969b). Synoptic histories of three african disturbances that developed into Atlantic hurricanes. *Mon. Wea. Rev.*, 97:256–275.
- Charney, J. G. and Stern, M. E. (1962). On the Stability of Internal Baroclinic Jets in a Rotating Atmosphere. *J. Atmos. Sci.*, 19:159–172.
- Chen, F. and Dudhia, J. (2001). Coupling an Advanced Land Surface-Hydrology Model with the Penn State-Ncar MM5 Modeling System. Part i: Model Implementation and Sensitivity. *Mon. Wea. Rev.*, 129:569–585.
- Cifelli, R., Lang, T., Rutledge, S. A., Guy, N., Zipser, E. J., Zawislak, J., and Holzworth, R. (2010). Characteristics of an African Easterly Wave observed during NAMMA. *J. Atmos. Sci.*, 67:3–25.
- D’Amato, N. and Lebel, T. (1998). On the characteristics of the rainfall events in the Sahel with a view to the analysis of climatic variability. *Int. J. Climatol.*, 18:955–974.
- de Magny, G. C., Guegan, J.-F., Petit, M., and Cazelles, B. (2007). Regional-scale climate-variability synchrony of cholera epidemics in West Africa. *BMC Infectious Diseases*, 7.

- Dee, D. P., Uppala, S. M., Simmons, A. J., Berrisford, P., Poli, P., Kobayashi, S., Andrae, U., Balmaseda, M. A., Balsamo, G., Bauer, P., Bechtold, P., Beljaars, A. C. M., van de Berg, L., Bidlot, J., Bormann, N., Delsol, C., Dragani, R., Fuentes, M., Geer, A. J., Haimberger, L., Healy, S. B., Hersbach, H., Hólm, E. V., Isaksen, L., Kållberg, P., Köhler, M., Matricardi, M., McNally, A. P., Monge-Sanz, B. M., Morcrette, J.-J., Park, B.-K., Peubey, C., de Rosnay, P., Tavolato, C., Thépaut, J.-N., and Vitart, F. (2011). The ERA-Interim reanalysis: configuration and performance of the data assimilation system. *Quart. J. Roy. Meteor. Soc.*, 137:553–597.
- DeLonge, M. S., Fuentes, J. D., Chan, S., Kucera, P. A., Joseph, E., Gaye, A. T., and Daouda, B. (2010). Attributes of mesoscale convective systems at the land-ocean transition in Senegal during NASA African Monsoon Multidisciplinary Analyses 2006. *J. Geophys. Res.*, 115.
- Diedhiou, A., Janicot, S., Viltard, A., and de Felice, P. (1998). Evidence of two regimes of easterly waves over West Africa and the tropical Atlantic. *Geophys. Res. Lett.*, 25:2805–2808.
- Diedhiou, A., Janicot, S., Viltard, A., and de Felice, P. (2002). Energetics of easterly wave disturbances over West Africa and the tropical Atlantic: A climatology from 1979-95 NCEP/NCAR reanalyses. *Climate Dyn.*, 18:487–500.
- Dudhia, J. (1989). Numerical study of convection observed during the winter monsoon experiment using a mesoscale two-dimensional model. *J. Atmos. Sci.*, 46:3077–3107.
- Erickson, C. O. (1963). An incipient hurricane near the west african coast. *Mon. Wea. Rev.*, 91:61–68.
- Estoque, M. A. and Lin, M. S. (1977). Energetics of easterly waves. *Mon. Wea. Rev.*, 105:582–589.
- Evans, J. L. and Shemo, R. E. (1996). A procedure for automated satellite-based identification and climatology development of various classes of organized convection. *J. Appl. Meteor.*, 35:638–652.
- Fall, S., Niyogi, D., and Semazzi, F. H. M. (2006). Analysis of mean climate conditions in Senegal (1971-1998). *Earth Interact.*, 10:1–40.
- Fink, A. H. and Reiner, A. (2003). Spatiotemporal variability of the relation between African easterly waves and West African squall lines in 1998 and 1999. *J. Geophys. Res.*, 108:4332.

- Fink, A. H., Vincent, D. G., and Ermert, V. (2006). Rainfall types in the West African Sudanian Zone during the Summer Monsoon 2002. *Mon. Wea. Rev.*, 134:2143–2164.
- Fjelde, H. and von Uexkull, N. (2012). Climate triggers: Rainfall anomalies, vulnerability and communal conflict in Sub-Saharan Africa. *Political Geography*, 31:444–453.
- Fuentes, J. D., Geerts, B., Dejene, T., D’Odorico, P., and Joseph, E. (2008). Vertical attributes of precipitation systems in West Africa and adjacent Atlantic Ocean. *Theor. Appl. Climatol.*, 92:181–193.
- Geerts, B. and Dejene, T. (2005). Regional and diurnal variability of the vertical structure of precipitation systems in Africa, based on spaceborne radar data. *J. Climate*, 18:893–916.
- Grell, G. A. and Freitas, S. R. (2013). A scale and aerosol aware stochastic convective parameterization for weather and air quality modeling. *Atmos. Chem. Phys. Discuss.*, 13:23845–23893.
- Grist, J. and Nicholson, S. E. (2001). A study of the dynamic factors influencing the rainfall variability in the West African Sahel. *J. Climate*, 14:1337–1359.
- Gu, G., Adler, R. F., Huffman, G. J., and Curtis, S. (2004). African easterly waves and their association with precipitation. *J. Geophys. Res.*, 109.
- Guy, N. and Rutledge, S. A. (2012). Regional comparison of west african convective characteristics: a TRMM-based climatology. *Quart. J. Roy. Meteor. Soc.*, 138:1179–1195.
- Guy, N., Rutledge, S. A., and Cifelli, R. (2011). Radar characteristics of continental, coastal, and maritime convection observed during AMMA/NAMMA. *Quart. J. Roy. Meteor. Soc.*, 137:1241–1256.
- Hall, N. M. J., Kiladis, G. N., and Thorncroft, C. D. (2006). Three dimensional structure and dynamics of African easterly waves. Part ii: dynamical modes. *J. Atmos. Sci.*, 63:2231–2245.
- Hendrix, C. and Salehyan, I. (2010). Climate change, rainfall, and social conflict in Africa. *J. Peace Res.*, 49:45–50.
- Hodges, K. and Thorncroft, C. D. (1997). Distribution and statistics of african mesoscale convective weather systems based on ISCCP Meteosat imagery. *Mon. Wea. Rev.*, 125:2821–2837.
- Holton, J. R. (1972). *An Introduction to Dynamic Meteorology*. Academic Press.

- Hong, S. Y. and Lim, J. O. (2006). The WRF Single-Moment 6-Class Microphysics Scheme (WSM6). *J. Korean Met. Soc.*, 42:129–151.
- Hong, S. Y., Noh, Y., and Dudhia, J. (2006). A new vertical diffusion package with explicit treatment of entrainment processes. *Mon. Wea. Rev.*, 134:2318–2341.
- Hsieh, J. S. and Cook, K. H. (2005). Generation of African Easterly Wave Disturbances: Relationship to the African Easterly Jet. *Mon. Wea. Rev.*, 133:1311–1327.
- Hsieh, J. S. and Cook, K. H. (2007). A study of the energetics of African Easterly Waves using a regional climate model. *J. Atmos. Sci.*, 64:421–440.
- Huffman, G. J., Bolvin, D. T., Nelkin, E. J., Wolf, D. B., Alder, R. F., Gu, G., Hong, Y., Bowman, K. P., and Stocker, E. F. (2007). The TRMM Multisatellite Precipitation Analysis (TMPA): Quasi-Global, Multiyear, Combined-Sensor Precipitation Estimates at Fine Scales. *J. Hydrometeorol.*, 8:38–55.
- Jenkins, G., Kucera, P. A., Joseph, E., Fuentes, J., Gaye, A., Gerlach, J., Roux, F., Viltard, N., Papazzoni, A., Protat, A., Bouniol, D., Reynolds, A., Arnault, J., Badiane, D., Kebe, F., Camara, M., Sall, S., Ndiaye, S., and Deme, A. (2010). Coastal observations of weather features in Senegal during the African Monsoon Multidisciplinary Analysis Special Observing Period 3. *J. Geophys. Res.*, 115.
- Jiménez, P. A., Dudhia, J., González-Rouco, J. F., Navarro, J., Montávez, J. P., and García-Bustamente, E. (2012). A revised scheme for the WRF surface layer formulation. *Mon. Wea. Rev.*, 140:898–918.
- Kelly-Hope, L. and Thompson, M. (2008). Climate and infectious diseases in seasonal forecasts. *Climate Change and Human Health: Health and Climate. Advances in Global Change Research*, 30:31–70.
- Kiladis, G. N., Thorncroft, C. D., and Hall, N. G. (2006). Three dimensional structure and dynamics of the African easterly waves, Part ii: Observations. *J. Atmos. Sci.*, 63:2212–2230.
- Kummerow, C., Barnes, W., Kozu, T., Shiue, J., and Simpson, J. (1998). The Tropical Rainfall Measuring Mission TRMM sensor package. *J. Atmos. Ocean. Technol.*, 15:809–817.
- Lafore, J. P., Flamant, C., Guichard, F., Parker, D. J., Bouniol, D., Fink, A. H., Giraud, V., Gosset, M., Hall, N., Höller, H., Jones, S. C., Protat, A., Roca, R., Roux, F., Saïd, F., and Thorncroft, C. (2011). Progress in understanding of weather systems in West Africa. *Atmos. Sci. Lett.*, 12:7–12.
- Laing, A. G., Carbone, R., Levizzani, V., and Tuttle, J. (2008). The propagation and diurnal cycle of deep convection in northern tropical africa. *Q. J. R. Meteorol. Soc.*, 134:93–109.

- Laing, A. G., Fritsch, J. M., and Negri, A. J. (1999). Contribution of mesoscale convective complexes to rainfall in Sahelian Africa: Estimates from geostationary infrared and passive microwave data. *J. Appl. Meteor.*, 38:957–964.
- Laurent, H., D’Amato, N., and Lebel, T. (1998). How important is the contribution of the mesoscale convective complexes to the Sahelian rainfall? *Phys. Chem. Earth*, 23:629–633.
- LeBarbé, L. and Lebel, T. (1997). Rainfall climatology of the HAPEX-Sahel region during the years 1950-1990. *J. Hydrol.*, 188:43–73.
- Lebel, T. and Ali, A. (2009). Recent trends in the Central and Western Sahel rainfall regime (1990–2007). *J. Hydrol.*
- Lebel, T., Taupin, J. D., and D’Amato, N. (1997). Rainfall monitoring during HAPEX-Sahel: 1. General rainfall conditions and climatology. *J. Hydrol.*, 189:74–96.
- Lélé, M. I. and Lamb, P. J. (2010). Variability of the Intertropical Front and Rainfall over the West African Sudan-Sahel Zone. *J. Climate*, 23:3984–4004.
- Leroux, S. and Hall, N. M. J. (2009). On the relationship between African easterly waves and the African easterly jet. *J. Atmos. Sci.*, 66:2303–2316.
- Lin, Y.-L., Robertson, K. E., and Hill, C. M. (2005). Origin and propagation of a disturbance associated with an African easterly wave as a precursor of hurricane alberto (2000). *Mon. Wea. Rev.*, 133:3276–3298.
- Mathon, V., Laurent, H., and Lebel, T. (2002). Mesoscale convective system rainfall in the Sahel. *J. Appl. Meteor. Climatol.*, 41:1081–1092.
- Mekonnen, A., Thorncroft, C. D., and Aiyyer, A. R. (2006). Analysis of convection and its association with african easterly waves. *J. Climate*, 19:5405–5421.
- Mlawer, E. J., Taubman, S. J., Brown, P. D., Iacono, M. J., and Clough, S. A. (1997). Radiative transfer for inhomogeneous atmosphere: RRTM, a validated correlated-k model for the long wave. *J. Geophys. Res.*, 102:16663–16682.
- Mohr, K. I. and Thorncroft, C. D. (2006). Intense convective systems in West Africa and their relationship to the African easterly jet. *Q. J. R. Meteorol. Soc.*, 132:163–176.
- Monin, A. S. and Obukhov, A. M. (1954). Basic laws of turbulent mixing in the surface layer of the atmosphere. *Tr. Akad. Nauk SSSR Geofiz. Inst.*, 24:163–187.

- Mozer, J. B. and Zehnder, J. A. (1996a). Lee vorticity production by large-scale tropical mountain ranges. part I: Eastern North Pacific tropical cyclogenesis. *J. Atmos. Sci.*, 53:521–538.
- Mozer, J. B. and Zehnder, J. A. (1996b). Lee vorticity production by large-scale tropical mountain ranges. part II: A mechanism for the production of African waves. *J. Atmos. Sci.*, 53:539–549.
- Nicholls, S. D. and Mohr, K. I. (2010). An analysis of the environments of intense convective systems in West Africa in 2003. *Mon. Wea. Rev.*, 138:3721–3739.
- Nicholson, S. E. (2008). The intensity, location and structure of the tropical rainbelt over west Africa as factors in interannual variability. *Int. J. Climatol.*, 28:1775–1785.
- Nicholson, S. E. (2009). A revised picture of the structure of the monsoon and land ITCZ over west africa. *Climate Dynamics*, 32:1155–1171.
- Nicholson, S. E. and Yin, X. (2001). Rainfall Conditions in Equatorial East Africa during the Nineteenth Century as Inferred from the Record of Lake Victoria. *Climatic Change*, 48:387–398.
- Nitta, T. S. (1972). Energy budget of wave disturbances over the Marshall Islands during the years of 1956 and 1958. *J. Meteor. Soc. Japan*, 50:71–84.
- Norquist, D. C., Recker, E. E., and Reed, R. J. (1977). The energetics of African Wave disturbances as observed during Phase III of GATE. *Mon. Wea. Rev.*, 105:334–342.
- Nzeukou, A. and Sauvageot, H. (2002). Distribution of rainfall parameters near the coasts of France and Senegal. *J. Appl. Meteor.*, 41:69–82.
- O’Loughlin, J., Witmer, F. D. W., Linke, A. M., Laing, A., Gettelman, A., and Dudhia, J. (2012). Climate variability and conflict risk in East Africa, 1990-2009. *Proc. Natl. Acad. Sci. (USA)*, 109:18344–18349.
- Pytharoulis, I. and Thorncroft, C. D. (1999). The low-level structure of African easterly waves in 1995. *Mon. Wea. Rev.*, 127:2266–2280.
- Redelsperger, J., Diongue, A., Diedhiou, A., Ceron, J., Diop, M., Gueremy, J., and Lafore, J. (2002). Multi-scale description of a Sahelian synoptic weather system representative of the West African monsoon. *Quart. J. Roy. Meteor. Soc.*, 128:1229–1257.
- Reed, R., Norquist, D., and Recker, E. (1977). The structure and properties of African wave disturbances as observed during Phase III of GATE. *Mon. Wea. Rev.*, 105:413–420.

- Rennick, M. A. (1976). The generation of African easterly waves. *J. Atmos. Sci.*, 33:1955–1969.
- Robert, V., MacIntyre, K., Keating, J., Trape, J.-F., Duchemin, J.-B., Warren, M., and Beier, J. C. (2003). Malaria transmission in urban sub-Saharan Africa. *Trop. Med. Hyg.*, 68:169–176.
- Roeloffzen, J. C., Berg, W. D. V. D., and Oerlemans, J. (1986). Frictional convergence at coastlines. *Tellus*, 38A:397–411.
- Shultz, J. M., Russell, J., and Espinel, Z. (2005). Epidemiology of Tropical Cyclones: The Dynamics of Disaster, Disease, and Development. *Epidemiologic Reviews*, 27:21–25.
- Skamarock, W. C., Klemp, J. B., Dudhia, J., Gill, D. O., Barker, D. M., Duda, M. G., Huang, X.-Y., Wang, W., and Powers, J. G. (2008). A Description of the Advanced Research WRF Version 3. *NCAR Tech. Note NCAR/TN-475+STR*.
- Skinner, C. B. and Diffenbaugh, N. S. (2013). The contribution of African easterly waves to monsoon precipitation in the CMIP3 ensemble. *J. Geophys. Res. Atmos.*, 118:3590–3609.
- Skinner, C. B. and Diffenbaugh, N. S. (2014). Projected changes in African easterly wave intensity and track in response to greenhouse forcing. *Proc. Natl. Acad. Sci. (USA)*, 111:6882–6887.
- Thompson, R. M., Payne, S. W., Recker, E. E., and Reed, R. J. (1979). Structure and properties of synoptic-scale wave disturbances in the intertropical convergence zone of the eastern Atlantic. *J. Atmos. Sci.*, 36:53–72.
- Thorncroft, C. D. (1995). An idealised study of African easterly waves III. More realistic basic states. *Quart. J. Roy. Meteor. Soc.*, 121:1589–1614.
- Thorncroft, C. D., Hall, N., and Kiladis, G. (2008). Three dimensional structure and dynamics of African Easterly Waves. Part III: Genesis. *J. Atmos. Sci.*, 65:3596–3607.
- Thorncroft, C. D. and Hodges, K. (2001). African easterly wave variability and its relationship to Atlantic tropical cyclone activity. *J. Climate*, 14:1166–1179.
- Thorncroft, C. D. and Hoskins, B. J. (1994a). An idealised study of African easterly waves i. A linear view. *Quart. J. Roy. Meteor. Soc.*, 120:953–982.
- Thorncroft, C. D. and Hoskins, B. J. (1994b). An idealised study of African easterly waves II. A nonlinear view. *Quart. J. Roy. Meteor. Soc.*, 120:983–1015.

- Torrence, C. and Compo, G. P. (1998). A Practical Guide to Wavelet Analysis. *Bull. Amer. Meteor. Soc.*, 79:61–78.
- Tsakraklides, G. and Evans, J. L. (2003). Global and Regional Diurnal Variations of Organized Convection. *J. Climate*, 16:1562–1572.
- Wu, M. C., Reale, O., Schubert, S. D., Suarez, M. J., Koster, R. D., and Pegion, P. J. (2009). African Easterly Jet: Structure and Maintenance. *J. Climate*, 22:4459–4480.
- Xu, W. and Zipser, E. J. (2012). Properties of deep convection in tropical continental, monsoon, and oceanic rainfall regimes. *Geophys. Res. Lett.*, 39.
- Xu, W., Zipser, E. J., Chen, Y.-L., Liou, Y.-C., Lee, W.-C., and Jou, B. (2012). An orography-associated extreme rainfall event during TiMREX: initiation, storm evolution, and maintenance. *Mon. Wea. Rev.*, 140:2555–2574.
- Zawislak, J. and Zipser, E. J. (2010). Observations of seven African Easterly Waves in the East Atlantic during 2006. *J. Atmos. Sci.*, 67:26–43.
- Zehnder, J. A. (1991). The interaction of planetary-scale tropical easterly waves with topography: A mechanism for the initiation of tropical cyclones. *J. Atmos. Sci.*, 127:1217–1230.
- Zehnder, J. A. and Gall, R. L. (1991). On a mechanism for orographic triggering of tropical cyclones in the Eastern North Pacific. *Tellus*, 43:25–36.
- Zehnder, J. A., Powell, D. M., and Ropp, D. L. (1999). The interaction of easterly waves, orography, and the intertropical convergence zone in the genesis of Eastern Pacific tropical cyclones. *Mon. Wea. Rev.*, 127:1566–1585.

Vita

Holly L. Hamilton

Education

- The Pennsylvania State University* State College, PA 2011–2015
Ph.D. in Meteorology
- The Pennsylvania State University* State College, PA 2008–2011
M.S. in Meteorology
- University of Leeds* Leeds, UK 2005–2008
B.S. in Meteorology & Atmospheric Science, *First Class Honors*

Awards and Honors

- Anne C. Wilson Graduate Research Award August 2008

Research Experience

- Doctoral Research* The Pennsylvania State University 2011–2015
Dissertation Co-Advisors: Dr. Jenni Evans & Dr. José Fuentes
Dissertation: “Relationships between Rainfall Characteristics and Environmental Predictors in the West African Region”
- Graduate Research* The Pennsylvania State University 2008–2011
Research Advisor: Dr. Jenni Evans
Thesis: “Observations of Tropical Cyclone Boundary Layer Winds in the Core of Hurricane Ike”
- Undergraduate Research* University of Leeds 2005–2008
Research Advisor: Dr. Cornelia Schwierz
Research Title: “Extratropical transition: The Effects of Atlantic Hurricanes on United Kingdom Weather”

Teaching Experience

- Teaching Assistant* The Pennsylvania State University 2012–2014